Atomic structures and properties of oxide interfaces

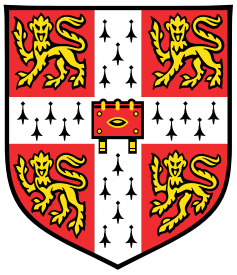

Bonan Zhu

Supervisor: Prof. Judith Driscoll

Department of Materials Science and Metallurgy
University of Cambridge

This dissertation is submitted for the degree of
Doctor of Philosophy

Queens' College

April 2020

Declaration

This thesis is the result of my own work and includes nothing which is the outcome of work done in collaboration except as declared in the Preface and specified in the text. It is not substantially the same as any that I have submitted, or, is being concurrently submitted for a degree or diploma or other qualification at the University of Cambridge or any other University or similar institution except as declared in the Preface and specified in the text. I further state that no substantial part of my thesis has already been submitted, or, is being concurrently submitted for any such degree, diploma or other qualification at the University of Cambridge or any other University or similar institution except as declared in the Preface and specified in the text. This dissertation contains fewer than 60,000 words including abstract, tables, footnotes and appendices.

Bonan Zhu
April 2020

Atomic structures and properties of oxide interfaces

Bonan Zhu

Abstract

This thesis uses computational approaches, mainly first-principles methods, to study interfaces in oxide thin films. One of the difficulties in interface studies is the lack of definitive atomistic models, yet they are essential input for any calculations. Here, this problem is tackled by *ab initio* random structure searching (AIRSS), or more broadly speaking, random structure searching (RSS). The initial work studies the interfaces in vertically aligned nanocomposites (VANs) that consist of CeO_2 pillars embedded in a $SrTiO_3$ matrix. Enhanced ionic conductivity has been found in these VANs in prior studies, but the role of vertical interfaces is not explained. The initial interface searches are performed with interatomic potentials due to the large size of the interface, followed by refinement first-principles calculations. Based on the obtained structures, it is shown that the majority interfaces are unlikely to directly enhance ionic conductivity. However, a parallel solid-state O^{17} NMR study by our collaborators later obtained interface signals that suggest fast ionic conduction. First-principles NMR calculations show the observed signals are not consistent with the majority interface initially studied; instead, they can be assigned to the minority interfaces that are in different orientations.

The following work studies the planar interfaces between epitaxial films of CeO_2 and STO substrates. A significant amount of research has been devoted to fluorite-perovskite interfaces since the controversial report of colossal ionic conductivity enhancement in YSZ/STO heterostructures. However, the exact atomic structures of these interfaces are not well understood. AIRSS is used for finding stable CeO_2/STO planar interfaces taking account of different terminations and local stoichiometries. When the STO terminates with a TiO_2 layer, a rock salt structured CeO layer emerges at the interface. On the other hand, with SrO termination, the stable structure contains a partially occupied anion lattice, which gives rise to lateral diffusion of oxygen anions in molecular dynamics simulations. In both cases, the interfaces are found to attract oxygen vacancies, which hinders ionic transport in the perpendicular direction.

The subsequent work starts with addressing the perovskite-perovskite interfaces between $La_{0.1}Ba_{0.9}MnO_3$ (LBMO) and STO. LBMO is a ferromagnetic insulator with a relatively high ferromagnetic transition temperature, which makes it an ideal material for spintronics applications. However, thin films of LBMO are conductive except when the thickness is less than eight unit cells. This has been attributed to the octahedral proximity effects, as electron microscopy reveals that octahedral tilting in LBMO is suppressed near the interfaces. Whist some experimental observations are successfully accounted for by the first-principles calculations, the predicted tilt angle suppression is much weaker than that observed. By studying the response of octahedral networks to corner perturbations, it is shown that a competing LBMO phase with an alternative tilt configuration is stable as a result of interface coupling.

I would like to dedicate this thesis to my parents and wife.

Acknowledgements

I would like to acknowledge my supervisors Prof. Judith Driscoll and Prof. Chris Pickard for their continuous guidance, support, discussions of science, and provisions of research facilities. Calculations in this work were performed using the Cambridge Service for Data-Driven Discovery, the UK national supercomputing service ARCHER, and UK Materials and Molecular Modelling Hub. The access to the last two facilities was obtained through the UK Car-Parrinello Consortium funded by EPSRC grant ref EP/P022561/1. I am grateful to my sponsors: Cambridge Commonwealth and International Trust and China Scholarship Council for funding, without which I would not be able to undertake these research projects. I would also like to express my gratitude to Dr. Georg Schusteritsch, Dr. Joseph Nelson for helpful discussions of theories and computational methods; Dr. Weiwei Li, Dr. Eun-Mi Choi and Dr. Rui Wu for sharing experimental results, having discussions and exchanging ideas. I am grateful to all my colleagues and collaborators: Ben Shires, Bowen Zhang, Gareth Cornish, Michael Hope, Dr. Ping Lu, and Xiaolei Feng. Special thanks to Ben, Joseph and Xiaolei who helped proofread this thesis. I would also like to thank Dr. Aiping Chen, who hosted me during the visit to Los Alamos National Laboratory; and Dr. Blas Uberuaga and Dr. Richard Hoagland for fruitful discussions while I was there.

Last but not least, I want to thank my parents, my wife, and my friends for their kindness, encouragement, and support during my time as a PhD student.

Publications

The following papers have been published/in preparation during my PhD study:

- **Zhu, B.**; Schusteritsch, G.; Lu, P.; MacManus-Driscoll, J. L.; Pickard, C. J. Determining Interface Structures in Vertically Aligned Nanocomposite Films. APL Materials 2019, 7 (6), 061105. DOI:10.1063/1.5099204.
  I performed structure searching and interface calculations. The results are presented in Chapter 5.

- Li, W.[†]; **Zhu, B.**[†]; He, Q.[†]; Borisevich, A. Y.; Yun, C.; Wu, R.; Lu, P.; Qi, Z.; Wang, Q.; Chen, A.; et al. Interface Engineered Room-Temperature Ferromagnetic Insulating State in Ultrathin Manganite Films. Advanced Science 2020, 7 (1), 1901606. DOI:10.1002/advs.201901606.
  I performed first-principles calculations and participated the XMCD beamline experiment at Diamond Light Source. Relevant results are described in Chapter 7.

- Choi, E.-M.[*]; **Zhu, B.**[*]; Lu, P.; Feighan, J.; Sun, X.; Wang, H.; MacManus-Driscoll, J. L. Magnetic Signatures of 120 K Superconductivity at Interfaces in La2CuO4$_{+\delta}$. Nanoscale 2020. DOI:10.1039/C9NR04996G.
  I analysed the electron micrographs to extract the change of lattice parameters and identify an unknown phase. The results are briefly described in Chapter 8.

- Choi, E.-M.; Bernardo, A. D.; **Zhu, B.**; Lu, P.; Alpern, H.; Zhang, K. H. L.; Shapira, T.; Feighan, J.; Sun, X.; Robinson, J.; et al. 3D Strain-Induced Superconductivity in La2CuO4$_{+\delta}$ Using a Simple Vertically Aligned Nanocomposite Approach. Science Advances 2019, 5 (4), eaav5532. DOI:10.1126/sciadv.aav5532.
  I performed analyses of the electron micrographs. This work is briefly described in Chapter 8.

[†]Equal contribution
[*]Correspondence

- Lin, Y.; Choi, E. M.; Lu, P.; Sun, X.; Wu, R.; Yun, C.; **Zhu, B.**; Wang, H.; Li, W.; Maity, T.; et al. Vertical Strain-Driven Antiferromagnetic to Ferromagnetic Phase Transition in EuTiO3 Nanocomposite Thin Films. ACS Appl. Mater. Interfaces 2020. DOI:10.1002/advs.201901606.
  I assisted analyses of the electron micrographs.

- Ghidini, M.; **Zhu, B.**; Mansell, R.; Pellicelli, R.; Lesaine, A.; Moya, X.; Crossley, S.; Nair, B.; Maccherozzi, F.; Barnes, C. H. W.; et al. Voltage Control of Magnetic Single Domains in Ni Discs on Ferroelectric BaTiO3. J. Phys. D: Appl. Phys. 2018, 51 (22), 224007. DOI:10.1088/1361-6463/aabf77.
  I performed the data analyses. I also participated in the beamline XMCD-PEEM experiment, and carried out in-house AFM characterisations before the start of my PhD study.

- Choi E.-M.; Maity, T.; Kursumovic, A.; Lu, P.; Bi, Z.; Yu, S.; Park, Y.; **Zhu, B.**; Wu, R.; Gopalan, V.; Wang, H.; MacManus-Driscoll, J. L. Nanoengineering Room Temperature Ferroelectricity into Orthorhombic SmMnO3 Films. Nature Comminations 2020, Accepted
  I performed DFT calculations to reveal the responses of bond-angles to elastic strain.

- **Zhu, B.**; Schusteritsch, G.; Pickard, C. J.; MacManus-Driscoll, J. L. Ionic conducting STO/CeO_2 interfaces. In preparation.
  I performed all structure searching and calculation works. The results are presented in Chapter 6.

- Hope, M.; Zhang, B.; **Zhu, B.**; Halat, D. M.; Lu, P.; MacManus-Driscoll, J. L.; Grey P.G. A new approach to probe interfaces in complex oxide heterostructures via solid state NMR. In preparation.
  I performed first-principles NMR calculations, and the findings are presented in Section 5.5.

- **Zhu, B.**; MacManus-Driscoll, J. L. Stabilising Octahedral Tilt in Perovskite Oxide by Substrate Pining. In preparation.
  I performed first-principles calculations for quantifying the flexibility of octahedral networks in perovskites. The results are included in Chapter 7

Table of contents

List of figures

List of tables

Nomenclature

Acronyms / Abbreviations

ABF Annular bright field (imaging)

ABF Annular bright field

AFM Atomic force microscopy

AIRSS *Ab initio* Random Structure Searching

DFT Density functional theory

DOS Density of states

FFT Fast Fourier transform

FORC-IV First-order reversal curve I–V

GGA General gradient approximation

GIPAW Gauge including projector augmented wave

HAADF High-angle annular dark field

HADDF High-angle annular dark-field (imaging)

HF Hartree-Fock

iDPC Integrated differential phase contrast

KS Khon-Sham

LBMO $La_{1-x}Ba_xMnO_3$

LSMO $La_{1-x}Sr_xMnO_3$

LDA Local density approximation

LMO $LaMnO_3$

AIMD *Ab initio* molecular dynamics

MD Molecular dynamics

NMR Nuclear magnetic resonance

OTFG On-the-fly generated (pseudopotential)

PAW Projector augmented wave

PDOS Projected density of states

PEEM Photoemission electron microscopy

PES Potential energy surface

PLD Pulsed Laser Depositions

PVD Physical Vapour Deposition

SDC Sm-doped ceria

SOFC Solid oxide fuel cell

STEM Scanning transmission electron microscope

STEM Scanning transmission electron microscopy

STO $SrTiO_3$

TEM Transmission electron microscope

UHV Ultra-high Vacuum

VAN Vertically Aligned Nanocomposites

XAS X-ray absorption spectroscopy

XC Exchange-Correlation

XLD X-ray linear dichroism

XMCD X-ray magnetic circular dichroism

XPS X-ray photoemission spectroscopy

YSZ Yittra-stablised zirconia

Chapter 1

Introduction and Overview

Oxides exhibit a wide range of fascinating properties, such as electronic/ionic conduction, magnetism, superconductivity, ferroelectricity and catalytic activity. Their usefulness is further enhanced by thin film deposition techniques, allowing single-crystal like materials to be grown with precise orientation, composition, termination, and thickness [1]. This creates an enormous playground for fundamental sciences as well as functional devices. Current silicon based semiconductor technologies are reaching their physical limits. Oxide materials provide a promising platform for not only replacing existing technologies, but also incubating emergent applications of thin film devices where functional properties are tightly integrated [2].

The quote *the interface is the device* by Nobel laureate Herbert Kroemer originally referred to the heterogeneous interfaces in semiconductors [3], which give them unique electric and optical properties because of interface induced phenomena such as the depletion region, band bending, and 2D electron gases (2DEGs). Similarly, interface induced phenomena play pivotal roles in realising a wide range of functional properties with oxides [4, 5]. The discovery of 2D electron gases at $LaAlO_3$(LAO)/$SrTiO_3$(STO) interfaces have sparked great research interest in the field [6], and many other emergent effects have been found at oxide interfaces including superconductivity [7, 8], ferroelectricity [9], magnetism[10] and ionic conduction [11, 12]. Whilst these interfaces posses enormous potential thanks to the wide structural and chemical spaces of oxides, their complexity makes it difficult to acquire mechanistic understandings. For example, even though bulk LAO and STO have the well-known perovskite structures, finding the exact cause of the 2DEGs at their interfaces turned out to be non-trivial, and significant research effort has been devoted to this subject [13–19].

Emerging interface phenomena are often attributed to subtle changes in the electronic and ionic structures, such as charge transfer [20], orbital reconstruction [21], and cation intermixing [16], but the small size and subsurface nature of interfaces make them challenge for

experimental studies, and direct probing is often impossible. Theoretical and computational approaches are hence of great importance for understanding interfaces. However, they require exact atomic structures to be known to start with. Reliably getting this information can be difficult experimentally, hence most existing theoretical works only considered structurally simple interfaces. In this thesis, a different approach is used, as systematic computational searches are performed to find possible low energy interface structures. Methods for predicting structures of materials have been developed and successfully applied in various fields of materials science [22–24]. Heterogeneous interfaces are challenging cases for structure prediction, owing to their complexity and the requirement of large simulation cells, and hence remain relatively unexplored.

Ionic conducting materials are needed for energy-related applications [25, 26], gas sensors [26, 27], and resistive switching devices [28]. The possibility of enhancing ionic conductivity through interface effects has attracted a significant amount of research interest. For example, Garcia-Barriocanal et al. have reported an enhancement of eight orders of magnitude in ionic conductivity (compard to the bulk) at yittra-stablised zirconia (YSZ)/$SrTiO_3$(STO) interfaces, although some argued that the effect has an electronic origin [29–31]. Enhanced ionic conductivity has also been observed in vertically aligned nanocomposites (VANs) [32, 33], which have pillar-matrix nanostructures and abundant vertical interfaces [34]. However, the cause of these enhancements is not fully understood, and the roles of interfaces need to be clarified. In Chapter 5, the structures of vertical interfaces in STO/CeO_2 VANs are determined using random structure searching, and subsequent analysis shows interfaces having the majority STO(100)/CeO_2(110) orientation are unlikely to give enhancements. Meanwhile, a solid-state NMR study carried out in parallel observed interface signals that suggest the existence of fast ionic conduction. First-principles NMR calculations show the observed NMR chemical shifts are consistent with the interfaces in the minority STO(110)/CeO_2(100) orientation, which are located at the corners of the CeO_2 pillars.

The structures of fluorite-perovskite interfaces are non-trivial, as a result of mismatches in both structure and chemistry of the two sides. One example is the YSZ/STO interface mentioned above. The exact atomic structure at interfaces needs to be clarified before any atomistic level theoretical studies can be carried out. In Chapter 6, low energy structures of STO(001)/CeO_2(001) interfaces are predicted, and their effects on oxygen vacancies are subsequently studied. It is found that the stable interface structure contains a partially occupied anion sublattice, which results in lateral diffusion of oxygen ions confined to the interface.

Perovskite structured oxides with general formula ABO_3 have attracted great research interest, owing to their seemingly simple crystal structures and flexibility in chemical space.

Most perovskite structured oxides have distorted structures due to the radii of species being not fully compatible, giving tolerance factors not equal to one [35]. The vertex-sharing BO_6 octahedra have a range of possible tilt patterns [36]. Networks of different tilt pattern and magnitude can be coupled via perovskite-perovskite interfaces, and hence affect the electronic and magnetic degrees of freedom that are closely intertwined with the crystal structure [4].

Perovskite structured ferromagnetic insulators are useful in spintronic applications [37, 38]. $La_{0.9}Ba_{0.1}MnO_3$ (LBMO) is ferromagnetic and insulating as bulk material [39, 40]. Thin films of LBMO deposited on STO substrate are found to be strongly affected by interfaces [41]. Ultra-thin films and superlattices of LBMO with a few unit cells in thickness/periodicity are insulating and have much increased Curie temperatures. This was experimentally found to coincide with the suppression of octahedral tilting, which is not present in thick LBMO films that are conductive [42]. In Chapter 7, the LBMO/STO heterostructures are studied using first-principles methods, giving theoretical insights for the experimental results. The flexibility of the octahedral network is found to be highly dependent on its tilt pattern, and that the experimentally observed tilt suppression may be explained by an alternative phase being stabilised due to the pinning of the octahedral corners at the interfaces.

The rest of this thesis is structured as follows. Chapter 2 gives the background of oxide interfaces and literature reviews of related topics. In Chapter 3, the computational methods used in this thesis are introduced. Chapter 4 describes structure prediction techniques and how they can be applied to interfaces. The main results are given in Chapters 5-7 as mentioned above. Chapter 8 summarises additional work carried out during the PhD research. Finally, conclusions and outlooks are given in Chapter 9.

Chapter 2

Oxide interfaces: background and literature review

This chapter provides a description of oxide thin films and interfaces, as well as giving an account of existing work in the literature relevant to this thesis. The first section introduces the growth of oxide films. The second section briefly reviews existing studies investigating the effects of planar interfaces on ionic conductivity. Following this, vertically aligned nanocomposites (VANs) are introduced, whose vertical interfaces are investigated in Chapter 5. Section 2.4 gives a review of prior interface structure prediction studies, and discusses the connections to the work completed in this thesis. The final section gives background on octahedral tilting in perovskites. The coupling of tilted octahedral networks at perovskite-perovskite interfaces is studied in Chapter 7.

2.1 Growth of oxide thin films

High quality epitaxial films are required for studying interfaces. Oxide thin films concerned in this work are mostly fabricated using physical vapour deposition (PVD), where different species arrive at the surface in vapour phases. This process typically happens in ultra high vacuum (UHV).

The substrate acts as a template and controls the crystallographic orientation of the film grown. They are often chosen to have the same or similar structure prototype as the film, and have certain surface orientations. Their surface terminations can be controlled by various chemical or physical treatments. A simple model of the growth process is that the high energy ad-atoms arrive at the surface, diffuse around and settle down at preferred sites after some time. The microstructure and surface topology of the resulting film depends on the

growth mode, which is controlled by several parameters, including: surface energy of the film σ_f^s , surface energy of the substrate σ_s^s , interface energy of the film-substrate σ_{fs} , and the strain energy density v_s. Several possible growth modes are listed below [43]:

Volmer-Weber growth Islands of the film grow initially and gradually join together. It occurs when the interface energy is large, and hence the film does not wet the substrate surface, e.g $\sigma_{fs} > \sigma_f^s + \sigma_s^s$.

Frank-van der Merwe growth The film grows one layer after another, which is often the preferred way for creating heterostructures. It takes place when the interface energy is small, hence the film wets the substrate, e.g $\sigma_{fs} < \sigma_f^s + \sigma_s^s$.

Stranski-Krastinov growth The film grows layer-by-layer in the beginning, but transfers to 3D growth after a certain thickness. It usually takes place when the film is highly strained, since the strain energy increases with the film thickness.

Step flow growth The film grows along the edge of pre-existing step-terraces, which have good affinity with the ad-atoms. Density of the steps on the substrate is related to the miscut angle. Step-flow growth can give rise to high quality films. However, the lack of any change in surface topology during the growth make it difficult to monitor the process *in situ*.

The requirements for each case listed above are for equilibrium conditions, whilst in reality the growth process can be far from equilibrium. Frank-van der Merwe growth, also referred as layer-by-layer growth, is required for creating high quality films with atomically sharp and flat interfaces. The layer-by-layer growth should take place when depositing a material the same as the substrate, since the interface energy σ_{fs} is effectively zero. In heteroepitxial growth, the mismatch of lattice constants between the film and the substrate causes interface strain. The film may start with layer-by-layer growth, but the elastic energy increases with increasing film thickness. Misfit dislocations become energetically favourable to form after reaching a critical thickness. This gives rise to island growth. In addition, surface/interface energies can vary significantly for different lattice planes, hence the growth mode is also affected by the orientation of the substrate.

Pulsed-laser deposition (PLD) [44, 45, 1] is one of the PVD techniques that are commonly used for oxide thin films. A schematic of typical PLD system is shown in Fig. 2.1. A high power pulsed-laser is focused on a target, which is made of the same stoichiometry as the desired film. The surface of the target is ablated by laser shots, typically lasting for tens of nanoseconds. A plasma is created and subsequently expands, ejecting the species normal

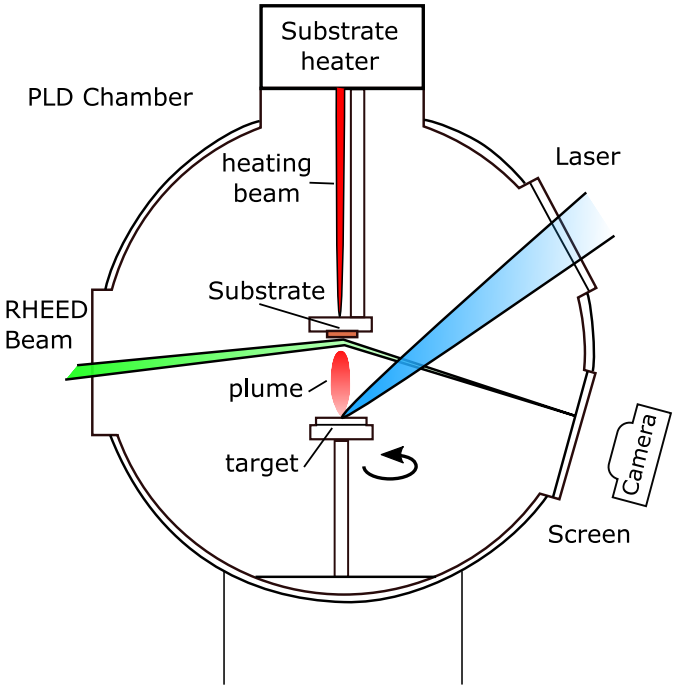

Fig. 2.1 A schematic of a PLD depostion system with RHEED monitoring.

to the surface. Visually, a plume can be seen in the UHV chamber. Ejected species interact with the background atmosphere, and arrive at the substrate with high kinetic energies. PLD is suitable for growing oxides since it allows an oxygen atmosphere to be used, which has two functions. First, it helps the film to have the correct stoichiometry, since oxygen tends to be lost in a high vacuum. Second, the background pressure influences the kinetic energies of the atoms arriving at the film surface. The rate of collisions between the ejected species and gas molecules increases with increasing pressure. If the kinetic energy is too high the ejected species may sputter the existing surface and affect the final morphology. The substrate is usually heated to 500°C to 900°C for promoting surface diffusion and formation of crystalline phases.

Another advantage of PLD compared with other vapour deposition techniques is that high supersaturation can be achieved [46], since ablated species arrive at the film at a very high rate within a very short amount of time. Laser shots typically last tens of nanoseconds [47], although the plume propagation takes longer. Supersaturation provides extra driving force for the nucleation and the growth processes, thereby improving the film quality.

The process of film growth can be monitored using surface characterising techniques such as reflection high-energy electron diffraction (RHEED) [48]. It is also shown in Fig. 2.1. A camera is used to record the fluorescence of the diffracted electrons. The Ewald sphere construction may be used to relate the diffraction pattern with the surface topography.

Because the electron beam only interacts with a few surface layers, the reciprocal lattice points turn into vertical rods, giving vertical streaks in the diffraction pattern if the surface is atomically smooth. On the other hand, a rough surface with islands results in a 2D array of diffraction spots. During layer-by-layer growth, the surface roughness is lowered initially, but recovers when a single layer is completed. The periodic oscillations of the spot intensity can be used for tracking the number of unit cells that have been deposited, which is essential for making superlattices.

Thin film deposition is a complex process, and it is difficult to find out exactly how the films are formed *in situ*. Practically, experimental procedures and parameters have to be optimised, which include (but are not limited to): target composition; substrate temperature and surface treatment; laser type, spot size, fluence and repeat rate; the type of background atmosphere and partial pressures. The quality of the resulting films can be checked *ex situ* using X-ray diffraction, atomic force microscopy and transmission electron microscopy. Fabricating high quality films and interfaces requires a considerable amount of knowledge, experience, and time.

2.2 Ionic conduction at planar interfaces

Ion conducting materials are widely used in energy applications, such as Li/Na ion batteries and fuel cells. The continuing demand for highly ionic conductive materials for energy applications has attracted great research interest. Sata et al. [49] reported orders of magnitude enhancement in F^- conduction in CaF_2/BaF_2 heterostructures, caused by overlapping space-charge regions. This effect is, however, difficult to realise in oxygen ionic conductors since they often have very small space-charge zones as a result of extrinsic doping.

In 2008, Garcia-Barriocanal et al. [11] reported an eight orders of magnitude enhancement in ionic conductivity using yittra-stablised zirconia (YSZ)/$SrTiO_3$(STO) interfaces. YSZ adopts a cubic fluorite structure and is widely used as an oxygen ion conductor. This, however, was a controversial claim, and the exact natural of the observed conductivity was debated in subsequent studies [30, 29, 50, 51, 31]. It is likely that the original conductivity enhancement observed was electronic in nature, caused by the STO substrate [31]. Nevertheless, the possibility of having enhanced ionic conductivity at interfaces has sparked theoretical and computational investigations of the fluorite-perovskite systems.

Thin film interfaces can induce a significant amount of lattice strain, and hence affects a range of properties [52]. Lattice parameters between two different materials often do not match fully. The elastic energy induced scales with the volume, and usually a few percent of biaxial strain can be maintained in very thin films. In the fluorite structure, oxygen anions

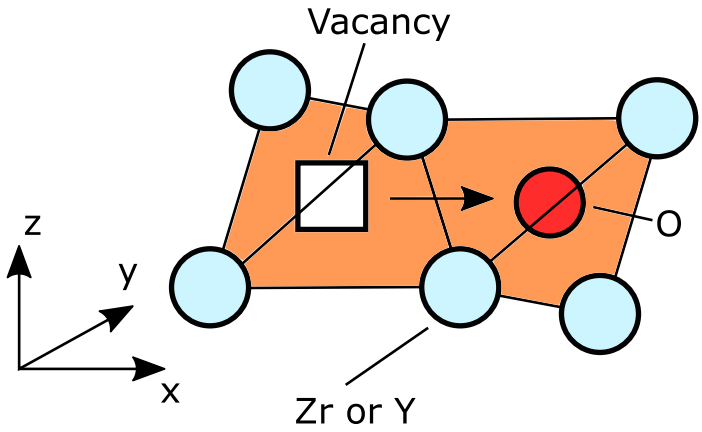

Fig. 2.2 A schematic of the vacancy hopping process. The oxygen anion (red) has to squeeze through two metal cations. Its movement is opposite in direction to that of the vacancy.

are tetragonally coordinated with metal cations, as shown in Fig. 2.2. A single *hop* of the oxygen vacancy to the nearest neighbour site requires the anion to squeeze through a gap between the two metal cations, which involves overcoming an energy barrier. The process is thermally activated, and the barrier height contributes to the activation energy E_a, hence strongly affects the conductivity. Intuitively, tensile straining should make this process easier, since the cations are further apart. Kushima et al. [53] studied the migration barrier in YSZ using first-principles calculations and found that ionic conductivity does not monotonically increase, but instead peaks at about 6% strain. This was explained by stronger oxygen-cation bonding in the relaxed structure with large tensile strain applied. A similar trend with strain was found by Souza et al. [54] for in-plane vacancy migrations in CeO_2. They employed a constant pressure empirical pair-potential model and showed that the migration volume also increases with increasing strain, giving increased enthalpy of migration. In both cases, the authors predicted possible enhancements of ionic conductivity of up to four orders of magnitude.

Alternative phases can be stabilised via strain - a columbite phase of ZrO_2 is found to be more stable than the fluorite phase under 7% tensile strain [55, 56]. Thorough exploration of the configuration space is need for theoretical investigations under unconventional conditions. *Ab initio* molecular dynamics (AIMD) simulations performed using unstable phases may give exaggerated results - the observed anion disordering and diffusion may in fact result from the

phase transition [57–59]. AIMD calculations can be computationally very demanding, hence simulations are mostly limited to small simulation cells and short timescales.

Studies of the strain effect usually neglect the atomic structure of the interface. The fluorites and perovskites have different crystal structures, and reconstruction is highly likely to occur in order to accommodate the mismatch [50]. Dyer et al. [60] used first-principles methods to study the YSZ/STO interface. They found placing a rock-salt ZrO layer at the interface could lead to structures of lower energies. However, their work examined only a few of the many possible interface structures. A more rigorous way is to treat the interface structure as unknown and systemically search for low energy structures. Cheah et al. [56] studied ultra-thin ZrO_2/STO superlattices using an interatomic potential based genetic algorithm search method developed in their previous work of grain boundaries in STO [61]. They found several new phases of ZrO_2 emerging as a result of both structural mismatch and strain. A later work from the same authors included yttria dopants in the search, and found the stable structure did not promote ionic conductivity. However, the ultrathin superlattice structures they studied can be very difficult to realised in experiment, and the exact structure of conventional planar fluorite-perovskite is still not fully understood to date. In Chapter 6, random structure searching is performed to predict the structure of CeO_2/STO planar (001) interfaces, which are more practical to make due to reduced interface strain.

2.3 Vertically Aligned Nanocomposites

Planar epitaxial interfaces formed by functional oxides can induce unexpected properties [62, 4]. However, creating these interfaces requires delicately controlled conditions for layer-by-layer growth. The strain state of the film is dominated by the substrate, because the latter is orders of magnitude thicker. This limits the inter-layer strain coupling in multi-layer heterostructures. In addition, thick films with high quality are difficult to fabricate, as a result of inevitable lattice relaxation and increase of surface roughness during the growth.

Vertically aligned nanocomposites [63, 64] offer an alternative geometry to achieve coupling of functional properties and emergent interface effects. They have been developed in parallel with the continuing research on planar heterostructures. A comparison between the conventional planar heterostructure and VAN films can be found in Fig. 2.3. VANs are formed during deposition through self-assembly - a process that is commonly found in organic solids [34]. Pulsed-laser deposition (PLD) is usually used for making VANs. In contrast with their complex nanostructures, depositing VAN films is relatively straightforward and only needs a single target with the desired overall stoichiometry. Growth monitoring

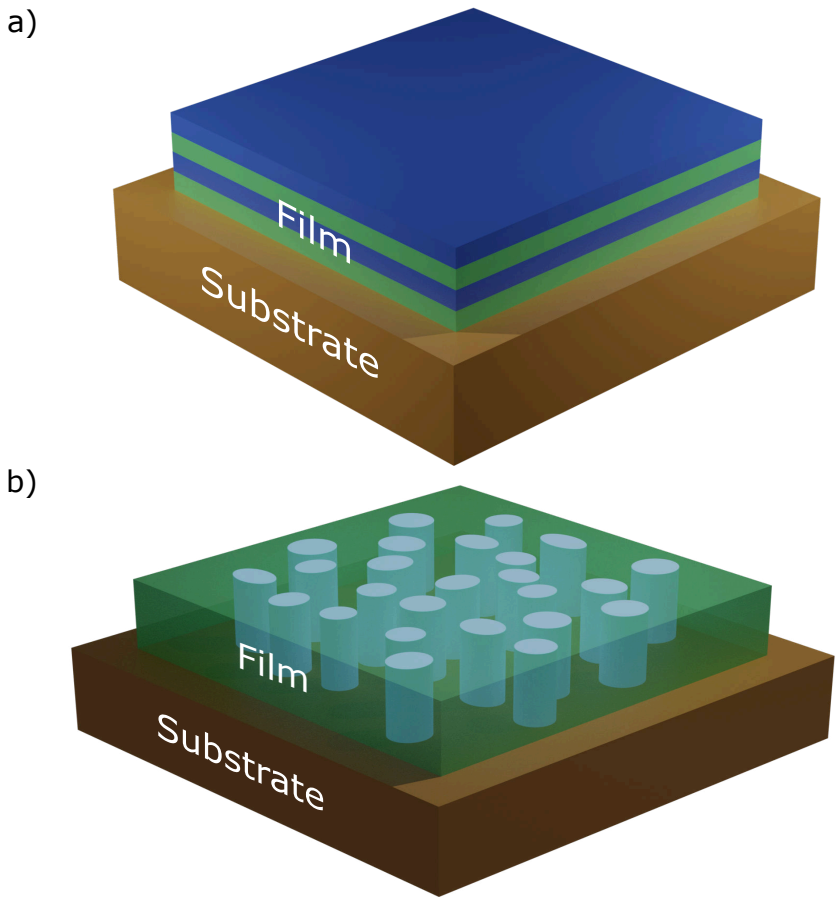

Fig. 2.3 Schematics of planar heterostructures (a) and vertically aligned nanocomposites (b).

techniques, such as Reflection High Energy Eelectron Diffraction (RHEED), are not required either.

2.3.1 Different nanostructured forms

The phases forming the pillar-matrix structure need to satisfy several criteria. They should have different crystal structures, allowing well-defined phase boundaries (interfaces) to be formed. The two phases should also be immiscible, i.e. they do not form solid solutions, even at high temperature. This is required for the nucleation-and-growth mechanism. At the beginning of the deposition, the phase that wet with the substrate grows layer-by-layer. The other phase, being less compatible, often adopts the island growth mode. As a result, the former makes the matrix, and the latter becomes the pillars. In practice, the matrix phase is often chosen to have the same crystal structure as the substrate. It is also desirable to

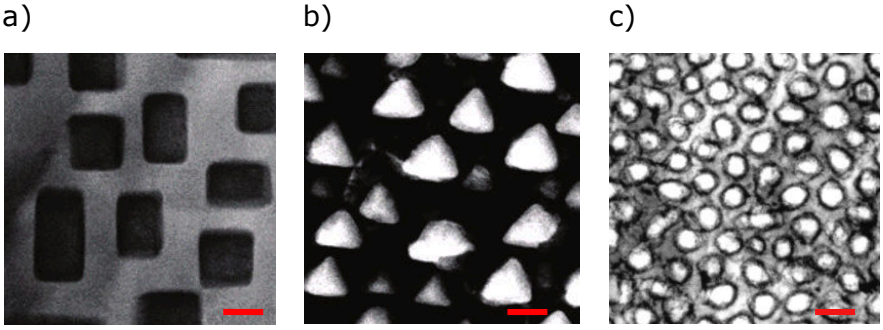

Fig. 2.4 Plan-view TEM images of: a) CFO-BFO on STO(100); b) CFO-BFO on STO(111); c) CFO-BTO on STO(100). Reprinted (adapted) with permission from a&b) Ref [67] and b) Ref [68]. Copyright (2006) American Chemical Society. Copyright (2004) AIP Publishing. Scale bar: 50 nm

chose compositions such that the elements from one are not common dopants for the other, otherwise the formed phases may not be pure.

Spinodal decomposition allows VANs to be formed with two phases that are miscible only at high temperatures [34]. This process results in highly ordered chequerboard pattens of pillars. Example systems with this behaviour are $BiFeO_3/Sm_2O_3$ and $(La,Sr)MnO_3/ZnO$ [65].

The shapes of the pillars are related to surface and interface energies of the pillar and matrix phases. For example, in the $BiFeO_3$(BFO)/$CoFe_2O_4$(CFO) VAN grown on STO (001) substrate, CFO pillars are pyramid shaped and grow out of the plane. This can be explained by their {111} surfaces having a lower energy [66]. Within the film, interfaces are formed between CFO(110)//BFO(110), giving rectangular shaped cross-sections, which can be seen in Fig. 2.4a. The nanostructure is also affected by the substrate orientation. When grown on STO(111) substrate, BFO forms the prism shaped pillars embedded in the CFO matrix [67], as shown in Fig. 2.4b. Replacing BFO by $BaTiO_3$(BTO) removes the facets, and the CFO pillars becomes cylindrically shaped [68], shown in Fig. 2.4c. This can be explained by the kinetics during self-assembly. BTO has high melting temperature (1625°C vs 1255°C), hence formation of facets is inhibited by the slow diffusion rate.

In planar heterostructures, the strain energy density is proportional to the thickness of the film. As the film grows, it becomes energetically favoured to relax the strain at the cost of increased interface energy (from misfit dislocations). The same principle holds true in VANs, but the interfaces are vertically orientated. Hence, the effective "thickness" for these interfaces is the lateral size of the pillars, which is independent of the actual film

thickness. The ability to maintain strain throughout thick composite films can be utilised to enhance superconducting T_c [69], ferroelectricity [70], magnetoelectric coupling [71] and ionic conductivity [72].

VANs typically have much higher interface-to-volume ratios r_s than planar heterostructures. To illustrate this, let's consider a VAN film with two phases: A and B, where A is the pillar phase, and B forms the matrix. For simplicity, it is assumed that the cross-sections of the pillars are square-shaped with edge length a. The pillars take a volume fraction of f. For a film with base area A and thickness H, the following equation can be written considering the total volume of pillar phases:

$$AHf = Ana^2H\,, \tag{2.1}$$

where n is the number density of the pillars. The interface-to-volume ratio r_s is given by:

$$r_s = \frac{An4aH}{AHf} = \frac{4an}{f}\,. \tag{2.2}$$

Rearranging equation (2.1) gives:

$$\frac{n}{f} = \frac{1}{a^2}\,. \tag{2.3}$$

Substituting this into the expression of r_s above gives:

$$r_s = \frac{4}{a}\,. \tag{2.4}$$

For comparison, a planar bilayer heterostructure of the same thickness has an interface-to-volume ratio given by $\frac{1}{H}$. Hence, one can deduce the enhancement factor for the VAN geometry as:

$$b_e = \frac{4H}{a}\,. \tag{2.5}$$

The term $\frac{H}{a}$ is the aspect ratio of the pillars. The enhancement factors for a range of film thicknesses and pillar sizes are tabulated in Table 2.1. Typically, an increase of one or two orders of magnitude in the interface-volume ratio can be achieved in VANs.

2.3.2 Ionic conducting VANs

Ions carry charges and give rise to currents as they move collectively. However, the speed at which ions can move in solids is often orders of magnitude smaller than that of electrons. The demand of highly ionic conductive materials for energy applications has led to investigations of the effects of planar heterostructure on ionic conductivity, described in section 2.2.

Table 2.1 Typical enhancement factor of the interface area between planar and VAN films.

File thickness H (nm)	Pillar Size a (nm)	Enhancement b_e
100	20	20
200	20	40
300	20	60
100	50	8
200	50	16
300	20	24

The existence of exposed vertical interfaces, and the ability to maintain strain make VANs ideal for studying nanoscale ionics with great potential for device integrations [73]. Tuning ionic conductivity via strain engineering was demonstrated in $SrZrO_3$/RE_2O_3 VAN films [72]. RE varies among Sm, Eu, Gd, Dy and Er, and changes the lattice parameter of the RE_2O_3 pillars, hence controlling the out-of-plane strain of the $SrZrO_3$ matrix phase. The conductivity was found to increase with increasing tensile strain in consistent with the theoretical studies [54, 53]. Yang et al. [33] studied Sm-doped-$CeO2_2$(SDC)/STO nanocomposite films and reported enhancement of out-of-plane ionic conductivity of up to two orders of magnitude [32]. A related work by Lee et al. [33] found similar enhancements in YSZ/STO VAN films templated on a SDC/STO VAN film. In both cases, the enhancements are attributed to the improved crystallinity of the pillar phases.

Ionic conducting VAN films also have promising applications in resistive switching (RS) memory devices [74]. The current technology for random access memory (RAM) in computers, namely the dynamic random access memory (DRAM), stores bits of data in memory cells each consisting of a capacitor and transistor. Data stored by DRAM is volatile. The electric charge leaks overtime, and periodic refreshes are required. The resistive switching phenomenon can be utilised for making memory devices that are non-volatile, with fast access speed and low energy consumption [75]. The movement of ions can open or close electronic conducting channels [76]. However, the conducting channels must be created by high voltage electro-forming processes, which leads to unpredictable device performance. VAN films can realise forming-free RS devices. The vertical interfaces act as the conducting channel, and the ionic movements tune the electronic conduction by altering the Schottky barrier. This behaviour has been observed in SDC/STO and Sm_2O_3/STO VANs [77, 74].

Despite novel properties of VAN films being linked to the vertical interfaces, directly or indirectly, they remain largely unexplored by theoretical and computational studies. The two phases forming the interface have different crystal structures, and often significant lattice mismatching exists. The lack of understanding of the vertical interfaces in Ref [33, 32]

motivated the investigation presented in Chapter 5, where structures of STO(100)//CeO_2(110) vertical interfaces are determined using random structure searching and subsequently studied.

2.4 Current research on interface structure prediction

Knowing the atomic structures of interfaces is essential for any computational studies. However, interface structures are often not known in the first place. Because interfaces have small sizes, and they are buried inside the material, determining their structures can be challenging experimentally. The conventional way is to use scanning transmission electron microscopes to capture images that show columns of atoms. However, these micrographs are 2D projections of the 3D lattices, and often do not have enough contrast to determine the exact identities of the atoms. As a result, the images have to be backed up by atomistic models that are constructed with human intuition, and then fitted to the images [78, 79]. An alternative approach is to find interface structures directly using computational methods. In this section, the existing studies involving predicting interface structures are described. General details of structure prediction can be found in Chapter 4.

Many of the existing works investigate grain boundaries, whose structures cannot be inferred trivially from that of the bulk phases. Silicon grain boundaries are relatively simple but technologically important. von Alfthan et al. [80] proposed a protocol to study the twist grain boundaries of silicon that involves randomly removing atoms within a slab containing the interface, since the interfaces may have different atomic densities. It is followed by molecular dynamics simulations under very high temperature to melt the interface region and remove any initial ordering. Afterwards, the system is quenched to a lower temperature, followed by a gradual reduction of temperature for reaching low energy configurations. Many ordered low energy structures have been found using this approach. Chua et al. [61] studied high angle symmetric $\Sigma(111)[\bar{1}10]$ and $\Sigma(112)[\bar{1}10]$ grain boundaries in $SrTiO_3$ using a genetic algorithm. Instead of defining a fixed region containing the interface structure, they used an order parameter to quantify whether an atom is in a disordered environment, e.g. near the interface. The order parameter controls the mutation and exchange steps, and hence reduces the chance of altering the bulk regions. The interface stoichiometry was explored by varying charge neutral units of TiO_2 and SrO included in the initial structures. Both Ref [61] and Ref [80] started with empirical interatomic potentials for searching or molecular dynamics runs, followed by refinement of results using first-principles methods. This is for practical reasons: DFT calculations are relatively expensive for large unit cells. Another problem is that the energy/force evaluations have to be performed in serial, one time step after another, in molecular dynamics simulations. This can result in long wall-times for the

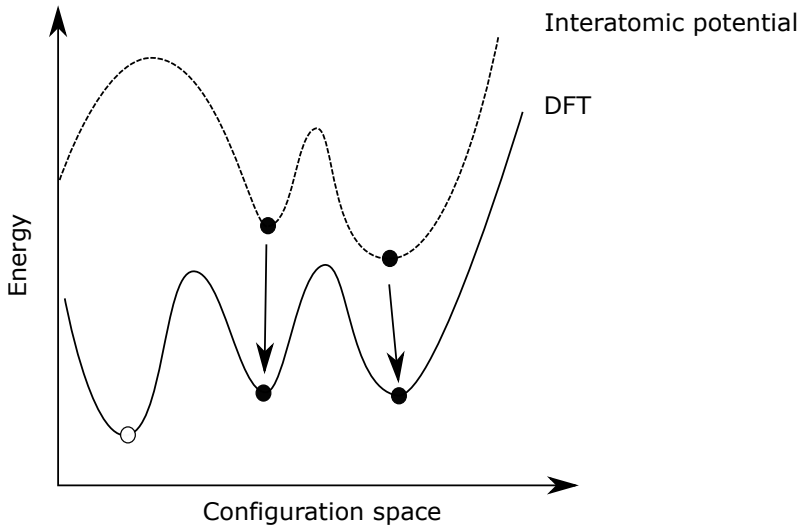

Fig. 2.5 A schematic to illustrate that additional local minima in the PES of DFT can be missed if structure searching is performed using interatomic potentials.

molecular dynamics runs. Population based search methods, such as genetical algorithms, can be parallelised within each generation, although the evolution of the generations is still sequential and must be performed iteratively. In both cases the empirical potentials give results that qualitatively agree with that of DFT refinements, which suggests the former are reasonably transferable for interface environments. Methods involving machine learning have also been proposed for predicting grain boundary structures [81–83].

The genetic algorithm method developed by Chua et al. was applied in a study of ZrO_2/STO ultra-thin supercells with 1.5 units of ZrO_2 sandwiched between STO layers [56]. The authors found a range of non-fluorite phases to be stabilised due to both strain and the structural mismatch. ZrO_2 is under about 7% biaxial tensile strain when one-to-one matched to STO (001) surface. A columbite bulk phase is more stable under this strain state [55, 59]. However, the anatase structured ZrO_2 is found to be most stable in the superlattice environment. A follow-up of this work studied YSZ/STO ultra-thin supercells and found a 'quasi-cubic' YSZ phase to be stable [84]. However, molecular dynamics simulations suggest this phase does not give any enhancement in long-range ion diffusivity, in contrast to what was claimed experimentally [11]. Ultra-thin supercells are an extreme case in theoretical studies, as there is effectively no bulk region being included. In reality, such heterostructures may not be practical to fabricate.

The protocol of performing searches with interatomic potentials followed by DFT refinement can potentially miss local minimum that are only present in the potential energy surface of first-principles calculations, as illustrated in Fig. 2.5. Refining the results with

DFT calculations only gives more accurate descriptions for the particular input structures. In addition, there is no guarantee that interface potentials, which are typically fitted to individual bulk phases, behave correctly at interfaces.

It is desirable to search directly on the potential energy surface (PES) using first-principles calculations. Xiang et al. [85] studied Si/Al_2O_3 interfaces using the basin hopping algorithm with first-principles calculations . However, their search only included a single interfacial layer of Si atoms, and most of the structures are kept fixed during geometry optimisations. An indirect approach is to adaptively fit the empirical potentials to DFT calculations, as proposed by Zhao et al. [86] for predicting STO $\Sigma(112)[\bar{1}10]$ grain boundary structures. Genetic algorithm searches using the potentials are repeated. The potentials are updated at the end of each search using the results of DFT relaxation of the output structures. The inclusion of two loops in the algorithm makes it complex and potentially sensitive to ad-hoc parameters. The quality of fitted potentials and whether they are representative of the true DFT potential energy surface is difficult to prove. Nevertheless, the algorithm appeared to work well for STO.

Schusteritsch et al. [87] performed first-principles searches of grain boundary structures for graphene and $SrTiO_3$ using *Ab initio* Random Structure Searching (AIRSS). AIRSS is the method that has been used in the studies presented in Chapter 5 and Chapter 6, and more details can be found in Chapter 4. The authors found previously unknown stable interface configurations of the graphene zig-zag boundaries. Interestingly, these structures were later observed experimentally using electron microscopy [88]. The search for $SrTiO_3$ $\Sigma(111)[\bar{1}10]$ grain boundary structures found long-range distortions that propagate into the bulk, which is not observed by Chua et al. [61]. Several new structures with lower energy were also reported, highlighting the importance of performing first-principles searches directly. Note that the interatomic potentials predict a cubic $Pm\bar{3}m$ ground phase for STO, while the stable phase in DFT is tetragonal and have space group $I4/mcm$ with a $a^0a^0c^-$ octahedral tilt pattern.

The random searching method used by Schusteritsch et al. forms the foundation of interface searching methods used in this thesis. Unlike grain boundaries, the thin film interfaces studied in this thesis are formed by two materials with different chemical compositions and crystals structures. This results in additional challenges for setting up the initial models, and more interface terminations and stoichiometries need to be explored. The increased number of chemical species means the configuration space is more complex. In Chapter 5, domain-matched vertical interfaces are studied using random searching with interatomic potentials. This is because the simulation cells embedding interfaces are too computationally expensive for DFT calculations. Interatomic potentials are shown to give qualitatively correct results

in similar systems [61, 56]. In Chapter 6, structures of planar epitaxial interfaces formed between STO and CeO_2 are predicted using first-principles random structure searching, as a range of terminations and off-stoichiometry cases need to be included. More details about the interface searching methodology used can be found in Section 4.3.

2.5 Octahedral tilting in perovskites

Moving away from interfaces related topics, this section gives a brief introduction about the tilted octahedra in perovskites, which are closely coupled with their properties. Perovskite structured oxides have a general formula of ABO_3. The A and B sites are often occupied by metal cations, whose charge numbers add up to six to balance that of the oxygen anions. The A site can have an ionic charge of $+1$, $+2$, $+3$ with the corresponding B site charge being $+5$, $+4$, $+3$. The B site is occupied by ions with relatively small radii, which are coordinated by octahedra of oxygen anions forming a vertex sharing network. Cations at the A sites are 12-fold coordinated. It is common to view them as if they fill the voids between the octahedra. A model of the perovskite structure is shown in Fig. 2.6. Note the radii of anions are reduced for clarity.

The structural stability of perovskites can be quantified using the Goldschmidt tolerance factor:

$$t = \frac{r_A + r_o}{\sqrt{2}(r_A + r_B)}, \tag{2.6}$$

where the r_A, r_b are the ionic radii of the cations occupying A and B sites respectively, and r_o is the radii of the oxygen anion. The tolerance factor can be rationalised by considering an idea perovskite structure with ions being hard spheres that are just touching each other, which corresponds to having $t = 1$. The tolerance factor may deviate from one, giving distorted perovskite structures. Having $t > 1$ implies that the B site ions are too small, or that the A site ions are too big. This gives rise to displacements of B site ions away from the centre of the octahedra, breaking the inversion symmetry, and results in a net dipole moment. An example of this is $BaTiO_3$. Structures with $t < 1$ usually have distortions making the lattice orthorhombic or rhombohedral. The A site ions are not big enough to fill interstitials of the octahedral network. This gives rise to octahedral tilting, which reduces the distances between B site ions.

Classifications of tilted octahedra was pioneered by Glazer [36]. Using geometry arguments, it was shown that there are 23 tilt systems. Because the primitive unit cell varies with the tilt pattern, the notation describing the tilt is defined along the three pseudo-cubic directions. The Glazer notation has a form "$a^{+/-/0}b^{+/-/0}c^{+/-/0}$, where a, b and c represent

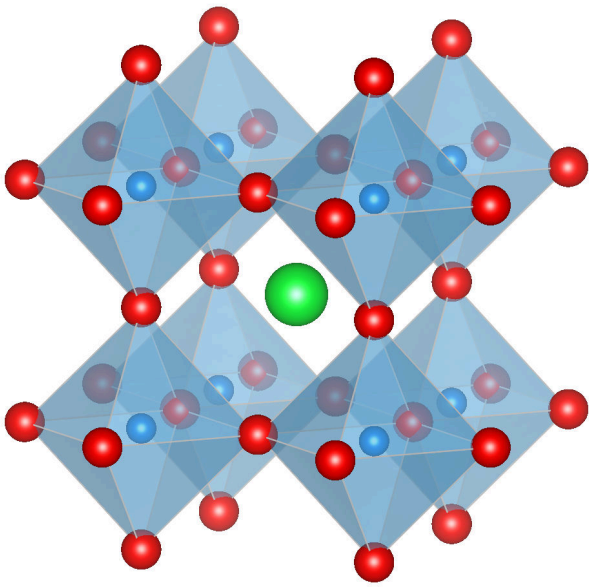

Fig. 2.6 A model perovskite structure with a corner-connecting BO_3 octahedra network. Colour code: *A*-green, *B*-blue, *O*-red.

the magnitude of the rotation along the three pseudocubic directions. The superscripts describe whether the rotation is in-phase or out-of-phase while looking down the corresponding directions, and ^{0} indicates there is no tilt. For example, the undistorted cubic case is written as $a^0a^0a^0$, and $a^0a^0c^-$ means octahedral tilt out-of-phase along only one pseudocubic direction. Note that there can be redundancy regarding the use of Glazer notation. For example, $a^0a^0c^-$ is equivalent to $a^0a^0b^-$. Not all 23 tilt systems have been observed experimentally. It is possible that some cases are too ideal, and in reality there are always extra distortion modes. One of the significance of Glazer's work is that it shows some space groups have only one unique tilt pattern, which allows the determination of the distortion mode though x-ray diffraction measurements, despite relatively weak contributions from oxygen atoms. A later work by Howard et al. [89, 90] uses group theory analysis listing 15 distinct rotation patterns and corresponding space groups . The group-subgroup relationships of different cases are shown in Fig. 2.7.

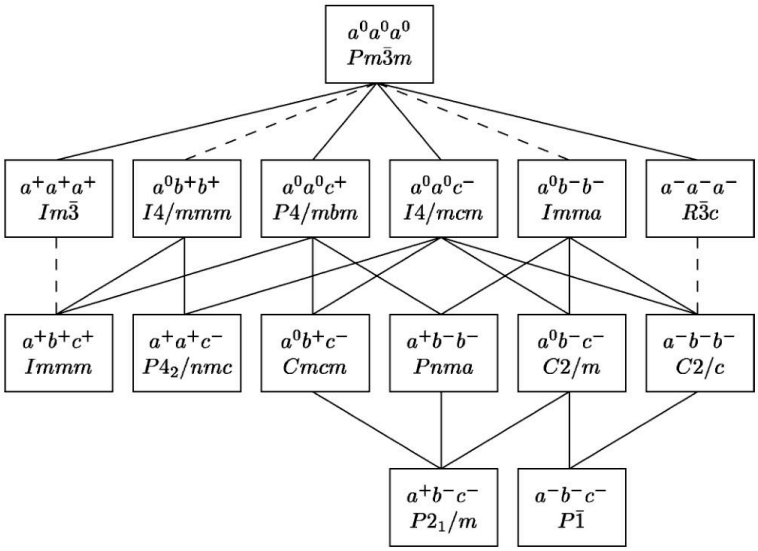

Fig. 2.7 Space group and sub-group relationships for a range of rotation patterns. Reproduced with permission of the International Union of Crystallography from Refs [89, 90].

Chapter 3

Methodology

This chapter aims to give background on the theoretical and computational methods used in this thesis. We start with the theory of *ab initio* materials modelling, which was the primary tool for the investigations performed, due to its transferability. It is followed by a brief summary of the interatomic potential methods, which are used in the works presented in Chapter 5 and Chapter 6. Whilst being less transferable, these are very useful for investigating large systems that are beyond the reach of first-principles methods due to computational costs. The final section describes how interfaces are modelled and embedded in simulation cells with periodic boundaries.

3.1 *Ab initio* theory of materials

Most of the quantum mechanics describing the microscopic world was developed in the early part of the 20th century. While the theory was shown to be highly accurate [91], directly solving the seemingly simple Schrödinger equation for everyday materials turns out to be very challenging [92]. Approximations have to be made in order to keep problems computationally tractable. The particular approach considered here is Density Function Theory (DFT). While the mathematical foundations were laid in the 1960s [93], its wide spread use has been more recent, thanks to the ever-increasing computational power, and the development of computer codes that implements robust and efficient algorithms [94, 95].

DFT is a first-principles method that models a system directly through quantum mechanics. The input for a calculation are the identities and coordinates of the atoms in the system, from which a vast number of physical and chemical properties can be obtained. The method excels in transferability - all chemical environments can be treated under the same framework, without free-parameters to adjust.

In this section, the background of electronic structure theory and derivations leading to the formulation of DFT are outlined. A full review of this field is, of course, beyond the scope of this work. For more details, intrigued readers are referred to the literature [96–98].

3.1.1 The Schrödinger equation

The time-independent Schrödinger equation may be written as:

$$\hat{H}\psi = E\psi, \tag{3.1}$$

where $\hat{H}$ is the hamiltonian for the system of electrons and nuclei, ψ is the many-body wave function, and E is the total energy of the system. The hamiltonian $\hat{H}$ contains several terms:

$$\hat{H} = -\frac{\hbar^2}{2m_e}\sum_i \nabla_i^2 - \sum_{i,j}\frac{Z_I e^2}{|\mathbf{r}_i - \mathbf{R}_i|} + \frac{1}{2}\sum_{i\neq j}\frac{e^2}{|\mathbf{r}_i - \mathbf{r}_j|} - \sum_i \frac{\hbar^2}{2M_I}\nabla_I^2 + \frac{1}{2}\sum_{I\neq J}\frac{Z_I Z_J e^2}{|\mathbf{R}_I - \mathbf{R}_J|}, \tag{3.2}$$

where i and j index electrons and I, J index nuclei. Since the electrons are much lighter and move much faster than the nuclei, the system can be decoupled. This is the Born-Oppenheimer approximation [99], which states ions can be regarded as "frozen" in-place, and the electronic structure adapts instantaneously to any motion of the ions. In this approximation, the electronic hamiltonian is:

$$\hat{H} = \hat{T} + \hat{V}_{ext} + \hat{V}_{int} + E_{II}, \tag{3.3}$$

where $\hat{T}$ is the kinetic energy of the electrons, $\hat{V}_{ext}$ is the potential felt by the electron from the nuclei, and $\hat{V}_{int}$ is the energy due to electron-electron interactions. The last term E_{II} is the nucleus-nucleus Coulomb energy, which is included as a constant.

Analytical solutions of the electronic Schrödinger equation are limited to a few simple cases, including hydrogen, H_2^+ and homogeneous electron gas. This is due to the electron-electron interaction ($\hat{V}_{int}$) term, which results in the probability of finding a given electron at a position $\mathbf{r}$ to depend on the positions of all other electrons in the system. The many-body wave function itself is also difficult to represent or even store. For an example, a system of N particles needs a many-body wave function that has $3N$ dimensions. If the wave function is stored on a $10 \times 10 \times 10$ grid, 1000^{3N} floating-point numbers are needed. This exponential scaling is referred as the *curse of dimensionality* [100].

3.1.2 Hartree and Hartree-Fock approximations

Directly solving for the many body wave function is exceedingly challenging, and approximations have to be made. The Hartree method [101] uses an *ansatz*, stating the wave function of N electrons can be written as the product of N single electron wave functions:

$$\psi(\mathbf{r}_1, \mathbf{r}_2, ...\mathbf{r}_n) = \psi_1(\mathbf{r}_1)\psi_2(\mathbf{r}_2)...\psi_n(\mathbf{r}_n)\,. \tag{3.4}$$

It is assumed the electrons are independent, and interact only though a mean-field potential. The one-electron Schordinger equation takes the form:

$$\hat{H}_{eff}\psi_i(\mathbf{r}) = \Big[-\frac{\hbar^2}{2m_e} + V_{eff}(\mathbf{r})\Big]\psi_i(\mathbf{r}) = \varepsilon_i\psi_i(\mathbf{r})\,, \tag{3.5}$$

where ψ_i is a single-particle wave function of electron i (omitting spin) and $V_{eff}(\mathbf{r})$ is an effective potential:

$$V_{eff}(r) = V_{ext} + \int d\mathbf{r}' n(\mathbf{r}')\frac{1}{|\mathbf{r}-\mathbf{r}'|}\,. \tag{3.6}$$

The first term of V_{eff} is the external potential arising from the nuclei plus any other fields. The second term is the Coulomb repulsion arising from the mean-field electron density. Equations in this form will be revisited in the Kohn-Sham equation of the density functional theory later*.

One major drawback of the Hartree approximation is that the wave function in (3.4) is not anti-symmetric upon exchange of particle labels, e.g $\psi(...\mathbf{r}_i...\mathbf{r}_j...) = -\psi(...\mathbf{r}_j...\mathbf{r}_i...)$, which is required by the fermionic nature of electrons. The solution is to construct the full wave function from the Slater determinant:

$$\Phi = \frac{1}{\sqrt{N!}}\begin{vmatrix} \phi_1(\mathbf{r}_1,\sigma_1) & \phi_2(\mathbf{r}_1,\sigma_1) & \cdots & \phi_N(\mathbf{r}_1,\sigma_1) \\ \phi_1(\mathbf{r}_2,\sigma_2) & \phi_2(\mathbf{r}_2,\sigma_2) & \cdots & \phi_N(\mathbf{r}_2,\sigma_2) \\ \vdots & \vdots & \ddots & \vdots \\ \phi_1(\mathbf{r}_N,\sigma_N) & \phi_2(\mathbf{r}_N,\sigma_N) & \cdots & \phi_N(\mathbf{r}_N,\sigma_N) \end{vmatrix}., \tag{3.7}$$

where $\phi(\mathbf{r}_i,\sigma_i)$ are single particle wave functions (spin-orbitals) with σ being the spin variable. The Hartree-Fock method uses a single Slater determinant to represent the wave

*The electron-electron Coulomb term in the original paper [101] has orbital dependence. The later Hartree-Fock method removed it, since the self-interaction is cancelled out.

function[102]. Applying the electronic hamiltonian to the wave function Φ gives:

$$\langle\Phi|\hat{H}|\Phi\rangle = \sum_{i,\sigma}\int d\mathbf{r}\,\psi_i^{\sigma*}(\mathbf{r})\left[-\frac{1}{2}\nabla^2 + V_{ext}(\mathbf{r})\right]\psi_i^{\sigma}(\mathbf{r}) + E_{II} \tag{3.8}$$

$$+\frac{1}{2}\sum_{i,j,\sigma_i,\sigma_j} d\mathbf{r}d\mathbf{r}'\,\psi_i^{\sigma_i*}(\mathbf{r})\psi_j^{\sigma_j*}(\mathbf{r}')\frac{1}{|\mathbf{r}-\mathbf{r}'|}\psi_i^{\sigma_i}(\mathbf{r})\psi_j^{\sigma_j}(\mathbf{r}') \tag{3.9}$$

$$-\frac{1}{2}\sum_{i,j,\sigma} d\mathbf{r}d\mathbf{r}'\,\psi_i^{\sigma*}(\mathbf{r})\psi_j^{\sigma*}(\mathbf{r}')\frac{1}{|\mathbf{r}-\mathbf{r}'|}\psi_i^{\sigma}(\mathbf{r})\psi_j^{\sigma}(\mathbf{r}'), \tag{3.10}$$

where the fourth term is the exchange energy, which accounts for the quantum mechanical effect of the Pauli's exclusion missing in the Hartree approximation. Note that the $i = j$ contributions cancelled between the third (pair-wise Coulomb interaction) and the fourth (exchange interaction) terms, making this hamiltonian free from self-interaction.

The Hartree-Fock method includes the exchange effect through the anti-symmetrical wave function, and is successful for a few cases. However, it still lacks the correlation effect of truly many-body interactions. The correlation energy is generally defined as the energy difference between the Hartree-Fock result and the *exact* energy of the interacting system. The accuracy of the Hatree-Fock method can be improved by using a linear combination of Slater determinants.

3.1.3 Density functional theory

The wave function describes the state of the quantum mechanical system, but it is not a physical observable. The electron density, on the other hand, is a measurable quantity. For a single electron i, it is given by:

$$n_i(\mathbf{r}) = \psi_i^*(\mathbf{r})\psi_i(\mathbf{r}), \tag{3.11}$$

where $\psi_i(\mathbf{r})$ is the single electron wave function. For systems with more than one electron, evaluation requires integration over the spacial coordinates of all other electrons. The density has to satisfy $N = \int n(\mathbf{r})d\mathbf{r}$, where N is the total number of electrons. The density $n(\mathbf{r})$ much easier to handle computationally, because it only has three variables. The Thomas-Fermi model [103, 104] is an early attempt to solve the electronic structure based on electron density alone. Unfortunately, it gives poor predictions for realistic solids because of the approximation for kinetic energy (using free electron gas), and the lack of exchange contribution.

In 1964, Kohn and Hohenberg established two theorems forming the foundation of density function theory [93]. For a system of interacting particles with hamiltonian of the

form:

$$\hat{H} = -\frac{\hbar^2}{2m_e}\sum_i \nabla_i^2 + \sum_i Vext(\mathbf{r_i}) + \frac{1}{2}\sum_{i\neq j}\frac{e^2}{|\mathbf{r}_i - \mathbf{r}_j|}, \tag{3.12}$$

the following two theorems apply:

- **Theorem I**: For any system of interacting particles in an external potential $Vext(\mathbf{r})$, the potential $Vext(\mathbf{r})$ is determined uniquely, except for a constant, by the ground state particle density $n_0(\mathbf{r})$.
- **Theorem II**: A universal functional for the energy $E[n]$ can be defined (in terms of the electron density $n(\mathbf{r})$), valid for any external potential $Vext(\mathbf{r})$. For any particular $Vext(\mathbf{r})$, the exact ground state energy of the system is the global minimum value of this function, and the density $n(\mathbf{r})$ that minimizes the functional is the exact ground state density $n_0(\mathbf{r})$.

The proof of these two theorems are not complicated and can be found in literature, e.g. [96]. They are *exact* and apply to any interacting systems. The first suggests that there is a one-to-one mapping between the ground state wave function (since the hamiltonian is uniquely determined) and the electron density. The second implies that the electron density that minimises the energy is the true ground state electron density.

These two theorems give the mathematical foundation for DFT, and show that the solution of the Schrödinger equation can be found by varying the density until a minimum of the total energy is reached. However, they only prove the existence of such universal energy functional - its exact form remains unknown.

3.1.4 The Kohn-Sham equation

One of the difficulties in applying the Honhenberg-Kohn theorems is the lack of ways to obtain the kinetic energy purely based on the electron density. This is tackled by the approach proposed by Kohn and Sham [105], which replaces the interacting many-body system with an auxiliary system of independent particles that reproduces the same electron density and energy. Therefore, the kinetic energy can be obtained using single-particle wave functions (orbitals). The hamiltonian of this auxiliary system is in the form:

$$\hat{H}^{\sigma}_{aux} = -\frac{1}{2}\nabla^2 + V^{\sigma}(\mathbf{r}), \tag{3.13}$$

where V^{σ} is some potential, and σ denotes the spin. The form of this equation is similar to Eq. (3.5). The ground state of a system is obtained by finding N^{σ} occupied orbitals $\psi^{\sigma}(\mathbf{r})$

with the lowest N^σ eigenvalues ε_i^σ. The density of this auxiliary system is obtained by summing those of the individual orbitals:

$$n(\mathbf{r}) = \sum n(\mathbf{r},\sigma) = \sum_\sigma \sum_{i=1}^{N^\sigma} |\psi_i^\sigma(\mathbf{r})|^2 , \tag{3.14}$$

since orbitals $\psi^\sigma(\mathbf{r})$ are orthonormal. The total kinetic energy of the system is:

$$T_s = -\frac{1}{2}\sum_\sigma \sum_{i=1}^{N^\sigma} \langle \psi_i^\sigma | \nabla^2 | \psi_i^\sigma \rangle . \tag{3.15}$$

The classical Coulomb interaction energy (Hartree energy) can be computed from the electron density as:

$$E_{Hartree}[n] = \frac{1}{2}\int d\mathbf{r} d\mathbf{r}' \frac{n(\mathbf{r})n(\mathbf{r}')}{|\mathbf{r}-\mathbf{r}'|} . \tag{3.16}$$

Hence, the ground state energy of this auxiliary system can be written as:

$$E_{KS} = T_s[n] + \int d\mathbf{r} V_{ext}(\mathbf{r}) n(\mathbf{r}) + E_{Hartree} + E_{II} + E_{xc}[n] , \tag{3.17}$$

where V_{ext} is the external potential, including contributions from the nuclei, and other external fields. The first four terms are well-defined by the non-interacting system. The last term E_{xc} is the exchange-correlation energy that encapsulates all many-body effects. Since the ground state energy and electron density are the same between the auxiliary and interacting systems, the exchange-correlation energy may be written in a more revealing form:

$$E_{xc}[n] = \langle \hat{T} \rangle - T_s[n] + \langle \hat{V}_{int} \rangle - E_{Hartree} , \tag{3.18}$$

where $\langle \hat{T} \rangle$ and $\langle \hat{V}_{int} \rangle$ are the kinetic and internal energy of the interacting system. The exchange-correlation energy $E_{xc}[n]$ accounts the energy difference between the interacting and non-interacting system.

Using the Honhenberg-Kohn theorems, the solution of the Kohn-Sham system can be obtained by varying the electron density Eq. (3.14) to minimise the total energy:

$$\frac{\delta E_{KS}}{\delta \psi_i^{\sigma *}(\mathbf{r})} = \frac{\delta T_s}{\delta \psi_i^{\sigma *}(\mathbf{r})} + \Big[\frac{\delta E_{ext}}{\delta n(\mathbf{r},\sigma)} + \frac{\delta E_{Hartree}}{\delta n(\mathbf{r},\sigma)} + \frac{\delta E_{xc}}{\delta n(\mathbf{r},\sigma)} \Big] \frac{n(\mathbf{r},\sigma)}{\delta \psi_i^{\sigma *}(\mathbf{r})} = 0 , \tag{3.19}$$

under the orthonormalization constraints $\langle \psi_i^\sigma | \psi_j^{\sigma'} \rangle = \delta_{i,j}\delta_{\sigma,\sigma'}$. This leads to Schrödinger-like equations:

$$(H_{KS}^\sigma - \varepsilon_i^\sigma)\psi_i^\sigma(\mathbf{r}) = 0\,, \tag{3.20}$$

where the effective hamiltonian H_{KS}^σ is given by:

$$H_{KS}^\sigma = -\frac{1}{2}\nabla^2 + V_{ext}(\mathbf{r}) + V_{Hartree} + V_{xc}^\sigma(\mathbf{r}) = -\frac{1}{2}\nabla^2 + V_{KS}\,. \tag{3.21}$$

Eq. (3.20) is known as the Kohn-Sham equation.

3.1.5 Exchange-correlation functional

The Kohn-Sham equation yields the exact solution if the exact exchange-correlation functional ($E_{xc}[n]$) is used. A reasonable guess for the form of $E_{XC}[n]$ is that it is a local or nearly local function of the electron density, written as:

$$E_{xc}[n] = \int d\mathbf{r} n(\mathbf{r})\varepsilon_{xc}([n],\mathbf{r})\,, \tag{3.22}$$

where ε_{xc} is the exchange-correlation energy density at point $\mathbf{r}$, which has a non-local dependency of the density n.

Local density approximation (LDA) The local density approximation, originally proposed by Kohn and Sham [105], approximates $E_{xc}[n]$ using the exchange-correlation energy of homogeneous electron gas. LDA removes the non-local dependency in ε_{xc} and make it a local quantity:

$$E_{xc}^{LDA}[n] = \int d\mathbf{r} n(\mathbf{r})\varepsilon_{xc}^{hom}(n(\mathbf{r}))\,. \tag{3.23}$$

The exchange part of ε_{xc}^{hom} has an analytical expression [106], and the correlation part can be computed by a high accuracy Monte Carlo method [107]. This approximation seems to be crude at the first glance, but it works very well for solids. Lattice constants of crystals are predicted to be within a few precent of the experimental values. This is because the exchange-correlation effects are rather short-ranged for typical electron densities in solids [96].

Generalised gradient approximation (GGA) It is reasonable to expect that the exchange-correction functional can be made more accurate by adding more ingredients to it. The generalised gradient approximation tries to improve on LDA by including the local density gradient:

$$E_{xc}^{GGA}[n] = \int d\mathbf{r} n(\mathbf{r})\varepsilon_{xc}^{hom}(n(\mathbf{r}))F_{xc}(n(\mathbf{r}),\nabla n(\mathbf{r}))\,, \tag{3.24}$$

where ϵ_{xc}^{hom} is the same XC energy density as in LDA, and F_{xc} is a dimensionless exchange-correlational enhancement factor, which depends on both the local density and the gradient. This allows a more accurate description of systems where density varies quickly. GGA gives better predictions of quantities such as absorption and formation energies. However, the improvements are not universal. The degrees of freedom in the functional form is increased, but it becomes difficult to satisfy all physical constraints. There are several forms of GGA functionals with different F_{xc}, and each satisfies a subset of the constraints. The Perdew-Burke-Ernzerhof (PBE) [108] functional is known to give almost identical results compared to the earlier PW91 functional [109], but has a simpler parametrization. GGA functionals are known to underbind solids, while LDA overbinds [110]. The PBEsol function [111] is designed with solid materials in mind and often gives lattice constants closer to the experimental values.

Meta-GGA and Hybrids The next step from GGA is to incorporate the second derivative of the density and/or the kinetic energy density (of independent particles). There are several proposed forms which have shown to improve binding and formation energies [112]. However, there are numerical instabilities for computational implementations that need to be addressed [113].

The other direction is to include some non-locality into the XC functional via the Hartree-Fock exchange. One of the problems in local and semi-local density functionals is that they are not self-interaction free. The Hartree-Fock exchange term cancels the self-interaction in the Hartre potential, but it lacks correlation. Thus, improvements can be made by mixing the two [114–116], giving the so called hybrid functionals. These are also known to improve the prediction of band gaps [117, 118], which are often underestimated with LDA and GGA. However, the use of hybrid functionals incurs a great increase of the computational cost, as result of the non-local exchange. In addition, some might argue that the inclusion of empirical mixing and screening parameters makes them no longer fully *ab initio*.

3.1.6 Hubbard-U correction

The self-interaction error is small for most materials where the electrons are sufficiently de-localized. However, transition metals are known to have localized d orbitals, where the uncancelled self-interactions often lead to incorrect electronic and magnetic states. One solution is to use hybrid functional, but this leads to orders of magnitude increase in computational cost (especially for plane-wave DFT).

The Hubbard-U method provides a correction by coupling the energy of the Hubbard Model with that from standard DFT [119]. The former is computed using the atomic orbital

occupations given by the Kohn-Sham wave functions. Dudarev et al. [120] proposed a simplified form, with the following expression for the total energy:

$$E_{DFT+U} = E_{DFT} + \frac{U_{eff}}{2}\sum_{\sigma}[Tr\rho^{\sigma} - Tr(\rho^{\sigma}\rho^{\sigma})], \tag{3.25}$$

where ρ_{ij}^{σ} is the occupation matrix of the atomic orbitals. This biases the orbital occupation towards having either fully occupied or unoccupied levels. Additional terms are also added to the expressions for forces and stresses. The Hubbard-U correction has little computation overhead. The value of U_{eff} is often chosen empirically, but it is also possible to calculate it from first-principles [121].

3.2 The plane-wave implementation of DFT

Materials in the macroscopic world involve large numbers of atoms and electrons, typically exceeding 10^{23}. Fortunately, most solid materials have long-ranged order,for example crystals. The infinite crystal lattice can be represented using a unit cell containing a finite number of atoms. The periodic nature of crystals makes plane waves the natural choice for expanding the Kohn-Sham wave functions, in addition to their simplicity and being computationally efficient. Other basis sets, such as Gaussian functions and atomic orbitals, are also popular choices. The plane-wave pseudopotential code CASTEP [122] is used extensively in the works presented in this thesis. This section serves as an introduction to a few the key aspects of the plane wave formulation without diving deep into the numerical and algorithmic details.

3.2.1 Plane-wave basis set

The Kohn-Sham orbitals must be discretised for it to be handled by computers. Expansion using basis functions has the advantage of being both a compact representation and allowing high accuracy. The periodic boundary condition means that $V(\mathbf{r}) = V(\mathbf{r}+\mathbf{l})$ for any potential V, where $\mathbf{l}$ consists of integer multiples of lattice vectors, i.e. $\mathbf{l} = n_1\mathbf{a}_1 + n_2\mathbf{a}_2 + n_3\mathbf{a}_3$. This leads to the Bloch theorem [123], which states that an independent-particle wave function $\phi(\mathbf{r})$ in a perfect crystal must take the form:

$$\psi(\mathbf{r})_i = e^{i\mathbf{k}\cdot\mathbf{r}}u_i(\mathbf{r}), \tag{3.26}$$

where $\mathbf{k}$ is a vector in reciprocal space that can be expressed in terms of reciprocal lattice vectors $\mathbf{b}_1, \mathbf{b}_2, \mathbf{b}_3$. The second part, $u_i(\mathbf{r})$, is a periodic function of the cell satisfying $u(\mathbf{r}) = u(\mathbf{r}+\mathbf{l})$, and can be expanded using plane waves that have wave vectors consisting of integer

multiples of the reciprocal lattice vectors:

$$u_i(\mathbf{r}) = \sum_{\mathbf{G}} c_{i,\mathbf{G}} e^{i\mathbf{G}\cdot\mathbf{r}}. \tag{3.27}$$

Thus, the wave function can be written as:

$$\psi_i(\mathbf{r}) = \sum_{\mathbf{G}} c_{i,\mathbf{G}+\mathbf{k}} e^{i(\mathbf{G}+\mathbf{k})\cdot\mathbf{r}}. \tag{3.28}$$

Substituting Eq. (3.28) into Eq. (3.20) and integrating (leaving out spin labels) gives [97]:

$$\sum_{\mathbf{G}'} \Big[\frac{\hbar}{2m}|\mathbf{G}+\mathbf{k}|\delta_{GG'} + V_{ext}(\mathbf{G}-\mathbf{G}') + V_{Hatree}(\mathbf{G}-\mathbf{G}') + V_{xc}(\mathbf{G}-\mathbf{G}')\Big] c_{i,\mathbf{G}'+\mathbf{k}} = \varepsilon_i c_{i,\mathbf{G}+\mathbf{k}}, \tag{3.29}$$

where terms in the square bracket comprise the elements of the hamiltonian matrix $H_{\mathbf{G}+\mathbf{k},\mathbf{G}'+\mathbf{k}}$. A notable advantage of using plane wave basis is that the kinetic energy term is diagonal in reciprocal space. Transformations between real and reciprocal space can be done with the Fast Fourier Transform (FFT) [124] algorithm. The Kohn-Sham orbitals and energies are obtained by solving the matrix equation (3.29). The lowest N_e Kohn-Sham orbitals are occupied, from which the electron density is obtained. The new electron density then gives the new $V_{Hartree}$ and V_{xc}. This process has to be repeated until a self-consistent solution is obtained.

The $\mathbf{k}$ vector of the wave-like part in Eq. (3.26) spans over the reciprocal space and is continuously varying. Because the reciprocal space is periodic, $\mathbf{k}$ outside the unit cell can be wrapped back. Hence, only those within the first Brillouin zone need to be considered. Formally, the total wave function is obtained by integrating $\mathbf{k}$ over the first Brillouin zone. Since the electronic wave functions are known to be smooth varying with $\mathbf{k}$, this integration can be replaced by summation over a set of discrete $\mathbf{k}$ vectors. The volume of the first Brillouin zone is inversely proportional to that of the unit cell in the real space. Therefore, the number of k-points required decreases when the cell size increases. For very large cell, a single gamma point (centre of the first Brillouin zone) may be sufficient.

A plane-wave basis set is only complete when an infinite number of $\mathbf{G}$ are included. In practice, the coefficient $c_{\mathbf{G}+\mathbf{K}}$ is expected to decrease quickly with increasing $|\mathbf{G}+\mathbf{k}|$. The basis set can be truncated using a cut-off so only those with $|\mathbf{k}+\mathbf{G}| < G_{max}$ are included. This cut-off is often expressed as an energy:

$$E_{cut} = \frac{h^2}{2m_e} G_{max}^2 \tag{3.30}$$

The size of the basis set directly affects the computational efficiency. The number of plane waves also increases with the cell size, which results in a denser grid of $\mathbf{G}$ inside the cut-off sphere. The hamiltonian matrix with a size $N_{\mathbf{G}} \times N_{\mathbf{G}}$ may not even fit into the RAM of a computer, and direct diagonalisation (which has a N^3 scaling) is impossible. Several methods has been developed to tackle the problem of solving the Kohn-Sham equations. Early methods perform molecular dynamics of a fictitious system consisting the electronic degrees of freedom [125]. Direction minimization algorithms were developed to search the minimum of the Kohn-Sham energy using a conjugate gradient method with preconditioning [97]. The density mixing approach [126] is now the default method for solving the Kohn-Sham equations in most plane-wave codes. It breaks the problem into obtaining the non self-consistent eigenfunction and eigenvalues (under fixed charge density), and the mixing of the charge densities to evolve the solution towards self-consistency. The former can be tackled by an iterative matrix diagonalisation method, which only computes the lowest N_b eigenvectors, without explicitly storing the full hamiltonian [127]. The latter is handled by algorithms that compute new charge density using the history of input and output densities [128, 129].

3.2.2 The pseudopotential approximation

The effective potentials in Eq. (3.29) can have non-vanishing Fourier components even at very high $|\mathbf{G}|$. In particular, the strong Coulomb potentials of nuclei diverge as $r \to 0$. Electron wave functions are known to be fast varying close to the nuclei and can contain nodes, increasing the cut-off energy required. On the other hand, the valence electrons are of greater importance for bond formation and chemical reactions, and have smooth varying wave functions. This can be attributed to the screening of nuclear Coulomb potential by inner electrons.

In the pseudopotential approximation, an effective potential is constructed such that the pseudised wave function and the potential itself are relatively smooth, hence fewer plane waves are need to expand them. The eigenvalues of atomic states should be identical between pseudo and all-electron calculations. The pseudo and all-electron wave functions are required to be identical outside a cut-off sphere with radius r_c. Early studies of pseudopotentials use experimental data for construction [130–132]. The first widely used *ab initio* pseudopotentials are norm-conserving [133, 134] potentials. The norm of the pseudo and all-electron wave functions are constrained to be equal within r_c. They are transferable to a range of chemical environments. The orthogonality between valence and core electrons means the potential should act differently with electrons in different angular moment channels. Such a potential

is said to be non-local and takes the general form:

$$\hat{V}_{nl} = \sum_{l,m} |Y_{lm}\rangle V_l(\mathbf{r}) \langle Y_{lm}|, \tag{3.31}$$

where Y_{lm} are the spherical harmonics and $V_l(\mathbf{r})$ is the potential for l channel. The partial waves of all-electron (dashed) and pseudised wave functions of the s, p and d channels for a norm-conserving pseudopotential generated for Ti are shown in Fig 3.1, where the pseudised wave functions are smoother and do not have nodes.

The norm-conserving requirement is lifted under the framework of ultrasoft pseudopotentials (US-PP) [135], where augmented charges are introduced for compensation. This form is more flexible and reduces the cut-off energy at a cost of increased complexity for computational implementations. Two projectors are usually used per angular momentum channel in ultrasoft pseudopotentials. Pseudo and all-electron wave functions are plotted in Fig. 3.2 for an ultrasoft pseudopotential generated for Ti. The pseudo wave functions for the d electrons are smoother than that in Fig. 3.1, as a result of the norm-conserving constraint being lifted. A closely related formulation is the projector augmented wave (PAW) method, which allows the full-electron wave function to be recovered [136, 137].

3.2.3 Convergence

One of the advantages of plane wave DFT is that the quality of the calculation can be systematically improved. The two most important parameters are the plane wave cut-off energy and the density of k-points sampling the reciprocal space. The former is closely related to the pseudopotentials used. Hard pseudopotentials require higher cut-off energies, but they are more transferable.

While under-converged parameters leads to erroneous results, overly converged settings waste computational resources and lower the overall throughput. The convergence criteria should be task-specific. For example, in structure searching it is preferable to start with relatively low cut-off energies and soft pseudopotentials, only switching to high-precision settings at a later stage.

3.2.4 Gauge-including projector augmented wave method

When a material is placed under a uniform magnetic field, induced electronic currents flow throughout the material, generating an additional non-uniform magnetic field. This allows different local environments to be resolved by nuclear magnetic resonance (NMR). For non-magnetic insulating materials, the induced current $\mathbf{j}(\mathbf{r})$ is solely produced by the orbital

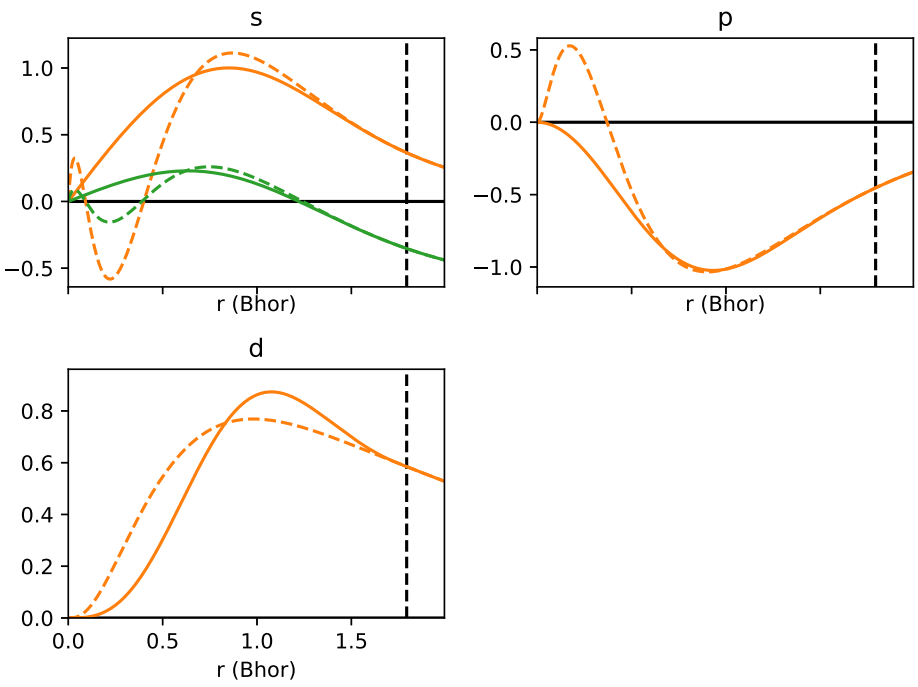

Fig. 3.1 Partial all-electron (dashed lines) and pseudo (solid lines) wave functions of a norm-conserving pseudopotential for Ti, computed using CASTEP's on-the-fly generator. The core radius is marked by the dashed vertical lines. There are two channels for s electrons (3s and 4s).

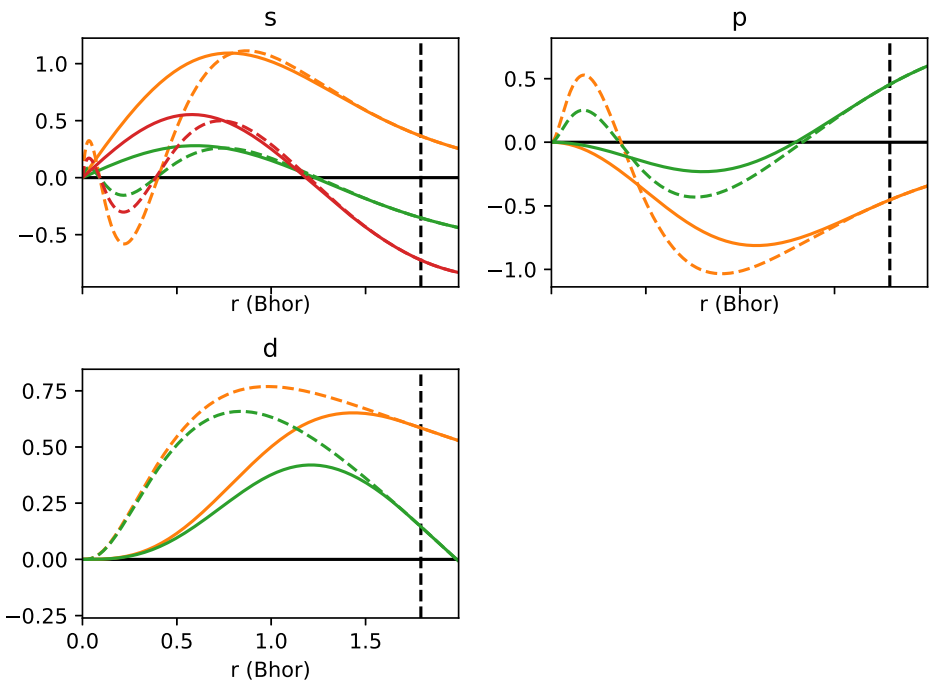

Fig. 3.2 Partial all-electron (dashed lines) and pseudo (solid lines) wave functions of an ultrasoft pseudopotential for Ti. A single projector is used for the 3s channel (orange), the other channels includes two projectors. The pseudo wave function of the d channel is smoother than that in Fig. 3.1.

motions of the electrons. The induced magnetic field is given by the Biot-Savart Law:

$$\mathbf{B}_{\text{in}}(\mathbf{r}) = \frac{\mu_0}{4\pi} \int d^3\mathbf{r}' \mathbf{j}(\mathbf{r}') \times \frac{\mathbf{r} - \mathbf{r}'}{|\mathbf{r} - \mathbf{r}'|^3} \,. \tag{3.32}$$

The shielding tensor $\sigma(\mathbf{r})$ is defined as:

$$\mathbf{B}_{\text{in}} = -\sigma(\mathbf{r})\mathbf{B}_{\text{ext}} \,, \tag{3.33}$$

which is the quantity that needs to be obtained through first-principles calculations.

The energy levels of isolated atoms are known to shift when an external magnetic field is applied, i.e., the Zeeman shift. Typical external fields only result in small contributions to the hamiltonian, hence the orbital current may be computed using the perturbation theory. To obtain the orbital current, one needs to evaluate the position operator $\mathbf{r}$, which involves some practical difficulties in extended periodic systems. Here, only give a brief summary is given, and detailed derivations can be found in Refs [138, 139]. First, places far away from $\mathbf{r} = \mathbf{0}$ give large contributions, and $\mathbf{r}$ diverges in extended systems. This problem is solved by cancelling out the two diverging terms from the paramagnetic and diamagnetic contributions. After this, the expression of the orbital current still contains the Green's function, but for an insulator it is localised. Secondly, the position operator does not have the periodicity of the unit cell. The solution is to consider the response of to a magnetic field with a finite wavelength q, and the response for a uniform field can be recovered in the limit that $q \to 0$. As a result, six extra calculations at $\mathbf{k} \pm \mathbf{q}$ are needed for each $\mathbf{k}$ point.

Both core and valence electrons contribute to the orbital current, whilst only the latter are included in the pseudopotential approach. It can be shown that the core electrons have contributions to shielding tensors that are chemically insensitive, given that the core and valence electrons are partitioned in a gauge invariant way [140]. Because NMR measures relative changes, the contributions of core electrons can be safely neglected. Another problem is that the pseudolised wave function deviates from the all-electron wave function within the cut-off sphere (Fig. 3.2), giving rise to significant errors in the computed shielding tensors. The projector augmented wave (PAW) method [136] allows the all-electron wave functions to be reconstructed from their pseudolised counterparts. However, the bare form of PAW does not fulfil the gauge invariance, which makes it not suitable for extended systems, as an infinitely large number of projectors are needed. This problem is solved by the gauge-including projector augmented wave method (GIPAW) [138] proposed by Pickard and Mauri. They introduced a modified transformation operator that ensures the translational invariance.

An extension by Yates et al. [141] allows GIPAW to be used with computationally more efficient ultrasoft pseudopotentials [135].

The NMR chemical shifts δ are measured against certain standards. In this thesis, only the isotropic part of the shielding tensor is concerned, i.e., σ is treated as a scalar. Similar to that in experiment, reference σ values can be obtained by performing calculations on the standards compounds. However, the actual standards used in experiment are often in liquid or gases states, which are not suitable for plane wave DFT calculations. In the context of solid-state NMR, the common practice is to plot the computed shielding and measured shift of a few known materials and obtain a linear fit $\delta_{\mathrm{dft}} = \alpha\sigma_{\mathrm{dft}} + \sigma_{\mathrm{dft}}^{\mathrm{ref}}$. Alternatively, a single secondary reference may be used assuming $\alpha = -1$.

3.3 Interatomic Potential based methods

Interactions between atoms can be modelled using parametrized potentials. Their forms depend on the nature of the interactions. The potential energy can be an expressed as [142]:

$$V_{total} = \sum_{i}^{N} V_1(\mathbf{r}_i) + \sum_{i,j}^{N} V_2(\mathbf{r}_i, \mathbf{r}_j) + \sum_{i,j,k}^{N} V_3(\mathbf{r}_i, \mathbf{r}_j, \mathbf{r}_k) + \dots , \tag{3.34}$$

where N is the number of atoms in the system, and V_1, V_2, V_3 are the one-body, two-body and three-body terms. In practice, V_1 is usually zero in the absence of an external field. The two-body term depends on the distance between atoms i and j ,and their identities. The three-body term is necessary when the bondings are directional, for example, to describe materials with covalent bonds.

3.3.1 The Buckingham potential

The Buckingham potential can be used to model oxides [143, 144], with pairwise contributions given by:

$$\Phi_{12} = A\exp(-Br) - \frac{C}{r^6}. \tag{3.35}$$

The first term represents the short range repulsion, which originates from the Pauli exclusion principle between closed electron shells. The second term represents the van der Waals interactions between the electron clouds, which is always attractive. The Buckingham potential differs from the Lennard-Jones potential [145] in the form of the repulsive term, which is exponential here, rather than $1/r^{12}$. The exponential term approaches a constant value when $r \to 0$. As a result, the potential becomes attractive at very short distances,

which gives rise to problems for ill-defined input structures. For ionic crystals, the Coulomb interaction is included in the expression:

$$\Phi_{12} = A\exp(-Br) - \frac{C}{r^6} + \frac{q_1 q_2}{4\pi\varepsilon_0 r}, \tag{3.36}$$

where q_1 and q_2 are the ionic charges. The Coulomb term decays with $1/r$, and is treated as long-ranged. A cut-off radius is used to truncate the short-range interactions, providing improved computational efficiency. A typical cut-off value in this work is 15 Å.

3.3.2 Molecular dynamics

Molecular dynamics (MD) simulates the "evolution" of a system with time, from which a range of physical properties can be extracted. Trajectories of each particle can be computed using the velocity verlet algorithm [146]:

$$\vec{x}(t+\Delta t) = \vec{x}(t) + \vec{v}(t)\Delta t + \frac{1}{2}\vec{a}(t)\Delta t^2$$
$$\vec{v}(t+\Delta t) = \vec{v}(t) + \frac{\vec{a}(t)+\vec{a}(t+\Delta t)}{2}\Delta t$$

The bare form of this dynamics represents an isolated system with constant energy, e.g. a microcanonical ensemble. It is often more useful to simulate a system that can exchange energy with a heat bath of constant temperature. The Nosé-Hoover thermostat couples the system with a heat bath by adding an extra degree of freedom to its the hamiltonian [147]. Barostats can be implemented similarly for constant pressure simulations.

3.3.3 Computational implementations and applicability

Calculations using interatomic potentials are orders of magnitudes faster than those of DFT. Efficient parallelisation can be achieved through spatial decomposition. Simulations of up to tens of thousands of atoms are possible, far beyond what can be treated with DFT calculations. The timescales accessible with molecular dynamics are usually in the order of nano seconds. MD simulations can also be performed using *ab inito* molecular dynamics (AIMD), but they are often limited to tens of picoseconds and relatively small cell sizes. Here, General Utility Lattice Program (GULP) [148] is used to perform geometry optimisation in interatomic potential based structure searches. GULP supports symmetry and has robust built-in local optimisation algorithms. The LAMMPS [149] code is used for MD simulations due to its speed and efficient parallelisation.

It is important to keep in mind that interatomic potentials may perform poorly in chemical environments that they are not designed for. Whilst the functional forms of such potentials are backed with physical principles, they are fitted to reproduce specific properties, such as the lattice constants. First-principles methods, on the other hand, are transferable and do not have free-parameters to adjust.

3.4 Interface Modelling

Interfaces are intrinsically non-periodic along the direction normal to the interface plane. The lateral directions are periodic but supercells are often needed to accommodate lattice mismatch and reconstructions. Modelling interfaces is challenging for two reasons. Firstly, the cell has to be sufficiently large to include both the interface and bulk regions. Embedding non-periodicity in a periodic cell incurs additional costs in the model size. For plane wave DFT calculations, which are usually cubic-scaling, this means the evaluation of energy, forces, and geometry optimisations are much more costly in terms of computational resources and wall-time. Secondly, the simulation cell has to be set up carefully. Factors such as orientation of the bulk crystal, periodicity mismatch, and terminations have to be taken into account. Unlike bulk materials, whose structures are readily available though various databases, structures of interfaces are often unknown or ambiguous in the first place. In many cases, the models have to be built by hand. A better solution is to systematically search for stable interfaces, which will be discussed in section 4.3. Nevertheless, hand-built initial models are still essential for setting up a search.

3.4.1 Lattice mismatch

In general, solid-solid interfaces can be classified into three categories:

Coherent Lattice planes from the two material are one-to-one matched at the interface, but both lattices may be strained.

Semi-coherent Misfit dislocations appears at the interface to reduce the strain energy. Lattice planes are often $N/(N+1)$ matched.

Incoherent No lattice matching takes place at the interface.

The interface energy (per unit area) increases from coherent to semi-coherent to incoherent. Fully matched interfaces often give rise to strain, since the two sides can have different lattice constants. The blue and red lattices in Fig. 3.3a have different lattice constants. They are

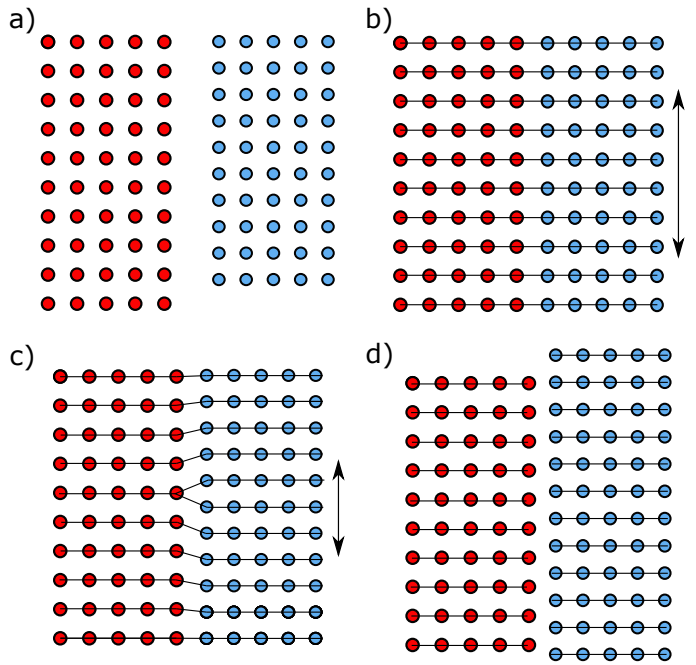

Fig. 3.3 Three possible types of interfaces formed from two crystals with mismatching lattice constants depicted in (a). These are (b) coherent, (c) semi-coherent, and (d) incoherent. Arrows indicate the sense of strain.

one-to-one matched in Fig. 3.3b, with the blue lattice being tensile strained. For ultra-thin films, the interface energy is expected to dominate, and strain up to a few percent may be maintained.

As films get thicker, it is energetically favoured to form misfit dislocations and relax the strain [150, 151], since the strain energy is proportional to the film thickness. This result in semi-coherent interfaces as shown in Fig. 3.3c. A critical thickness can be derived based on energy cost associated with interface strain and dislocations [150, 152]. Mis-fit dislocations typically nucleate at the surface and have to glide down to the interface.

The relationship between lattice parameters, matching periodicities, and residual strains can be derived for a 1D interface. Consider two 2D crystals with lattice parameters a_1 and a_2, one can write:

$$N_1 a_1 (1+s_1) = N_2 a_2 (1+s_2), \tag{3.37}$$

where N_1, N_2 are the matching periodicities, and s_1, s_2 are the residual strains. A pair of integers N_1, N_2 can be chosen to minimise s_1 and s_2. Having an array of equally spaced misfit dislocations gives $N_2 = N_1 \pm 1$. This is the case in Fig. 3.3c, for which $N_1 = 10$. In general, this happens with the lattice parameters only differ slightly, i.e. when $a_1/a_2 \approx 1$.

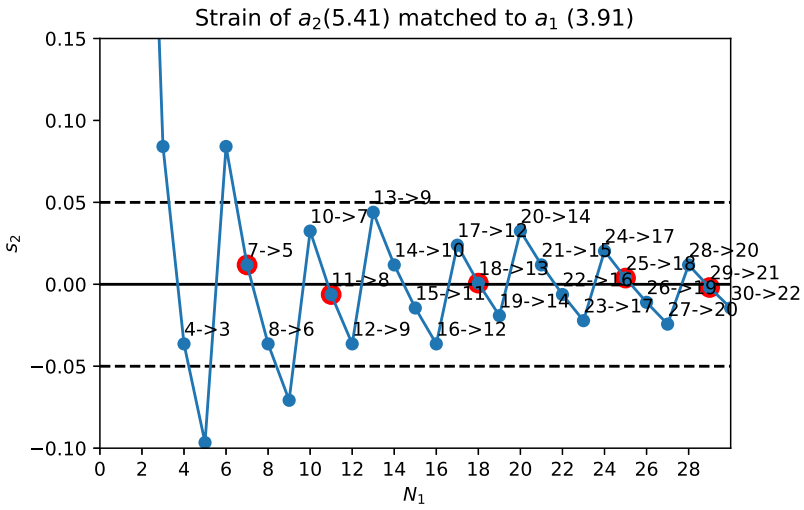

Fig. 3.4 Residual strains plotted against the periodicity N_1 when matching two crystals with $a_1 = 3.91$, $a_2 = 5.41$. The former is assumed to be rigid. Cases with small residual strains are highlighted by red circles.

When two lattices have very different structures and lattice constants, the interface can be "domain-matched", without having to satisfy $N_2 = N_1 \pm 1$. The domain matching is exploited for growing epitaxial films on substrates with very different crystal structures [153]. To illustrate this, the minimum values of s_2 for a range of N_1 are plotted in Fig. 3.4. The lattice parameters of the two sides are $a_1 = 3.91$ and $a_2 = 5.41$, and the former is made to be rigid with $s_1 = 0$. The minimum residual strain is achieved by matching 18 units of a_1 with 15 units of a_2, although schemes with small N_1 and N_2 values may take place in reality due to reduced interface energy.

Vanishingly small residual strain can be achieved by having very large N_1 and N_2, which is shown by the asymptotic behaviour in Fig. 3.4. This happens when the elastic energy dominates, or there is no way to form a low energy interface due to structural or chemical incompatibilities. The resulting interface is incoherent, but strain-free, as shown in Fig. 3.3d.

The interfaces studied in this work are mostly one-to-one matched or domain-matched, requiring relatively small supercells. Conventional semi-coherent interfaces also widely exist in thin films. Since misfit dislocations are sparsely arranged when the lattice mismatch is relatively small, very large supercells may be needed. These interfaces are often studied with interatomic potentials, and a review of this topic can be found in Ref [154].

3.4.2 Interfaces and periodic boundary conditions

Interfaces can be embedded in the periodic unit cells as slabs, as shown in Fig. 3.5a. The cell contains two surfaces in addition to the interface of interest. Slab models are commonly used for surface studies [155]. The vacuum separating the periodically repeated slabs should be sufficiently wide that the interaction between surfaces are insignificant. One way of checking is to plot the electron densities to confirm that they do not overlap. Another issue of the slab model is that the slab may have a net dipole moment. Since the electrostatic potentials must satisfy the periodic boundary condition, a fictitious electric field is added implicitly, giving errors to both the energy and forces. This can be avoided by making the slab symmetrical. Dipole corrections can be applied to asymmetrical slabs [156, 157]. In Fig. 3.5, A and B themselves may be polar in the direction perpendicular to the interface. Nevertheless, the dipole-related errors are expected to be cancelled when comparing relative energies of slabs that only differ at the centre (i.e. at the interface). On the other hand, A and B should be sufficiently thick that the interface is in an environment resembling that of the bulk.

An alternative scheme is to have two equivalent interfaces in a single unit cell. An example is shown in Fig. 3.5b, where the dotted line indicates one of the mirror planes. The other mirror plane occurs in A at the periodic boundary. The interface orientation is locked-in by the mirror symmetry, but lateral translations are free to vary during relaxation. Both A and B must already have mirror planes in their bulk phases. This construction is different from that for symmetrical grain boundary models [87, 61], since the interface is formed by two different phases.

3.4.3 Interface excess energy

The stability of interfaces can be quantified with the excess energy [61] per unit area, given by:

$$\sigma = \frac{1}{2A}(G_{total} - \sum_{i}^{n} n_i \mu_i)\,, \tag{3.38}$$

where $2A$ is the area of the two equivalent interfaces, n_i is the number of atoms of species, μ_i is chemical potential of i, G_{total} is the Gibbs free energy of the simulation cell containing the interfaces, which is approximated using the DFT total energy [87, 144]. The species are not necessarily elemental phases. For example, the excess energy of a grain boundary is usually calculated with respect to the bulk phase. Relative stability between interfaces with different stoichiometries can be compared using:

$$\Delta\sigma = \frac{1}{2A}(\Delta G_{total} - \sum_{i}^{n} (n_i - n_i^{ref})\mu_i)\,, \tag{3.39}$$

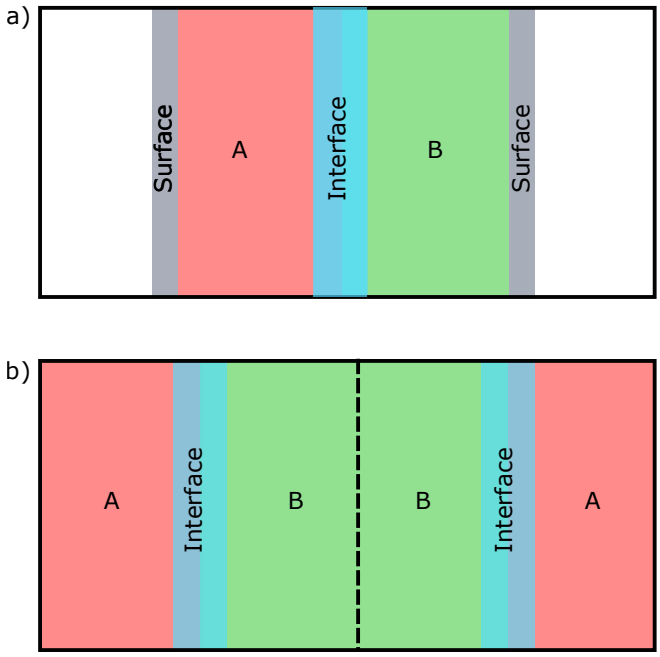

Fig. 3.5 Interfaces can be embedded in a periodic cell using a slab model (a) or a dual-interface model (b).

where n_i^{ref} is the number of species in the reference structure, and ΔG_{total} is the difference between the DFT total energies. Chemical potentials are approximated using the DFT total energy for solids, neglecting entropy contributions. For a gas phase, this can be defined with respect to a reference state μ_g^0:

$$\mu_g = \mu_g^0 + \mu_g', \tag{3.40}$$

with the reference energy μ_g^0 given by the DFT energy of an isolated molecule at 0 K. The value of μ_g' depends on the partial pressure and the temperature, and the relationship can be obtained using the NIST-JANAF thermochemical data [158].

The total energy of a slab model, shown in 3.4.2, also includes contributions from the surfaces, which need to be subtracted away:

$$\sigma = \frac{1}{A}(G_{total} - \sum_i^n n_i \mu_i) - \sigma_{sa} - \sigma_{sb} \tag{3.41}$$

Cleaving a crystal may expose two surfaces with different terminations and energies [159, 160]. As an example, cleaving the (001) plane of STO creates one surface terminated by SrO,

and the other by TiO_2. The energy of cleaving for a crystal is given by:

$$E_c = E_{slab} - E_{bulk}\,, \tag{3.42}$$

where E_{slab} is the total energy of an unrelaxed slab with two surfaces labelled as m and n. The surface energy of m is given by:

$$\sigma_m = \frac{1}{A}(\frac{1}{2}E_c + \Delta E_{relax})\,, \tag{3.43}$$

where ΔE_{relax} is the change of energy during surface relaxation.

Chapter 4

Structure prediction

4.1 Background

The knowledge of the exact atomic structure of a given material is invaluable for its theoretical description and understanding. This information is essential for computational studies since any model at the atomic level require the structure as the *a priori* input. The conventional way of obtaining this information is through experimental characterisations, which requires: (1) the material itself to have been synthesis with sufficient quantity, and (2) the existence of a method to fully resolve the structure. In many cases, these two conditions can be difficult to satisfy. An alternative approach is to search for stable structures computationally. This requires the energy of any given structure to be calculated reliably, as well as a means to systematically explore the high-dimension configuration space to locate the global minimum. The former can be fulfilled by first-principles methods, in particular, DFT calculations. Further details can be found in section 3.1 and 3.2. This chapter deals with the latter issue, and describes how it can be tackled with random structure searching.

Predicting the structure of a material without any prior knowledge is challenging. The aim is to find the global minimum of the potential energy function, which has atomic coordinates as independent variables:

$$E_t(\mathbf{r}_1, \mathbf{r}_2 ... \mathbf{r}_n) \tag{4.1}$$

where $\mathbf{r}_i$ is the vector of the ith atom. The surface formed by this multi-variable function is known as the Born-Oppenheimer potential energy surface, or in short, the potential energy surface (PES). The number of local minima on the PES can be shown to grow exponentially with the number of atoms [161]. Consider a system of N atoms, which can be divided into M sub-systems, each with N/M atoms. When these sub-systems are sufficiently large they may have independent configurations. Hence, the total number of locally stable configurations

should satisfy the equation:

$$n_s(N) = n_s^M(N/M) \tag{4.2}$$

valid solution to this, by inspection, is in the form:

$$n_s(N) = e^{\alpha N} \tag{4.3}$$

where α is a constant. This means that the global minimum is extremely hard to find reliably for large systems, since it requires locating all local minima. This make the global optimisation problem non-determinestic polynomial hard (NP-hard). However, real materials contain lots of atoms, in the order of 10^{23}, and yet most of them do exist in their stable forms, rather than being trapped in high energy polymorphs. This implies that function E_t must have certain features that one can exploit to efficiently locate the stable structure, as nature does. For example, most inorganic materials are crystalline, with stable phases described by unit cells containing a handful of atoms.

Before going into the details of *Ab initio* Random Structure Searching (AIRSS) - the structure prediction method used in this work, a brief summary is given below for other structure prediction approaches.

Simulated Annealing The simulated annealing [162] approach mimics the annealing process that promotes re-crystallisation and removal of defects in alloys. In the basic form, an existing structure is perturbed in some way. The new structure is accepted if the energy is lowered, or if $e^{-\Delta E/T} < u$ where u is a random number sampled uniformly from 0 to 1. The temperature T is gradually lowered in the search and in theory the global minimum can be reached if the cooling rate is slow enough. At high temperature, the structure is allowed to jump out from the local minima and explore the energy landscape. At $T = 0$ only structures that lower the energy are accepted, and the algorithm effectively performs a (stochastic) local minimisation. In practice, the system has a tendency to become trapped in regions surrounded high energy barriers, as escaping moves are highly likely to be rejected. There is a lot of freedom in implementing the perturbation and scheduling the cooling. Variants of the algorithm are developed to improve the performance.

Basin Hopping The simulated annealing algorithm described above does not require any knowledge of the energy gradient (i.e forces). For interatomic potentials, the gradients are often straightforward to compute, and can be used to efficiently find local minima. The basin hopping method [163] adopts a Monte-Carle plus minimisation approach. The structure is randomly perturbed and subsequently relaxed to a local minimum. The condition of

accepting the new minimum is the same as in simulated annealing. The two important parameters to adjust are the effective temperature and scheme of moving atoms. With the use of minimisation, the initial and final structure of a single step can be rather distant compared with the magnitude of the perturbation. The process can be seen as sampling a transformed PES where the energy is constant within each catchment basin. The trajectory of exploration can be used to create connectivity graphs of the minima, which are useful for studying the underlying structure of the PES. The method has been applied to small molecular systems, and its efficiency in finding global minima is further benefited by the existence of funnel-structures in energy landscapes.

Minima Hopping The transformed PES in the basin hopping method may still lead to trapping in regions surrounded by high energy minima, preventing the algorithm from escaping the funnels. A closely related algorithm is minima hopping [164], which uses molecular dynamics for escaping basins, followed by local minisation. The kinetic energy in the MD simulation is increased if escape is failed, or the new minimum has already been visited. Otherwise, it is decreased. This biases the search away from visiting existing minima and promotes visits to neighbouring basins that have small energy barriers. Deep basins tend to have lower barriers, according to the Bells-Evans-Polanyi principle [102].

Evolutionary Algorithms These algorithms are inspired by biological evolution [165]. A population of candidates are maintained and evolved towards the optimum solution by applying selection, mutation, and cross-over operations to individuals. The population is usually initialised randomly. One of the key steps for such an algorithm to be successful is to perform local optimisations on each structure before reproduction [166]. The selection operation is usually carried out by energy ranking. Mutation are applied as random displacements of atoms and lattice deformations. Cross-overs (obtaining child structures from parents) are usually achieved via cut-and-pastes of slabs, or permutations of like-species. Care is required to maintain population diversity in order to consistently improve the best solutions and to avoid premature convergence.

Particle Swarm Optimisation The particle swarm optimisation is also a population-based global optimisation method and is inspired by movements of bird flocks [167]. Each individual is affected by its own best position as well as the best global position so far. When applied to structure prediction, the population is locally minimised at each iteration [168]. Diversity is maintained by introducing a substantial amount (typically 40%) of randomly

generated structures at each iteration and eliminating similar structures.

The methods outlined above have their own strengths and weaknesses. One should be aware of the "no free lunch theorem" for global optimisation algorithms [169], which states that we are unlikely to have a magic algorithm that outperforms the rest in every case. Over-specialization for one kind of problem may lead to poor efficiency for others.

From now on, this thesis focuses on the *Ab initio* Random Structure Searching (AIRSS) method, initially proposed by Pickard and Needs for the prediction of high-pressure silane phases [170]. To avoid confusion, it is also referred as "random structure searching", because the method is not exclusively for use with first-principles calculations. Most of the approaches described above more or less already involve "random" structures, but they emphasise iterative improvements, and *learn* the PES over time. Random searching does not involve learning, and instead focuses on generating physically sensible candidate structures in the first place. This removes the iterative and state dependent nature of the process, allowing it to be fully parallelised and distributed.

4.2 Random Structure Searching

Random structure searching typically involves with the following steps:

1. Prepare the generation settings, specifying them in a seed file.
2. Generate the random structures. This usually involves choosing lattice vectors and placing atoms randomly in the unit cell. A structure is only accepted if the criteria defined in the seed files are met.
3. Relax the random structure to reach a local minimum.
4. Store the structure and repeat steps 2-3. A pool of workers is typically used to run searches in parallel, since they are independent from one another.
5. Analyse the ensemble of random structures, conduct further tests and refine. For DFT calculations, this involves ranking structures by energy, and performing relaxation using more accurate parameters on distinct low energy structures.

A schematic of this workflow is shown in Fig. 4.1. Generating a random structure usually takes a few seconds. Most computational resources and wall-time are spent on geometry optimisation, where the objective function E_t is typically evaluated hundreds of

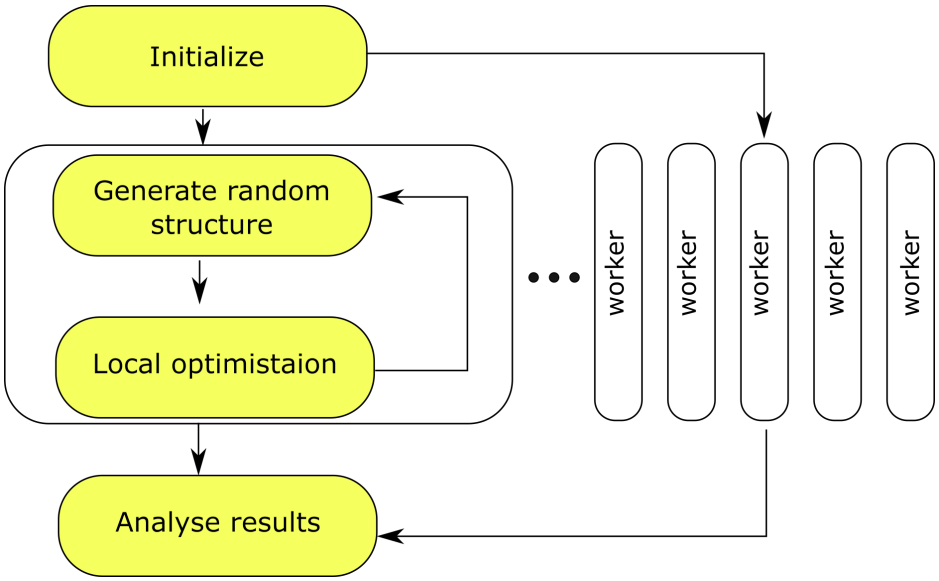

Fig. 4.1 A schematic of the random structure searching workflow. Random structures are generated and relaxed in parallel.

times. The objective function E_t should sufficiently describe the physical reality, and the prediction is only as good as the level of theory used. First-principles methods are suitable for structure prediction due to their transferability, being almost parameter-free. Plane wave DFT is preferred here because of its efficiency for small and medium-sized systems. The Hellmann–Feynman forces are computed with little cost, and can be used directly for geometry optimisation. Quality of the calculation is controlled by the cut-off energy, k-point density, and the pseudo-potentials. Looser convergence settings can be used in the initial search. Despite E_t being less precise, its general shape remains unchanged, and contains the same basin structures. A sub-set of the obtained structures, each corresponding to a distinct local minimum, can be further relaxed with high precision settings to obtain the final results.

An extensive review of the Ab inito Random Structure Searching (AIRSS) can be found in the literature [171]. The method has been applied to predictions of high-pressure bulk materials [172–174], point-defects [175], low-dimension materials [176] and interfaces [87]. In the following sections, the rationale behind its success is discussed, together with some practical aspects, and its adaptation for interface structure searching.

4.2.1 The Potential Energy Surface

Being a simple method, the success of random structure searching (AIRSS) may appear counter-intuitive. The reason is in the underlying structure of the potential energy surface (PES), which favours (or can be made to favour) even a random sampling scheme for finding

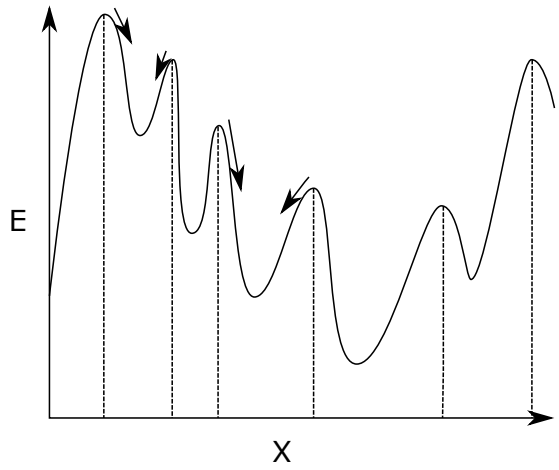

Fig. 4.2 An example of a 1D potential energy surface, divided into basins of attractions. Performing down-hill relaxations inside a given basin lead to the same local minimum. The dotted vertical lines indicate the boundaries of each basin of attraction.

the global minimum. Whilst the exact form of E_t is unknown, it is clearly not an arbitrary function, and have a number of specific properties.

The PES can be divided into many basins of attraction. Down-hill pathways starting from points with a given basin lead to the same local minimum. An one-dimensional example in Fig 4.2. When the starting point is chosen randomly, the probability of landing at a minimum is proportional to the hyper-volume of its basin of attraction. In Fig 4.2, this corresponds to length of the segments on the x axis, and the dotted vertical lines show the boundaries of each basin.

Energies of local minima may follow a Gaussian distribution in large structures, and the total number of minima grows exponentially as shown in Eq.(4.3). This works against a random sampler for finding the global minimum. However, the low energy basins are likely to have larger hyper-volumes compared with high energy basins, which is known for Lennard-Jones crystals [177]. The hyper-volume of a basin is likely to decrease with minimum energy according to a power-law [178]. Basins of different sizes are likely to be arranged with some order, with smaller basins filling the gap between larger ones.

A substantial proportion of a PES will corresponds to configurations containing unphysical small atomic separations. Here m,short-range repulsion(s) will dominate, and the PES will be high in energy, with almost no minima. The other extreme is when a large part of the unit cell contains no atoms, which leads to the formation of isolated fragments and clusters.

Such cases can be discarded if one is only interested in dense and fully connected structures. This means that one should not just randomly and independently place atoms into the unit cell.

Most periodic materials contain certain types of symmetry. This is evident by surveying the Inorganic Crystal Structure Database (ICSD), where most entries are in a space group other than $P1$ (and space group $P2_1/c$ appears to be most popular). Very low or very high energy minima are often linked with structures with symmetry.

To demonstrate the above points, densities of structures obtained from random searches of Lennard-Jones 38 clusters are plotted in Fig. 4.3. Particles are randomly placed inside a sphere with a diameter of 3.5 σ. The top plot is generated without enforcing any minimum separations (minsep) between particles. The fat tail with high energy is eliminated by making sure all atoms are separated by least 0.75 σ. In other words, the atoms are treated as hard spheres, rather than points during initialisation. The resulting distribution is shown in the central plot. Further improvements are achieved by giving initial structures 1-4 symmetry operations. The distribution becomes more broad, expanding at both high and low energies, shown in the bottom plot of Fig. 4.3. This allows the global minimum to be reliably obtained with a few hundreds trials.

In addition, the Bell–Evans–Polanyi principle means that low energy basins tend to cluster together, giving a funnel-like energy landscape. The low energy structure found with random searching may be further improved by applying random shakes followed by local optimisation. This process is effectively a one-shot zero temperature basin hopping search, and can be performed alongside the main search process.

4.2.2 Constraints, biases and stopping criteria

One commonly used constraint in random structure searching is species-wise minimum separations, which helps avoid cases contains atoms that are too close. In addition, structures that are computationally poorly described can be avoided. The cores of pseudopotentials ($r < r_c$) may overlap when atoms get too close, which leads to erroneous results or crashes of the computer programs. Interatomic potentials with strong repulsive short-range interactions may cause numerical overflow when atoms are too close. Some potentials are physically incorrect at very short range, such as the Buckingham potential described in section 3.3.1.

Values of pair-wise minimum separations can be set based on those of known phases. Of course, this biases the search towards reproducing the known phases, but unknown stable phases are also likely to have similar species-wise separations. An alternative is to start with a fixed value, say 1.5 Å, and update the setting on-the-fly by applying that from the best

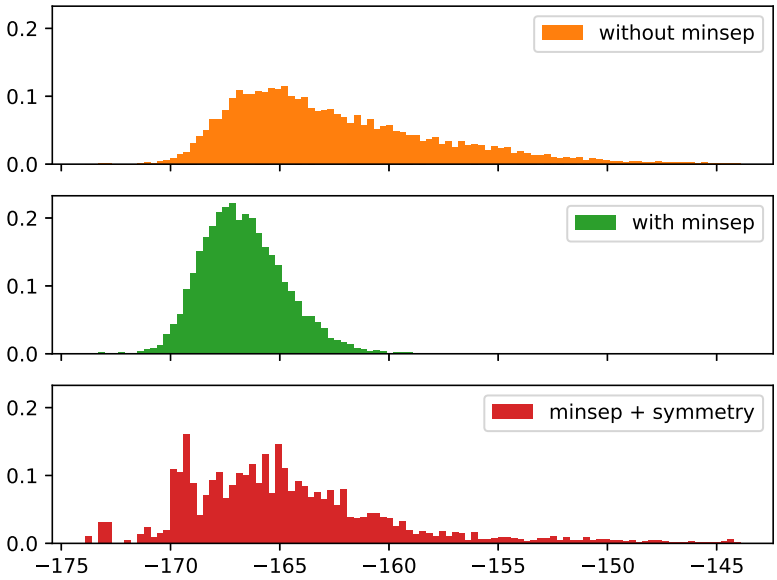

Fig. 4.3 Density of structures plots showing the energy distributions of relaxed LJ 38 clusters. Three cases are shown (from top to bottom) for the generation of initial structure: purely random, enforcing minimum separation, enforcing symmetry. *minsep*: species-wise minimum separation constraint

structures. In practice, it is found the that searches are not sensitive to the exact values used, and very often they are not fully enforced.

Including symmetry operations in random structures increases the encounter rates of low energy structures. Furthermore, it decreases the number of degrees of freedom in the system, which reduces the number geometry optimisation steps. The energy and force evaluations can be accelerated by exploiting symmetry, especially in DFT calculations. The initial symmetry should be chosen randomly and contain only a few operations, typically less than four. Structures often contain more symmetry operations after relaxation.

The search can be terminated if the PES has been sufficiently sampled. The repetitive visits of the same set of low energy minima can be used as an indicator for this. Like all global optimisation methods, there is no guarantee that has been found. On the other hand, the signal for not stopping a random search is clear - when the lowest energy structure is only encountered once or twice.

4.3 Searching for interface structures

Knowing the structures of interfaces is crucial for understanding their properties. The methods for searching stable bulk structures can be extended to interfaces. It is pioneered in the work of Schusteritsch et al. [87], which investigates high-angle symmetric grain boundaries in graphene and $SrTiO_3$. This method is further developed and tailored in this thesis for interfaces that are formed by materials with dissimilar structures and compositions.

Experimental knowledge should be used as much as possible to limit the scale of the problem. Strictly speaking, the goal of interface searching is not to find the global minimum, which may in fact be an intermixed phase, but to find low energy minima in a sub-space where the interface geometry holds. Keep in mind that epitaxial films and heterostructures are not necessarily in their most thermodynamically stable state.

4.3.1 Model construction

A bulk crystal can be divided into layers, which stack together in a particular repeating sequence. Low index interfaces can be seen as where the structure transitions from one stacking sequence to another. This is shown in Fig. 4.4, where crystal X has a $ABCABC$ stacking and crystal Y has a sequence of $A'B'A'B'$. The interface is formed by joining A and A'. Other termination combinations are also possible. The lateral alignment between the two crystals is omitted in Fig. 4.4, but should also be considered in reality.

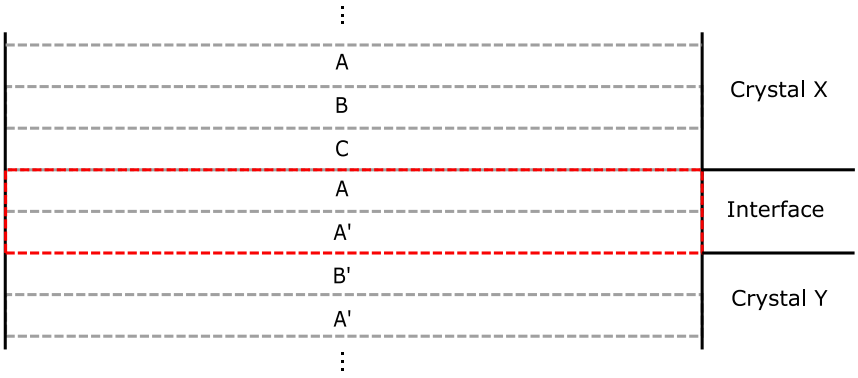

Fig. 4.4 An interface can be seen as where a transition between stacking sequences takes place.

One of the implications in the procedure above is that the bulk crystal largely remains unchanged near the interface. For most materials, it is a reasonable assumption, as any deviation from the bulk phase carries an energy penalty. Nucleation of alternative phases may also increase the elastic energy due to lattice mismatch. However, layers near the interface may not remain the same as in bulk. In Fig. 4.4, the A layer of crystal X is compatible with the C layer above, but is not necessarily compatible with the A' layer from crystal Y below it. Reconstructions are likely to take place, which cannot be obtained via simple local relaxations. It is also possible that the local stoichiometry adapts to account for the chemical mismatch of the two crystals. The bottom line is that the layer model is good until we reach the interface itself, and searches need to be performed to find the exact interface structure.

4.3.2 Limiting the search space

The degree of randomisation needs to be carefully controlled during the search for interface structures. Only atoms near the interface should be randomised. Tests should be performed to study the effects of randomisation zone size. It is found that including only the first layer on each side of the interface is often sufficient. This scheme is illustrated in Fig. 4.5. Searches with extended zone size may find the same low energy structures, but with much lower encounter rates. It is reasonable to believe that structural changes are limited to the interface region, given that there is no competing bulk phase. Different lateral alignments should also be explored, although it has been found that in some cases the randomised interface is able to driving the bulk crystals into an optimum alignment during geometry optimisations.

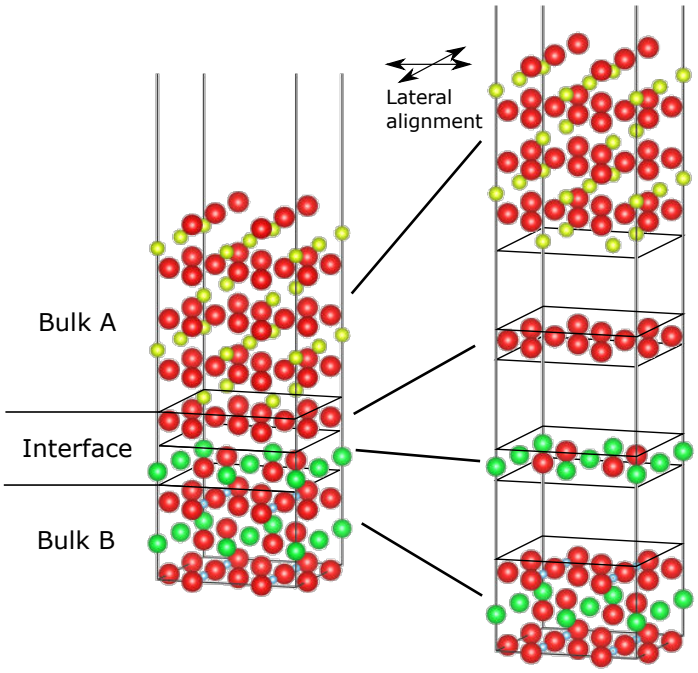

Fig. 4.5 Exploded-view of the inteface model including the randomisation zone.

Atoms within the zone are randomly displaced with species-wise minimum separation constraints. Most of the materials studied here are ionic crystals. Clusters of similarly charged ions have large electrostatic energy, but are unlikely to be re-distributed during the local optimisation. Clustering happens more often in large search cells. It is helpful to uniformly pre-distribute ions within the cell, and then apply random displacements of reduced maximum amplitudes. The amplitude of random displacements should exceed the average bond length in order to eliminate any pre-existing order.

Unless known experimentally, the search should include all possible terminations. The local compositions of the interface can be explored by adding or removing species in the randomisation zone. Relative stability between different compositions are compared with equation (3.39).

Chapter 5

Interfaces in Vertically Aligned Nanocomposites

5.1 Introduction

The knowledge of the exact atomic structure for a given material is essential for any theoretical and computational studies. Until recently, structures were almost exclusively obtained experimentally. The development of first-principles methods and structure searching algorithms has made it possible to predict stable phases of materials with a given chemical composition without any prior information [22, 171]. New materials that are not yet synthesised can be predicted, and those with ambiguity in their structures can be determined with high confidence.

Interfaces in oxide thin films are of great importance. Understanding the effects of interfaces is crucial for understanding the design principles of thin film devices. Unfortunately, interface structures can be difficult to obtain experimentally, because they are buried within the sample. Morden scanning transmission electron microscopy (STEM) has been widely used for imaging oxide thin films with atomic resolution. However, the image contrast can be highly dependent on the sample quality (primarily its thickness) and atomic numbers. Two-dimensional images only show projections along a certain crystallographic direction, which are insufficient for unambitiously determining the three-dimensional lattice. The standard routine is to infer a few candidate structures from images and optimise them to fit the data. This process involves a significant amount of human intuition, and only works reliably when the underlying structure is more or less being known already.

Vertically aligned nanocomposites adopt pillar-matrix nanostructures with a high density of vertical interfaces (see Chapter 2.3). VANs consisting of fluorite structured ionic con-

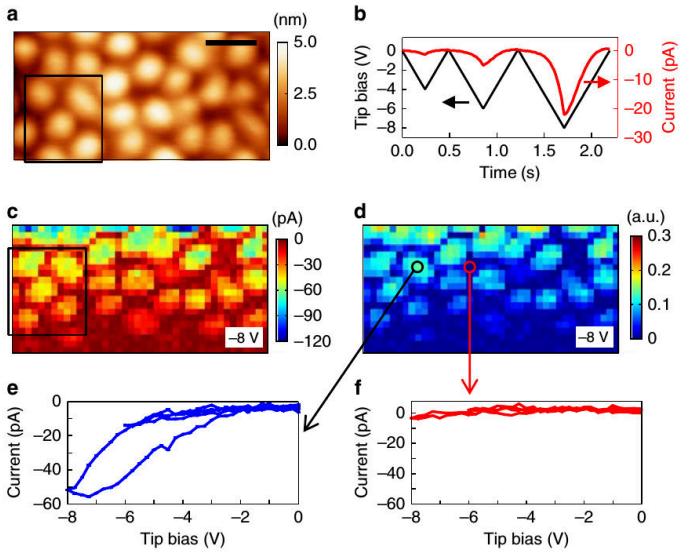

Fig. 5.1 Reported AFM data of SDC/STO VAN films [32]: (a) surface topography. (c) electrochemical strain mapping. (d) map of FORC-IV loop area. Reproduced from Ref [32] (Licensed under CC BY 4.0).

ductors have been found to give enhanced ionic conductivity [32, 33], which makes them promising solid electrolytes for micro solid oxide fuel cells. Yang et al. [32] deposited VAN films made of Sm-doped-CeO_2(SDC) pillars and $SrTiO_3$ matrix on Nb-STO (001) substrates. They found the out-of-plane ionic conductivity was increased by two orders of magnitude. To reveal the source of the enhancement, they mapped electrochemical activity using atomic force microscopy on the top surface of the film. It was found that the regions of high ionic conductivity, indicated by FORC-IV loop area, are centred on the SDC pillars, as shown in Fig. 5.1. They therefore rule out the possibility that the enhancement is due to the presence of interfaces, and suggest that the increase of ionic conductivity is instead due to better crystallinity in the SDC pillars. However, contact AFM is sensitive to the surface topography due to the finite size and the aspect ratio of the tip. The interface effects can be localised, e.g. 1-2 nm, but interface regions are unlikely to make good contact with the tip due to the surface topography. A schematic of this problem is shown in Fig. 5.2. In addition, ionic conduction is also likely to happen on the top surface of the SDC pillars, which further reduces the lateral resolution.

Assuming the pillars have square cross-sections, the volume fraction of the interface region f_i is given by:

$$f_i = 4\left(\frac{b}{a} - \frac{b^2}{a^2}\right), \tag{5.1}$$

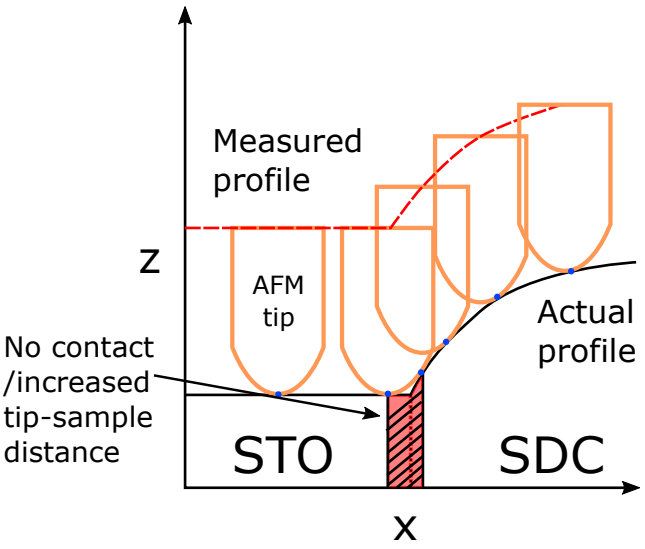

Fig. 5.2 Schematic of potential contact issues of AFM tip.

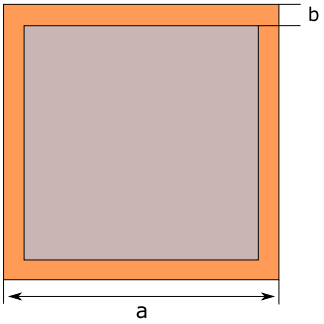

Fig. 5.3 A cross-section of a pillar with size a and interface region of thickness b.

where b is the thickness of the interface region, and a is the size of the pillar, as indicated in Fig. 5.3. The prefactor 4 is a related to the shape of the cross-section, and if the pillars are cylindrical shaped, it becomes π instead. The volume fraction of interface regions is plotted against the pillar size a in Fig. 5.4, assuming $b = 1$ nm. For a typical pillar size of 50 nm, the volume fraction is about 7%. If the enhancement is solely due to the interfaces, the local conductivity should be increased by at least three orders of magnitude. Such localised enhancement is not entirely unreasonable, because ionic conduction though vacancy hopping is thermally activated, and the activation energy is highly sensitive to atomic configuration. Thus, the structures of vertical interfaces and their roles in ionic conduction need to be thoroughly studied.

A schematic of the nanostructure of SDC/STO VANs is shown in Fig. 5.5d, which is determined using the plan-view and cross-sectional high angle annular dark-field (HAADF)

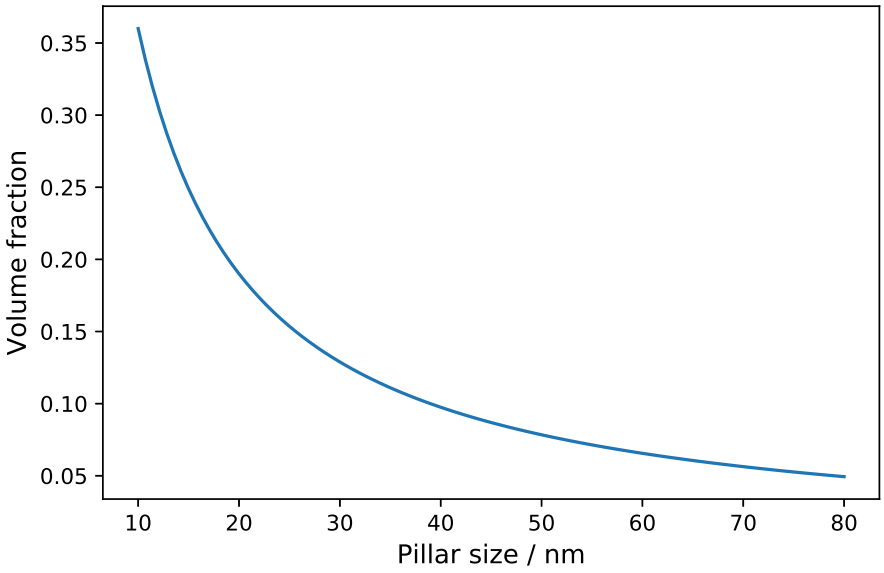

Fig. 5.4 The volume fraction of interfaces plotted against the size of the pillars. The thickness of interface regions is assumed to be 1 nm.

images captured using scanning transmission electron microscopy (STEM). These images were taken by Ping Lu. The samples were made by Seungho Cho, who previously studied the resistive switching in SDC/STO VANs [74]. The crystallographic directions between the pillar and matrix are aligned such that:

- STO[100] // SDC[110]
- STO[001] // SDC[001]
- STO[110] // SDC[110]

The SDC pillars have rounded square cross sections as shown in Fig. 5.5b. Two types of interfaces can be identified:

Type I STO(100)//SDC(110), labelled blue in Fig. 5.5b.

Type II STO(110)//SDC(100), labelled green in Fig. 5.5b.

Initially, the study focuses on the Type I interfaces, because they appear to be the most prevalent type of interfaces and have been surveyed under STEM. HAADF images show they have the STO side terminated with a plane of Ti atoms, which are indicated by the vertical lines in Fig. 5.5a&c. As a first approximation, the Sm dopants in the CeO_2 are neglected,

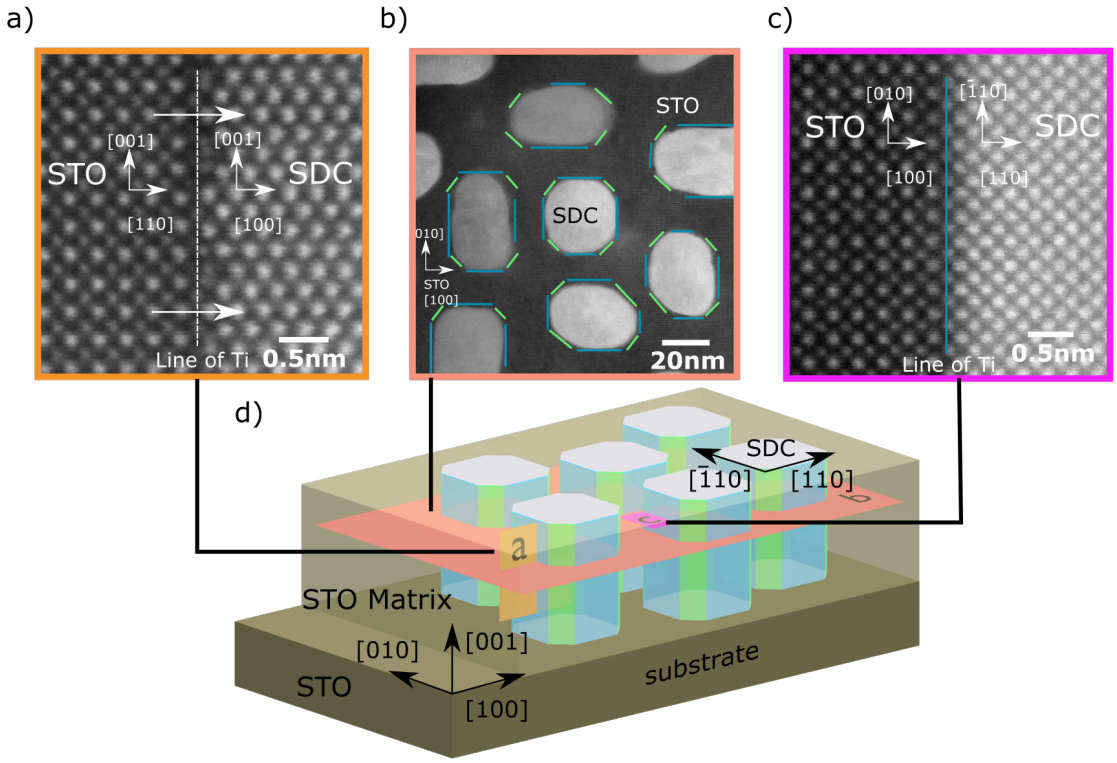

Fig. 5.5 HAADF images of SDC/STO VAN films and an illustration of the nanostructure. STEM images are taken by of Ping Lu, Sandia National Laboratory, USA.

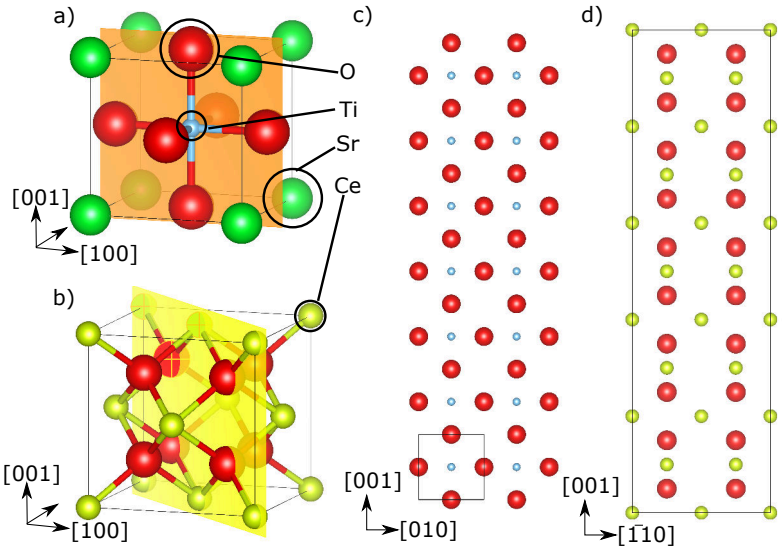

Fig. 5.6 Bulk structures of STO (a) and CeO_2(b) and the corresponding planes that forms the interface (c, d).

since they will further complicate the structure searching. Both SDC and pure CeO_2 have the same cubic fluorite structure.

The bulk structures of STO and CeO_2 are shown in Fig. 5.6a&b respectively, with the planes forming the interfaces highlighted. The lattice constant of STO is 3.905 Å and for CeO_2 it is 5.414 Å. In the vertical direction, 7 unit cells of STO (27.335 Å) match with 5 unit cells of CeO_2 (27.070 Å). The interface is domain-matched [153] (also see 3.4.1). The 7-5 matching scheme can be seen in the STEM images shown in Fig. 5.5. There is a Moiré pattern caused by overlapping lattices, since the interface may have kinks and is not completely parallel to the viewing direction. While cation positions are shown clearly in the image, there is no information available regarding the anion lattice. This is because the HAADF images are sensitive to the atomic number of atoms (approximately proportional to Z^2), hence oxygen atoms are not visible.

5.2 Methods

Seven unit cells of STO and five unit cells of CeO_2 are included along the [001] direction in the interface model. Sufficient bulk layers have to be included in the direction perpendicular to the interface, which will be discussed later. Two units cells of the bulk phases for each side are included along the STO[010] direction. Initially, attempts were made to perform first-principles searches using the slab construction, as shown in Fig. 5.7a, but soon

realised that the computational cost would be too high to obtain enough relaxed random structures to sufficiently sample the PES. Note that the generation of random structures is not computational costly. Hence, the searches are performed using interatomic potentials instead, which gives less accurate but yet good enough energies at a much lower computational cost. Buckingham potentials have been widely used for modelling bulk oxides, in spite of issues concerning their transferability [144]. They have been used to predict the structures of STO grain boundaries [61] and ZrO_2/STO ultra-thin interfaces [56]. In both cases mentioned here, the relative energies between candidate structures computed with interatomic potentials were shown to be qualitatively consistent with those computed using DFT. A similar approach is adopted here. The initial searches are performed using interatomic potentials, and a collection of the low energy structures were further relaxed with DFT. The form of the Buckingham potentials is shown in Eq. (3.35). The parameters used in this work are tabulated in Table 5.1 together with sources references from the literature.

Pair	A (eV)	B (Å)	C (eVÅ^{-6})	Reference
O-O	9547.96	0.21916	32	[56, 179, 180]
Ce-O	1809.8	0.3547	20.4	[179, 180]
Sr-O	682.172	0.3945	0	[56, 61, 144]
Ti-O	2179.122	0.30384	8.986	[56, 61, 144]

Table 5.1 Table of the parameters for the Buckingham potentials.

Details of interface structure searching is described in section 4.3. The open source AIRSS package [181] provides a suite of tools for structure prediction. The `buildcell` program provided is used to generate slab cells containing the interface. Because the interatomic potentials do not describe the base surface well*, the slab cell must be converted into the dual-interface geometry. Lattice parameters of STO are used for constructing the initial cell. The cell is fixed during geometry relaxation except in the direction perpendicular to the interface. The CeO_2 lattice is tensile strained by 2.2% along the STO [010] direction and compressed by 0.2% along the STO [001] direction. The interface strain is not expected to affect the energy landscape of the interfaces remarkably. A python package has been developed for running interface searches, which allows more flexible post-generation structural manipulations. It allows scheduler-aware automatic checkpointing and continuation; this is discussed further in Sec. 8.2.2. The stock `airss.pl` runner script included in the AIRSS package is well-suited for studying bulk materials.

Density functional theory calculations are performed using CASTEP [122]. The PBEsol [111] exchange correction functional is used, since it gives lattice constants closer to that

*In fact, the surfaces are unstable, which is not a surprise, since the potentials are fitted to the bulk phases.

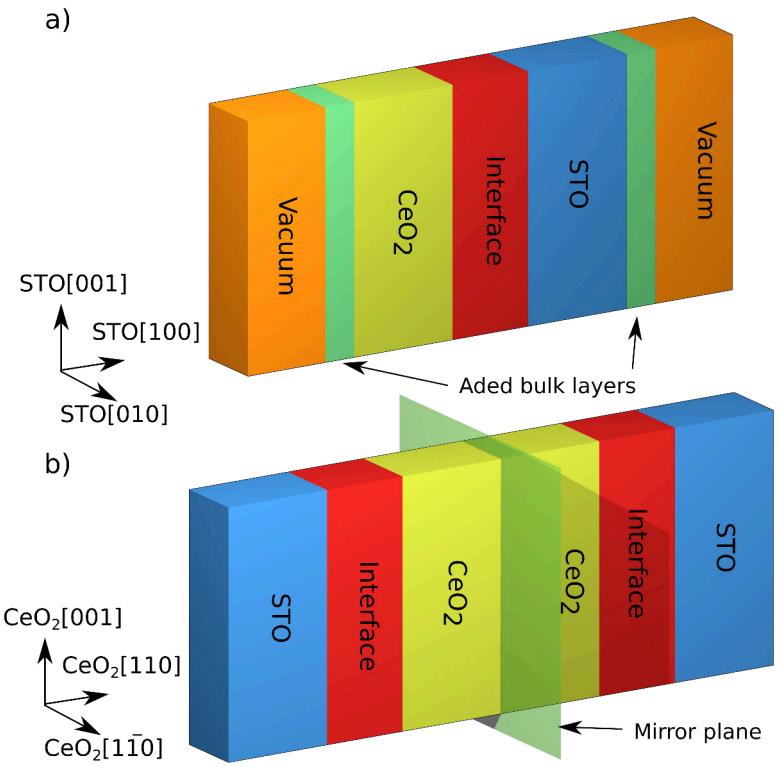

Fig. 5.7 Schematic of the search cell using slab (a) and dual-interface (b) setups.

computed using interatomic potentials for both STO and CeO_2, the interface structures obtained from the searches can be used indirectly in DFT calculations without additional scaling. Generalized gradient approximation based exchange-correlation functionals have been used in many other computational studies of STO and CeO_2 in the literature [182, 55, 183–185]. On-the-fly generated core-corrected ultrasoft pseudopotentials are used, which are generated using the `QC5` library in CASTEP version 18.1. Relevant generation strings are tabulated in table A.1. These potentials are designed to be soft and not as transferable as their harder counterparts because of the relative large cut-off sphere radius (r_c). Their usage here is justified since ionic crystals have relatively large atom-atom separations with smooth varying electron densities, and only the relative energies amongst chemically similar structures are needed in the current study. More discussion can be found in Appendix A.1. The plane wave cut-off energy is set to be 350 eV, and a $1 \times 4 \times 1$ Monkhorst-Pack grid is used for sampling the reciprocal space. The interfaces are embedded in the cell under the slab geometry. The cell vectors are fixed during relaxation.

5.3 Results

Bulk structures of both STO and CeO_2 are successfully found via random structure searching. The low energy $I4/mcm$ structure of STO is found using DFT. It is the low temperature phase observed experimentally [186]. The interatomic potentials predict the cubic perovskite $Pm\bar{3}m$ phase to be most stable, which is the room temperature phase of STO. For CeO_2, the cubic fluorite $Fm\bar{3}m$ phase is found to be most stable in both cases, which is consistent with experimental results [187].

The impact of the randomisation zone size is investigated by performing trial searches with one or two layers of atoms from the interface on each side randomised. It is found that randomising only one layer on each side is already sufficient. The larger zone size does not give any new structures that are low in energy. In fact, the same set of low energy structures are found, but each has a much lower encounter rate.

The size of the simulation cell perpendicular to the interface also needs to be converged. Multiple searches containing 4-10 layers of material are performed with about 15,000 trial structures generated and relaxed in total. A set of unique low energy structures, each being found repetitively, are identified using relative energies and structural similarity. The latter is represented using the Smooth Overlap of Atomic Positions (SOAP) descriptors [188] centred on Ce atoms that are close to the interface. Structures with different cell sizes are made comparable by inserting additional bulk layers, such that there are ten layers in total, and then relaxed again. Relative energies of nine lowest energy structures are plotted against the number of layers in Fig. 5.8. While up to ten layers are needed for converged values, all structures can be found with only 5 layers of material on each side. This suggests artificial interface-interface interactions shift the energies of the minima, but do not affect the existence of their basins of attractions. Interface searching can be performed with small cells, as long as the final energies are computed including sufficient bulk layers either side of the interface.

Five of the low-energy structures obtained though searching are shown Fig. 5.9. Only the interface regions are displayed, since there is no change of the bulk phases beyond the field of view. In practice, equivalent structures with different z-translations are found for each case, suggesting the randomised interfaces are capable of driving the bulk crystals into different alignments. A common pattern emerges among these structures - note that the faded regions in Fig. 5.9 are shared by all structures. The atomic arrangements in these regions closely resemble that of the bulk phase, even near the interface. On the other hand, in the central regions of Fig. 5.9, the anion lattices are distorted as a result of structural mismatch. Structures *A* and *B* are almost degenerate in energy and both have space group *Pc*. Structure C^* has more symmetry operations with space group *Pmm*2. In fact, it can be obtained by

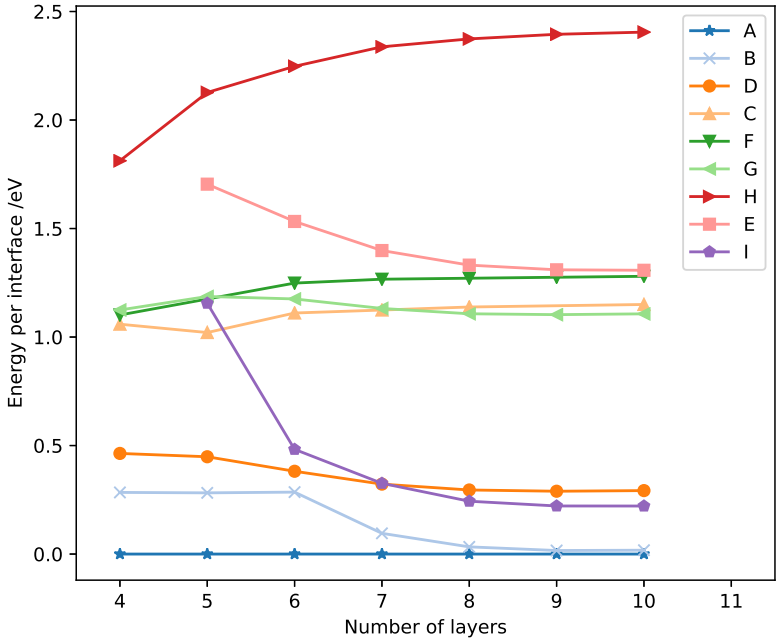

Fig. 5.8 Convergence of relative energies with the number of layers included in the cells.

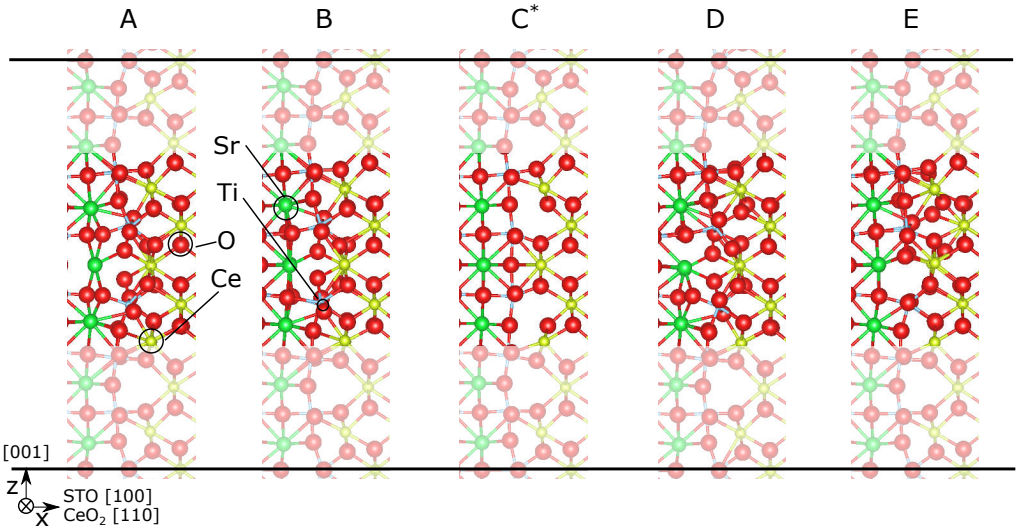

Fig. 5.9 Five lowest energy structures found for the Type I CeO_2/STO vertical interface.

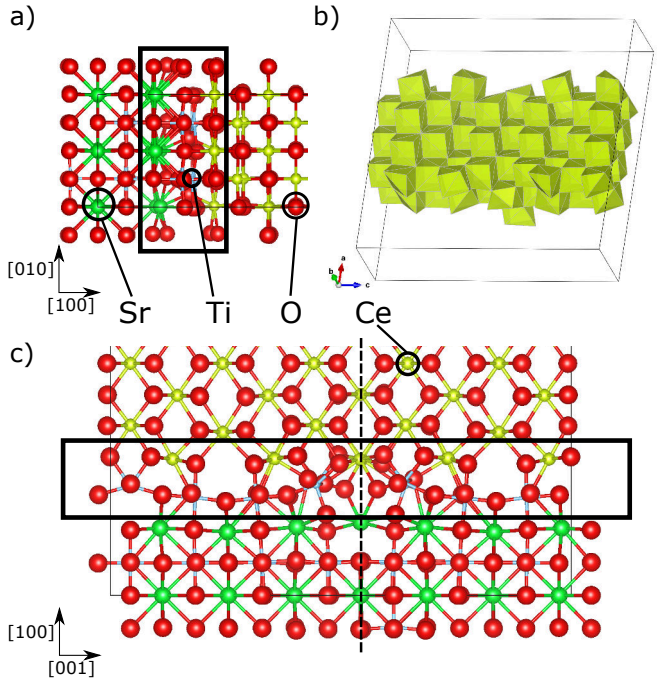

Fig. 5.10 (a) Structure *A* viewed along the *y* (STO [010]) direction. (b) Incomplete coordination cubes for Ce at the interface. (c) The glide plane in Structure *A* indicated with the dashed line.

a simple geometry optimisation using bulk crystals. Structure *D* and *E* do not have any symmetry, and the same applies for most other low energy structures.

Further details of Structure *A* are shown in Fig. 5.10. The mismatch between the two phases can be understood by considering the coordination environments. STO has six-fold coordinated Ti atoms and twelve-fold coordinated Sr atoms. The polyhedra formed by the former are corner-sharing, and those of the latter are face-sharing. Ce atoms in the fluorite structure are eight-fold coordinated by oxygen with edge-sharing cubes, as shown in Fig. 5.10b. At the interface, seven unit cells of STO meet with five unit cells of the CeO_2. The stacking sequence of STO is "TiO_2-SrO-TiO_2", while that of the CeO_2 side is "CeO_2- CeO_2'-CeO_2". Each layer is charge neutral in both materials. If the sequence is to be continued, the terminal TiO_2 layer would have 7 oxygen atoms in the next layer, extending the octahedral networks. Instead, there are 10 oxygen atoms in the CeO_2. For CeO_2, the adjacent TiO_2 layer has 14 oxygen atoms instead of 10. As a result, their anion lattices undergo reconstructions to accommodate the mismatch.

The cation lattices among these structures show little distortion from the bulk phase, which is consistent with the STEM-HAADF image displayed in Fig. 5.5a. On the other hand, the complex distortions of the anion lattice are missing in these HAADF images, since the

contrast relies on elastic scattering, which is sensitive to the nucleus charge. Annular Bright Field (ABF) images are capable of showing both light and heavy elements, and were also used to image the interfaces by our collaborator Ping Lu. Although oxygen columns can be seen in the bulk region, the contrast becomes too weak at the interface.

Density functional theory calculations are carried out to check the relative energies computed using the interatomic potentials. The test set includes nine low energy structures (*A*-*H*) as well as six structures that have higher energies (*S*1-*S*6). The dual-interface cells are converted into slab models that consist of six layers on each side to keep the cost of DFT calculations manageable. The relative interface energy densities, referenced to structure *A*, from the two levels of theory are plotted in Fig. 5.11. No significant change of the interface structure is found during DFT relaxation. In both cases, structure C^*, which can be obtained by relaxing a hand-built model, does not have the lowest energy. Structure *H* has the lowest energy when computed using DFT. A positive correlation exists over the range of energy plotted, indicated by the blue trend line. However, it is not the case over a smaller energy scale, as shown in the inset of Fig. 5.11, which is a zoom-in of the low energy end. The interatomic potentials, despite having a simple parametrised form, do capture the general trend of the energy landscape. This may be due to the ionic nature of the materials considered, whose energies and forces are reasonably well captured by the Buckingham-style potentials. The correlation over the energy scale suggests that recomputing only a subset of low energy structures using DFT is a valid strategy for refinement. On the other hand, one cannot rule out the possibility that some low energy structures only exist in the PES of DFT, hence they are missing here. Unfortunately, the cost of running fully first-principles searches for this interface geometry is prohibitively high.

The strain fields of the interface structures are obtained using the nearest neighbour Ti-Ti and Ce-Ce distances. Fig. 5.12 shows that of structure *E*. The viewing direction is along STO[010], i.e. the same as in Fig. 5.9. The triangles represent the Ti atoms, and the Ce atoms are marked by the squares. Linear interpolations are used to create the mapping. The sign of strain alternates along STO[001] direction and across the interface. The strain field can be interpreted as a result of mismatching periodicity. Two misfit dislocations may be identified by considering the continuity of the atomic planes across the interface. They are labelled in Fig. 5.12 by the red coloured $\perp$ symbol. The magnitude of strain decreases quickly when moving away from the interface. Other low energy structures are found to have strain fields similar to the one presented here.

Mobility and distributions of oxygen vacancies are affected by their relative stability at different sites. Vacancy defect energies are computed for the low energy structures using the Mott-Littleton method [189] implemented in GULP. A mapping of the relative vacancy

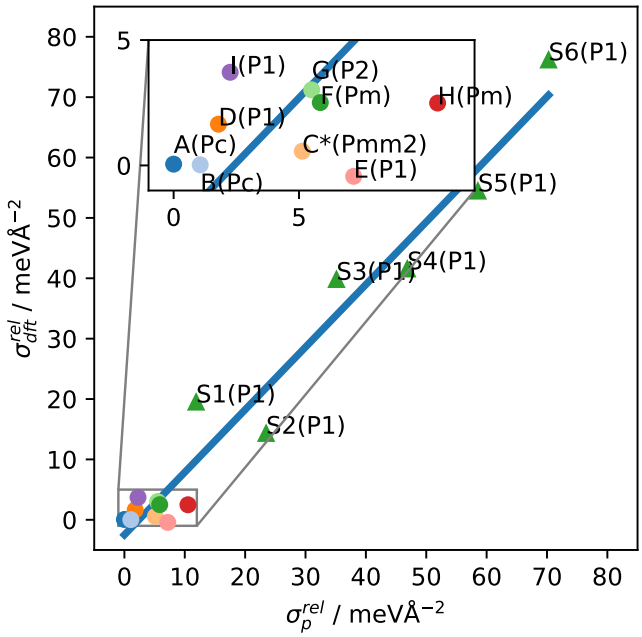

Fig. 5.11 Relative interface excess energy densities computed using interatomic potential (x axis) and DFT (y axis).

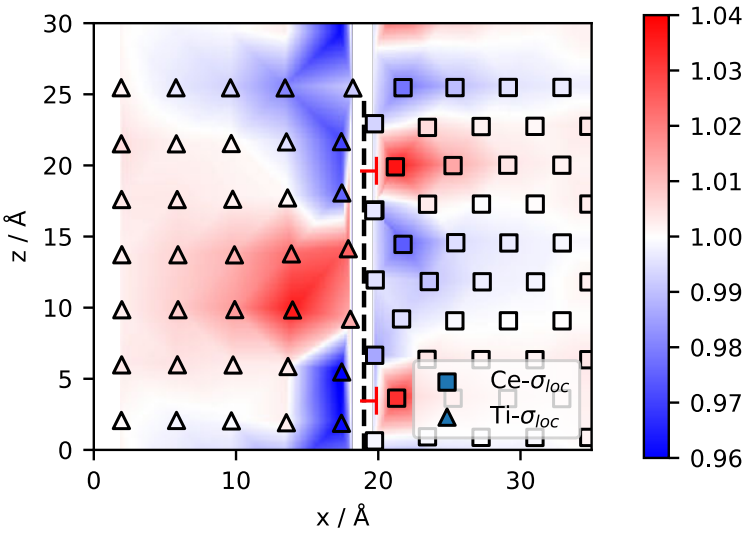

Fig. 5.12 Cation lattice strain field computed for structure E. The viewing direction is the same as that of Fig. 5.9. Triangles represent Ti atoms, and squares represent Ce atoms.

energies for structure *E* is shown in Fig. 5.13, where each circle represents an oxygen atom. All four layers of the atoms are included, and those that are further away from the viewing plane are depicted with smaller radii. The mean value of the as-computed defect energy is used as the reference. The absolute oxygen vacancy formation energy is not available using the potentials. Nevertheless, the relative values should be qualitatively representative in chemically similar environments. Sites with low vacancy energies appear in a localised region along the interface, where the oxygen lattice is highly distorted.

The existence of oxygen sites with very low vacancy formation energies, as shown in Fig. 5.13, suggests that non-stoichiometric interface structure may be stabilised. Ideally, searches should be performed with a range of interface compositions. However, atoms are modelled as particles with fixed charges by the potentials (rigid ion model). Removing or adding oxygen atoms will give the system net charges, which reduces the applicability of the potentials. Other structure prediction works using interatomic potentials all choose to limit adding/removing charge neutral units [61, 56, 84]. The point to take away here is that the uneven landscapes of vacancy energies are likely to cause trapping at the interface.

The interface excess energy of structure *E* is found to be 0.91 J/m^2, computed following the method described in Section 3.4.3. In comparison, the excess energies of STO symmetrical grain boundaries vary between 0.5 - 1.5 J/m^2 for a range of terminations and orientations [61, 87, 86]. The results here suggest that the energy costs of having these vertical interfaces are similar to that of having grain boundaries. The variation between the low energy structures is in the order of 3 meV / Å (Fig. 5.11), which corresponds to 0.05 J/m^2. At elevated temperature, many interface structures found here are energetically accessible. In reality, a disordered anion lattice may present at the interface. However, these disordered regions are likely to be separated from each other by locally ordered regions, since common motifs are shared between the predicted structures.

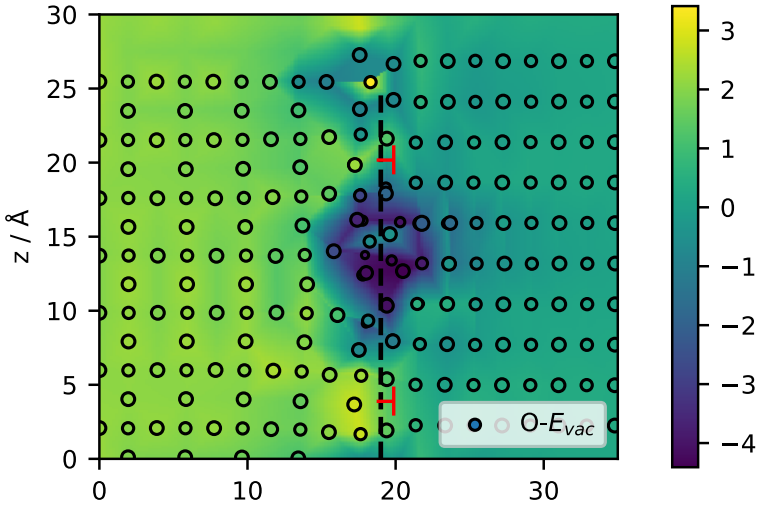

Fig. 5.13 Relative vacancy energy calculated for structure *E* using pair-potentials. The mean value is used as the reference. The viewing direction is the same as that of Fig. 5.9

5.4 Discussion

Interfaces with mismatching periodicity are often considered as containing misfit dislocations that relax the strain. For planar films, the growth process typically starts with one-to-one matched lattice, followed by the nucleation of dislocations at surfaces, which then glide down to the interface. The domain matching epitaxy is an extension to this model, where the mismatch of the lattice is so large such that the initial one-to-one matching no longer exists. Instead, the lattice is domain-matched from the start, and the misfit dislocations effectively nucleate in-place [153]. Vertical interfaces, on the other hand, grow continuously during the deposition. The vertical interface studied here can be seen as domain-matched between 7 unit cells of STO and 5 unit cells of CeO_2. Two misfit dislocations are identified as in Fig. 5.12. However, the distortions in the anion lattice do not take place at the cores of these dislocations, but in the region between them, resulting much reduced vacancy energies. The effects of dislocations on ionic diffusivity have been reported in various literatures with contrasting results [179, 190–193]. It should be noted that the dislocations are based on geometry arguments. Out results here show that the atomic structure around dislocations can be more complicated than elastic deformations in compounds with more than one element.

The possible effects of the interface structures on oxygen diffusion are discussed in the following. Ionic conductivity is expected to increase under tensile strain, as found in many other works [53, 194, 54, 72]. However, these results apply to uniformly strained bulk materials, and the strains induced by the vertical interfaces are highly localised. Diffusion of

vacancies in the out-of-plane direction have to pass through regions of alternating signs of the strain. Sun et al. [179] studied the distribution of dopants near edge dislocations in CeO_2 and found their strain fields segregate the dopants. Those with larger radii than Ce^{4+} concentrate when the lattice is tensile strained, and those with smaller radii prefer compressive strain. This can hinder the ionic conductivity, since the dopant concentration close to the interface may deviate from the optimum level. Dopants also tend to bind more strongly to the vacancy at interfaces [195].

Oxygen sites with lower vacancy defect energies than that of the bulk exist at the interface. Mobile vacancies can be trapped at these sites, because the migration barriers to the next site are very high. Dholabhai et al. [190] studied the dislocation network at the STO-MgO interface. They find sites with very low vacancy energies existing close to the misfit dislocations, as well as where they cross, giving increased barriers for oxygen diffusion. Using kinetic Monte-Carlo simulations, they show the ionic conductivity is reduced because of the trapping sites.

The energies of the candidate structures, computed using both DFT and interatomic potentials, are closely spaced. The interface is unlikely to take a single structure under finite temperature, although the structural degeneracy is limited to the anion lattice. A disordered anion lattice can lead to enhanced ionic conduction, for example, in superionic conductors [196]. However, the disordered regions are isolated from each other by regions with well-defined structures, as shown in Fig. 5.9. Hence, this effect is not expected to enhance the ionic conductivity along the out-of-plane direction.

5.5 NMR studies of vertical interfaces

A parallel project was carried out to study the vertical interfaces in CeO_2/STO VANs using solid state NMR with O^{17}. One of the challenges is that both the film and the substrate contain oxygen. Processes to obtain free-standing VAN films using exfoliation were developed by Bowen Zhang. Selective O^{17} enrichment of the free-standing film samples and NMR measurements were performed by Michael Hope. The hypothesis is that the ionic conductivity is increased at the interfaces. Hence, they can be selectively enriched with O^{17} at relatively low temperatures, under which the ionic diffusivities of bulk CeO_2 and STO are much lower.

The NMR spectrum showing shifts of O^{17} is shown in Fig. 5.14. A peak is found between those arising from STO and CeO_2. The analysis of the peak areas with increasing enrichment temperature indicates that the signal is from regions that are selectively enriched at low temperatures. I performed DFT calculations to investigate the original of this peak and whether it can be assigned to a specific interface environment. Note that the experimental

results were obtained after the computation study described in the previous sections had been completed.

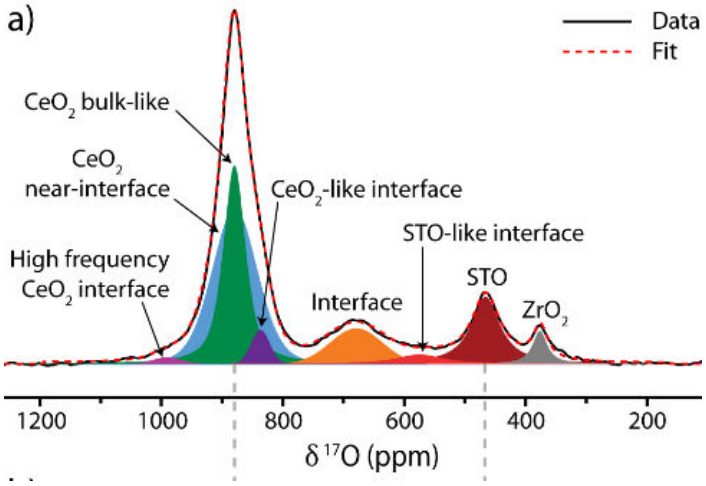

Fig. 5.14 O^{17} NMR spectrum of the VAN films with fitting peaks. Several peaks appear in between that of the $SrTiO_3$ and CeO_2. Courtesy of Michael Hope.

NMR spectra are computed using the GIPAW method [138, 141] for the interface structures found for STO(100)/CeO_2(110) vertical interfaces. Because of the large unit cell size, calculations are performed using soft pseudo-potentials (see table A.1) with a cut off energy of 350 eV to reduce the computational cost for individual structures. To check the convergence, calculations are also performed with harder potentials (see table A.3) with a cut off energy of 600 eV, and comparable interface signals are found. To check the effects of surfaces, calculations are carried out with cells containing four and eight atomic layers of each side. Although the vacuum surfaces affect the computed NMR signals, the effect does not penetrate deep into the slab. The computed shifts at the interfaces are almost identical between the thin and thick slabs, as shown in Fig. 5.15. This shows the four-layer slabs are sufficient for mimicking the bulk environment for interfaces. Thus, the four-layer configuration is used in subsequent NMR calculations for the Type I interfaces obtained previously through random searching.

The computed NMR shifts for STO(100)/CeO_2(110) vertical interfaces are shown in Fig. 5.16. The signals of oxygen atoms at the interface are either clustered near the bulk values of STO or that of CeO_2. Very few oxygen atoms, mostly from structures with slightly higher energies, have shifts consistent with the observed peak (within a range of 600 - 750 ppm). This is because these interfaces are formed by joining a TiO_2 layer with a CeO_2 layer (Fig. 5.9), both resembling that of the corresponding bulk phases. As a result, the oxygen

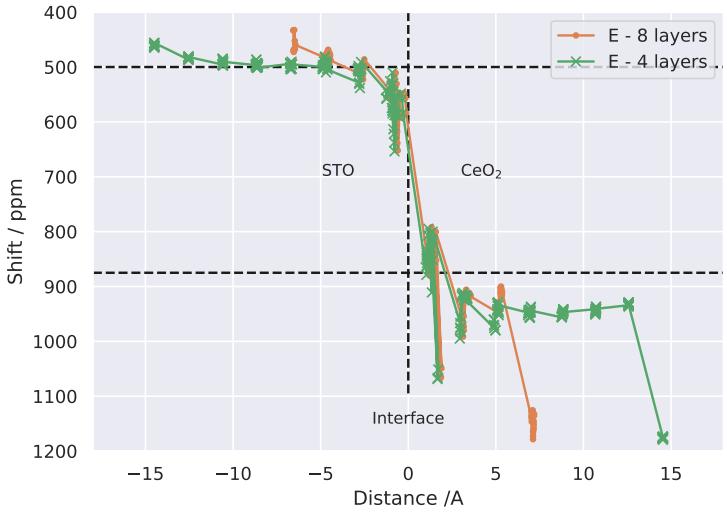

Fig. 5.15 Computed shifts with four and eight layers of materials for the structure *E* (Fig. 5.9). The interface signals are almost unaffected even if fewer layers of materials are included. Solid horizontal lines indicate the computed shifts for bulk phases.

atoms are in environments that are either CeO_2-like or STO-like. Hence, the NMR shifts computed do not significantly deviate from the bulk values.

On the other hand, not all vertical interfaces are in the Type I orientation. There are type II interfaces with interface planes being STO(110)/CeO_2(100). They are located at the corners of the pillars, as labelled by green segments in Fig. 5.5b. In contrast to Type I interfaces, both STO and CeO_2 have charged layers parallel to the interface plane. STO is made of layers with a stacking sequence "$SrTiO^{4+}$-O_2^{4-}-", and CeO_2 has layers of "Ce^{4+}-O_2^{4-}-". Because 7 unit cells of STO are matched with 5 unit cells of CeO_2 along the STO[001] direction, the O_2 layers of the two sides include different numbers of oxygen atoms. When the stacking sequence changes from one to the other, there is a choice between either having the STO's O_2 layer or CeO_2's O_2 layer at the interface. Nevertheless, the oxygen atoms at the interface are now properly sandwiched between the two bulk environments in both cases.

NMR shifts are computed using model interfaces obtained by joining slabs of bulk phases, followed by geometry optimisation. The simulation cell constructed this way has two interfaces, one has a CeO_2-like O_2 plane, and the other has a STO-like O_2 plane. In addition, structure searching is performed with the same protocol used for studying Type I interfaces. To satisfy the charge neutrality, 17 oxygen atoms are placed in the randomised interface region, which is the average between the number of oxygen atoms in the STO-like O_2 layer (14) and that of the CeO_2-like O_2 layer (20).

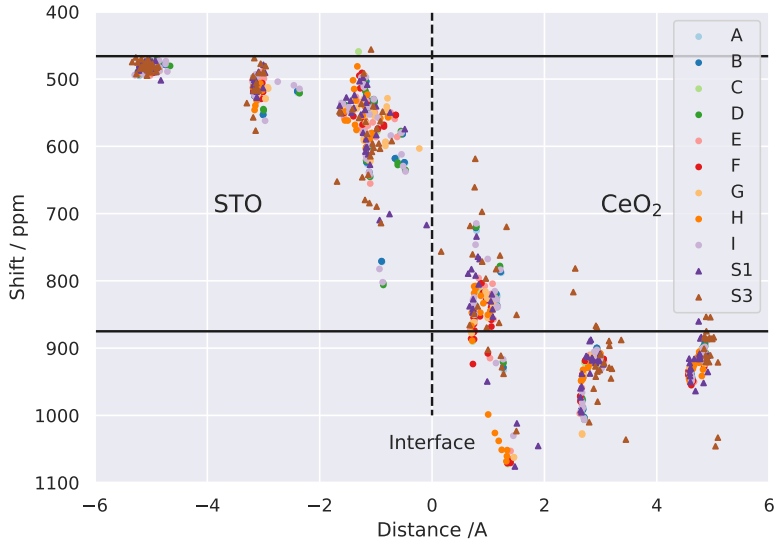

Fig. 5.16 Computed shifts using the interface models discussed in Sec. 5.3. The interface signals tend to cluster near that of bulk STO and CeO_2. Few oxygen atoms have signal in the middle.

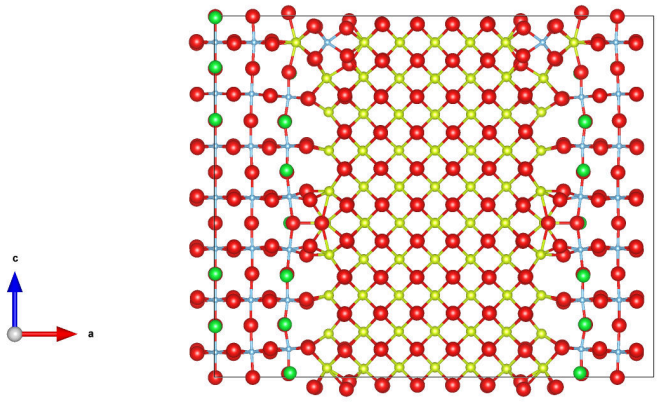

Fig. 5.17 The lowest energy interface structure of the alternative orientation obtained using random structure searching. The viewing direction is the same as that of Fig. 5.9.

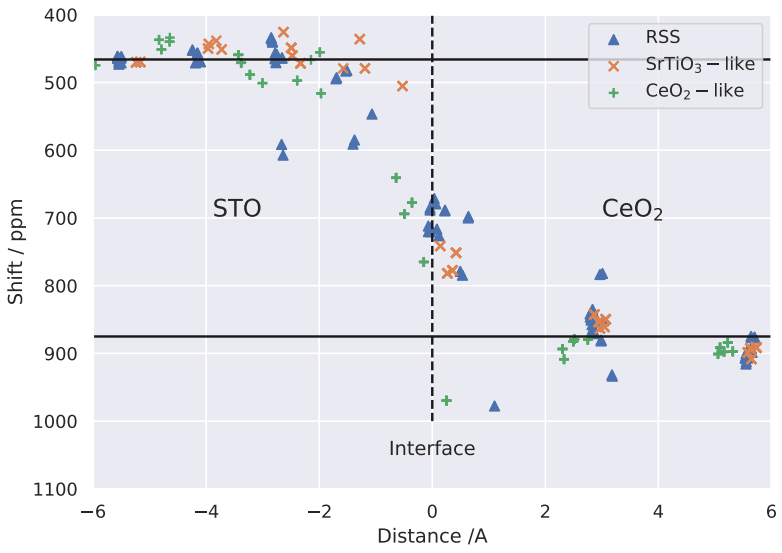

Fig. 5.18 Computed shifts of the Type II interfaces (STO(110)/CeO_2(100)) with different oxygen contents at the interface.

The computed shifts are shown in Fig. 5.18 for the three cases. Most of the oxygen atoms at the interface have shifts between 700-800 pmm, which are consistent with the measured values in Fig. 5.14. The interface structure obtained through searching has additional shifts around 600 ppm and 800 ppm, due to the intermixing of Ti and Ce atoms, shown in Fig. 5.17. Nevertheless, the computed shifts appear to be not sensitive to the exact number of oxygen atoms in the interface plane. There is no obvious choice of how many of them should be there. It is possible that this interface can accommodate a range of local oxygen stoichiometries, which may be the cause of the enhanced ionic conductivity.

5.6 Conclusion and Outlook

A collection of low energy structures for the STO(100)/CeO_2(110) interfaces are obtained using random structure searching. Previously unknown structures with lower energy than that of the hand-built interface model (C^* in Fig. 5.9) are found. The anion lattice is highly distorted near the interface. In contrast, the cation lattice remains similar to that of the bulk phases. The excess energies of these vertical interfaces, despite major structural mismatch, is similar to that of the high angle grain boundaries in STO. A complex landscape of the vacancy defect energies can be associated with the distorted lattice, which is consistent with oxygen vacancy being trapped at the interface, rather than them being more mobile. The non-uniform strain field in the cation lattice may cause dopant segregation in doped CeO_2,

which hinders oxygen diffusion. Hence, the STO(100)/CeO_2(110) interfaces are unlikely to directly enhance ionic conductivity.

On the other hand, solid-state O^{17} NMR measurements suggest there can still be enhanced ionic conduction related to the vertical interfaces. The observed NMR shifts is not consistent with that computed for the STO(100)/CeO_2(110) interfaces, but instead account for those of the STO(110)/CeO_2(100) interfaces.

Computational structure prediction is very useful for studying heterogeneous interfaces with non-trivial atomic structures. This approach can be applied to other interfaces in VANs, which are largely unexplored. Experimental studies are also important - they are essential for establishing the problem and limiting the search space to a level that is manageable. The best approach is to combine the two.

Chapter 6

Planar perovskite-fluorite interfaces

6.1 Introduction

Properties of oxide thin films can be strongly affected by the presence interfaces, and unexpected properties may emerge. An example of such an effect is was the seminal discovery of a 2D electron gas (2DEG) formed at the (001) interface between $SrTiO_3$ (STO) and $LaAlO_3$ (LAO) [6]. Despite continuing efforts in integrating these interfaces into devices [2], fundamental questions regarding the origin of the 2DEG remain open for debate [19, 16, 197, 198]. The challenge of understanding these interfaces is that they are buried inside the samples, making direct probing almost impossible.

Interfaces have long been considered a potential way of enhancing ionic conductivity, which is essential for fuel cell applications, oxygen sensors, and resistive switching memory devices. Enhanced ionic conduction was observed in CaF_2/BaF_2 supperlattice thin films [49], and attributed to overlapping space charge zones. Various studies have focused on enhancing fluorite structured oxide thin films using interfaces [199–201]. Garcia-Barriocanal et al. reported a "colossal" enhancement of ionic conductivity at the STO/yittra-stablised zirconia (YSZ) interface [11]. This work was rather controversial, and it has been suggested that the measured enhancement was from electronic conductions [30, 29, 202]. Nevertheless, it motivated theoretical studies of the possible mechanisms of the observed enhancement (see section 2.2).

Thin film epitaxial interfaces are not necessarily formed by materials of the same crystal structures. When they do, given well-matched lattice parameters, the atomic structures are often trivial to infer from that of the bulk phases. An example is the STO/LAO interface, where the ABO_3 perovskite lattice stays unchanged across the interface, and only the A and B sites are occupied by different elements. Small ionic distortions can still exist and have profound consequences on properties [13, 203, 204]. Nevertheless, the atomistic model of

the interface can be constructed easily, and the challenge is to understand the electronic structure. On the other hand, the exact atomic structure of an interface is not trivial when it is made of materials with different crystal structures. The YSZ/STO interface is an example of this; YSZ has fluorite structure and STO has a perovskite structure. Morden scanning transmission electron microscopes are capable of obtaining images resolving individual (columns of) atoms. However, these images are 2D projections of the 3D lattice, and light elements (e.g. oxygen) are often missing. Hence, the routine for determining the structure in full is to construct a few lattice models and fit them to the images. Some examples can be found in Ref [78, 79].

An alternative approach is to directly search for the interface structures using computers. Cheah et al. [56] performed pair-potential baseed searches for ZrO_2/STO ultrathin superlattices (e.g with 1.5 layers of ZrO_2) using a genetic algorithm. They found alternative phases that are very different from the bulk phase are stable at the interface, highlighting the need of performing rigorous structure searching. Dyer et al. [60] studied the YSZ/STO interface using a more realistic cell geometry, including both the interface and bulk, but they did not conduct a comprehensive search of stable interface structures. They found, by performing first-principles calculations on a few model structures created by hand, that a rock-salt ZrO termination is energetically favoured at the interface.

Because of the mismatching crystal structure, interfaces between fluorites and perovskites are likely to undergo significant reconstruction. In this work, *ab initio* random structure searching (AIRSS) is used to search for stable structures of the CeO_2 and STO (001) interfaces. CeO_2 has a cubic fluorite structure and becomes a fast ionic conductor when doped. The mismatch of lattice parameters between CeO_2 and STO is about 2%, which is much smaller than the 7% mismatch between YSZ and STO, allowing the effect of structural mismatch to be studied alone. CeO_2 films can be grown epitaxially on STO substrates [205].

This chapter describes the search and subsequent studies of CeO_2/STO(001) interfaces. The terminations at the interfaces are shown to strongly affect their structures and properties. Interfaces with SrO terminated STO sustain a fluorite anion lattice with a substantial amount of unoccupied sites, which gives rise to lateral oxygen diffusion near the interfaces. The TiO_2 terminated interface contains a buckled rock-salt CeO layer. For both cases, it is found that oxygen vacancy formation energies are lowered near the interface, which can hinder ionic transport in the perpendicular direction.

6.2 Method

General background of AIRSS and interface modelling are provided in Chapter 3 and 4. Unlike in Chapter 5, density functional theory (DFT) calculations are directly used for searching here. This is essential since a range of terminations and compositions have to be covered. No experimental data for the interface structure are used as *a priori* knowledge.

The PBEsol exchange correlation functional [111] is used in the DFT calculations. Initial searches are performed using on-the-fly generated ultrasoft pseudopotentials with relatively large cut-off radii. The parameters used for generating these potentials are tabulated in Table A.1. The plane wave cut off energy is 300 eV, and a $2 \times 2 \times 1$ Monkhorst-Pack grid is used for sampling the reciprocal space. The search cells consist of $2 \times 2 \times 2$ units of STO and $\sqrt{2} \times \sqrt{2} \times 2$ units of CeO_2. High precision calculations are performed for comparing relative stability across interfaces of different terminations and overall compositions. A cut-off energy of 600 eV is used with a set of harder pseudopotentials with $4 \times 4 \times 1$ k-point sampling. The configuration strings of these potentials are shown in Table A.3. Simulation cells containing slabs of STO and CeO_2 are transformed into the dual-interface models for these calculations (see Fig. 3.5). The generation strings for the pseudopotentials are displayed in Table A.3.

Molecular dynamics (MD) simulations are performed using the LAMMPS code under constant pressure (NPT ensemble) to obtain the equilibrium cell sizes, followed by constant volume simulations (NVT ensemble). The Buckingham potentials with long range Coulomb interactions are used (as in Chapter 5), and their parameters can be found in table 5.1. A time step of 2 fs is used in all MD simulations. Transition states barriers for a range of paths are computed using both DFT and interatomic potentials, to check the applicability of the latter at interfaces. The LST/QST method [206] for transition state searching is used by the DFT calculations, as implemented in CASTEP [122]. The climbing-image nudged elastic band [207] method, as implemented in ASE [208], is used with the interatomic potential calculations.

6.3 Bulk phases and terminations

The bulk phases of STO and CeO_2 have cubic symmetry. At room temperature, STO has a cubic perovskite ($Pm\bar{3}m$) structure with lattice constant 3.905 Å, whilst CeO_2 has a fluorite structure with lattice constant 5.41 Å. Epitaxial films of CeO_2 can grow on an STO(001) substrate, orientated such that CeO_2[110] is parallel to STO[100] and CeO_2[001] is parallel to STO[001], as shown in Fig. 6.1. The pseudocubic lattice constant for CeO_2 is 3.82 Å,

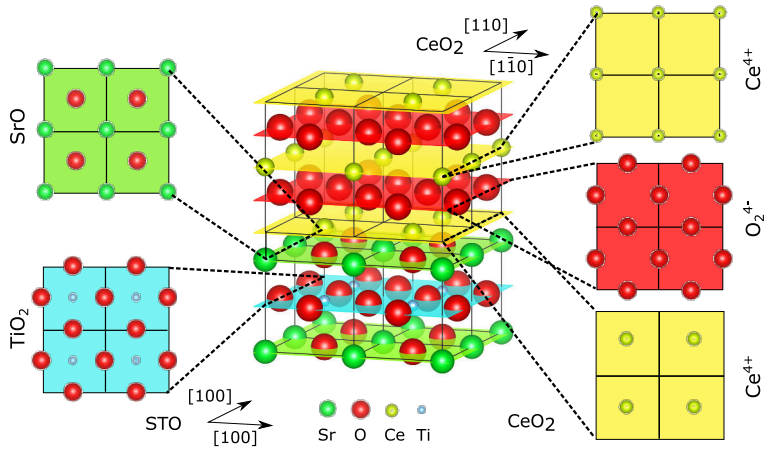

Fig. 6.1 Interface model constructed by stacking layers of STO and CeO_2 along their [001] directions. Top views of individual layers are also included.

resulting in a tensile strained of 2.2% when fully matched to the STO substrate. At low temperatures, STO has an anti-ferrodistortive ground state (space group $I4/mcm$) [209], which can be located through AIRSS. Because the energy difference is very small, the cubic phase is used for constructing the interface model.

A simple interface model can be constructed by stacking (001) planes of STO and CeO_2, as shown in Fig. 6.1. While the lattice parameters are well-matched, their stacking sequences are rather different. CeO_2 consists of alternating Ce and O_2 planes along the [001] direction, with the the sequence: $Ce_a^{4+} - O_2^{4-} - Ce_b^{4+} - O_2^{4-}$. Adjacent Ce planes are displaced laterally by $(\frac{1}{2}, \frac{1}{2})$ pseudocubic unit cells. STO is made of alternating SrO and TiO_2 planes along the [001] direction. The (001) layers in CeO_2 are charged, while those in STO are charge neutral. The two structures also share some common patterns. The cation sites are displaced by $(\frac{1}{2}, \frac{1}{2})$ cubic unit cells between adjacent layers in STO, similarly to CeO_2. The anion lattice of the TiO_2 layer has an arrangement that is similar to the O_2 layer in CeO_2.

Model interface structures can be constructed by enumerating all possible terminations, including "TiO_2-Ce", "TiO_2-O_2", "SrO-Ce", and "SrO-O_2". In addition, the two sides may have different lateral alignments, including displacements by $(\frac{1}{2}, \frac{1}{2})$, $(\frac{1}{2}, 0)$, $(0, 0)$ unit cells. Hence, there are 12 different combinations in total. While some of them happen to be the most stable structure for the given composition, structures with significant reconstructions cannot be obtained this way. Furthermore, the model structures do not fully sample the composition space, and the local stoichiometry at the interfaces can differ from the bulk.

6.4 Interface structures

Interface searches are performed for TiO_2 and SrO_2 terminated STO. These two cases are treated separately since the substrate termination can be controlled in experiment [202]. The interface excess energy density is given by:

$$\sigma = \frac{1}{2A}(G_{total} - \sum_{i}^{n} n_i \mu_i)\,. \tag{6.1}$$

If only the oxygen content is varied, the relative excess energy density can be written as:

$$\Delta\sigma = \frac{1}{2A}(\Delta G_{total} - n_O \mu_o)\,, \tag{6.2}$$

where n_O is the number difference of oxygen atoms with respect to a reference composition, μ_O is the chemical potential, and ΔG_{total} is the difference in Gibbs energy. Since the entropic contributions are expected to be similar among the solid phases, G_{total} is replaced by the internal energy obtained from the DFT calculations. The reference composition is chosen to be made of integer units of CeO_2, TiO_2 and SrO. The value of n_O is varied between -4 to $+4$. The lower limit is equivalent to letting the CeO_2 terminate with a Ce layer, and the upper limit corresponds to the CeO_2 terminating with a O_2 layer.

Search results for SrO terminated interfaces are shown in Fig. 6.2. The SrO-Ce terminated interface in Fig. 6.2a does not contain significant reconstruction. The lateral alignment of the two lattices minimises the electrostatic energy. Oxygen atoms in the SrO plane lie directly beneath Ce atoms, and the Sr atoms move downwards as a result of Coulomb repulsion, giving a slightly buckled SrO layer. The arrangement of each layer is almost identical to those in the bulk phase. In fact, this structure can also be obtained by relaxing the hand-built model SrO-Ce interface. However, the same is not true for the SrO-O_2 terminated interfaces, where oxygen dimers are formed, as shown in Fig. 6.2b. These dimers have bond lengths between 1.45 Å and 1.50 Å, which is consistent with the peroxide O_2^{2-} group. Similar structures arise as defects that compete with oxygen interstitials in CdO [210], ZnO [211] and Al_2O_3 [212], where they are referred as oxygen dumbbells. Three peroxide groups are located in the SrO plane, with one in the CeO_2 plane. The formation of "O_2^{2-}" reduces the net ionic charges, and thereby decreases the degree of polar discontinuity at the interface.

Alternatively, the net ionic charge at the interface layers can be reduced by having fewer oxygen atoms. The lowest energy structure with SrO-O termination is shown in Fig. 6.2c. A partially occupied oxygen sublattice emerges at the interface, where empty sites are represented as hollow red circles. Notably, the side view in Fig. 6.2c closely resembles the bulk phase, indicating that the fluorite and perovskite orderings are still intact. The

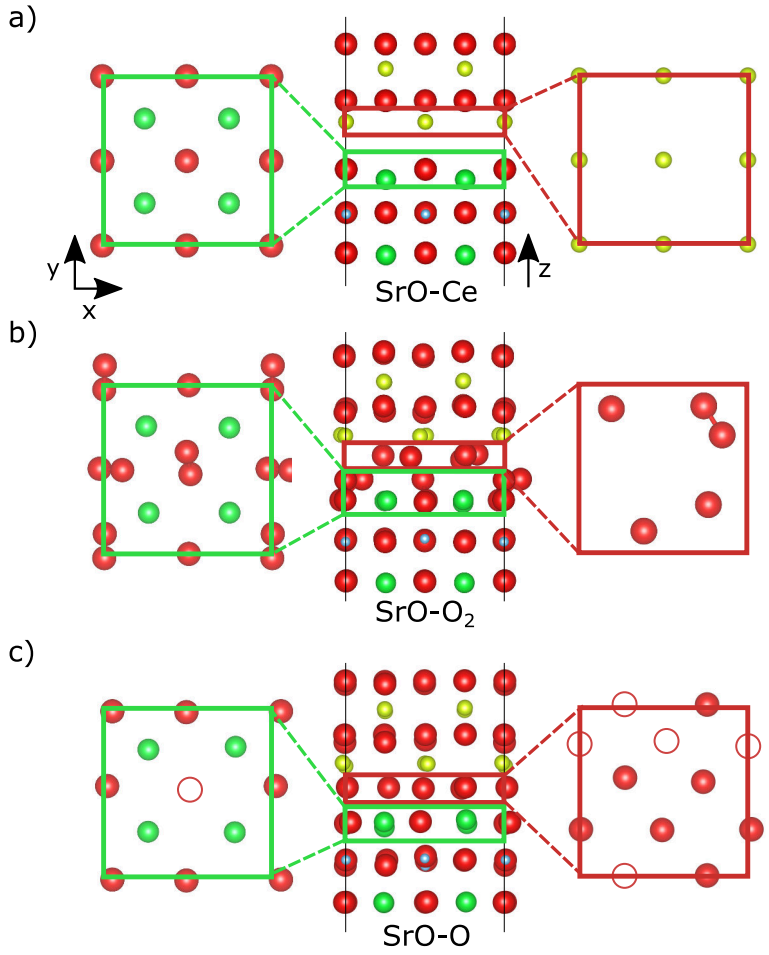

Fig. 6.2 Lowest energy structures found with a) SrO-Ce, b) SrO-O_2 and c) SrO-O terminations.

implications of these unoccupied sites will be discussed later. Apart from small deviations, the cation lattices are almost indistinguishable among the three cases shown in Fig. 6.2.

Structures of TiO_2 terminated interfaces are shown in Fig. 6.3. Similar to the SrO-Ce case, the lowest energy structure found with the TiO_2-Ce termination can be obtained by relaxation of the model structure. There is a slight buckling in the TiO_2 layer where Ti atoms moves downwards, as shown in Fig. 6.3b. The oxygen lattice in this layer resembles that in CeO_2, resulting a good match. The TiO_2-O_2 interface also contains the same number of peroxide groups as in the SrO-O_2 case. The structure appears to be more reconstructed as shown in Fig. 6.3b. This can be attributed to Ti^{4+} having ionic radius than Sr^{2+}. There are several polymorphs of bulk TiO_2. In contrast, SrO has a single stable phase with a rock salt structure.

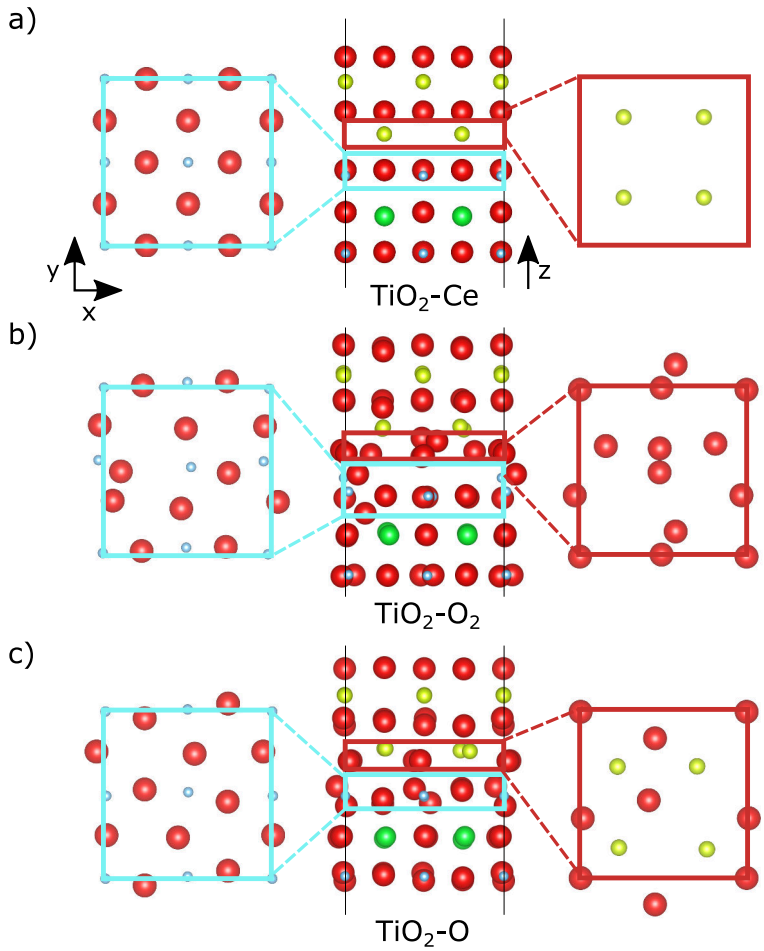

Fig. 6.3 Lowest energy structures found with a) TiO_2-Ce, b) TiO_2-O_2, c) and TiO_2-O terminations.

The stable TiO_2-O interface structure is displayed in Fig. 6.3c. Unlike the SrO-O interface, a buckled rock salt structured CeO layer emerges at the interface. The buckling can be explained by the smaller ionic radius of Ce^{4+} which is insufficient for supporting the rock salt structure. The lateral displacements of the oxygen atoms also induces rotations of TiO_6 octahedra in STO.

The 2×2 supercell size in the lateral directions may constrain the interface from further reconstructions. Shake-and-relax optimisations are performed using expanded cells containing $2\sqrt{2} \times 2\sqrt{2}$ pseudocubic units. The stable structures obtained for Sr-O_2, Ti-O_2 and Sr-O interfaces are tested. Atoms close to the interfaces are randomised with a maximum amplitude of 1 Å, followed by relaxation. New structures with lower energy should emerge if reconstruction was prevented by periodic boundaries previously. In practice, only structures with higher energies are found, and no new structure with lower energies is obtained.

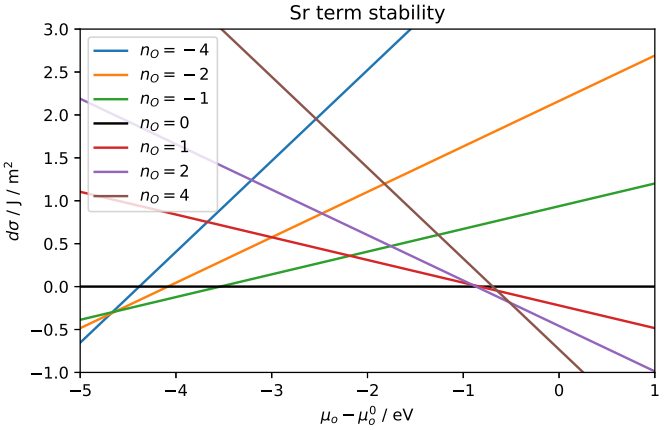

Fig. 6.4 Relative interface excess energy density plotted against $\mu_O - \mu_o^0$ for SrO terminated interfaces.

The relative interface excess energy density $\Delta\sigma$ is plotted against $\mu'_O = \mu_O - \mu_O^0$, for SrO and TiO_2 interfaces obtained via searches, in Figs. 6.4 and 6.5, respectively. In addition to $n_O = -4, 0, 4$, interface structures with other n_O values are also included. The higher the value of μ'_O, the more oxygen rich the environment is. The $n_O = -4$ interfaces are stable in oxygen poor environments. Similarly, those with $n_O = +4$ are stable in oxygen rich environments. At the intermediate range, interfaces with $n_O = 0$ are stable, represented by the black horizontal line.

The reference chemical potential μ_O^0 is obtained by computing the DFT total energy of a spin polarised oxygen molecule. However, semi-local exchange correlation functionals are known to over bind molecular oxygen, and hence a correction is needed. This is obtained by computing the DFT formation energy of a smaller number of alkali and alkaline metal

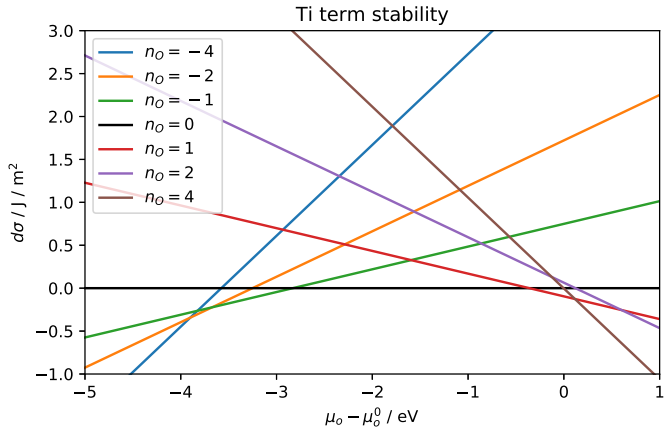

Fig. 6.5 Relative interface excess energy density plotted against $\mu_O - \mu_O^0$ for TiO_2 terminated interfaces.

oxides, and fitting to the experimental values [213, 158]. A value of 1.18 eV is obtained here for the PBEsol functional, as shown in Fig. 6.6.

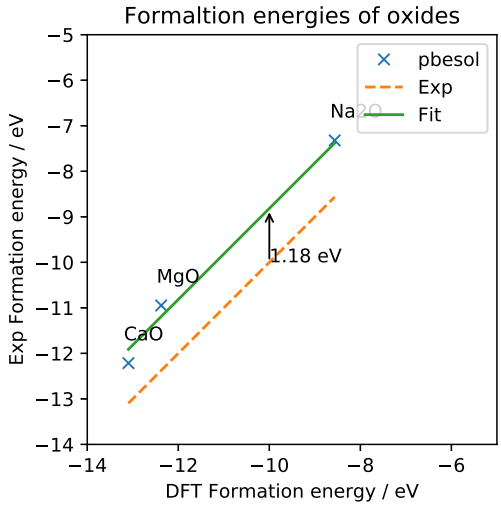

Fig. 6.6 The correction to account the overbinding of molecular oxygen is obtained by fitting DFT and experimental formation energies for Na_2O, MgO and CaO.

The value of μ'_O is a function of both temperature and pressure, and phase diagrams are calculated for the SrO and TiO_2 interface using the data from the NIST-JANAF thermodynamics table [158]. These are shown in Figs. 6.7 and 6.8, respectively. In both cases, the "X-O" type terminations with reconstructed structures are most stable under the film growth conditions, which typically have temperatures ranging from between 800 K to 1000 K, with oxygen partial pressures between 10 Pa and 10^{-8} Pa [205, 32, 74].

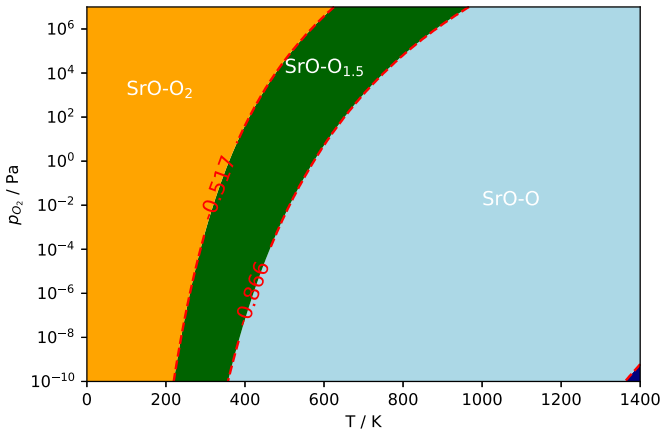

Fig. 6.7 A phase diagram calculated for SrO terminated interfaces. Films are typically grown with temperatures between 800 K and 1000 K, and pressures between 10 Pa and 10^{-8} Pa, which are well within the stable region for the SrO-O interface (Fig. 6.2c).

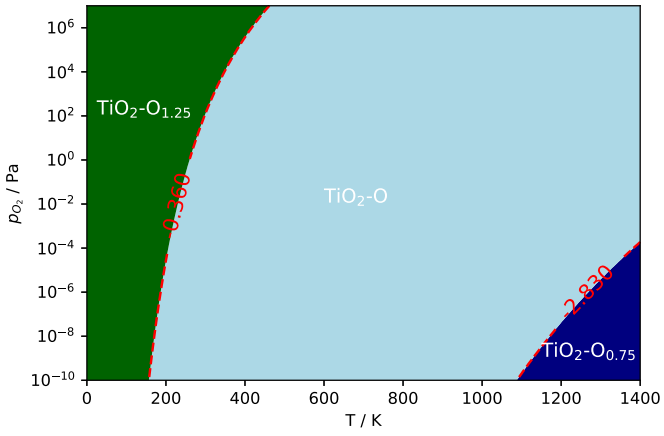

Fig. 6.8 A phase diagram calculated for TiO_2 terminated interfaces. The TiO_2-O termination (Fig. 6.3c) is most stable under typical growth conditions.

Compositional changes at interfaces have been suggested to be crucial for providing stabilisation. Dyer et al. [60] studied the YSZ/STO interfaces using hand-built models, with a range of terminations. They found that a rock salt structured ZrO termination ($n_O = 0$) is stable with respect to having O_2 ($n_O = 4$) and Zr ($n_O = -4$) terminations. The results presented here, obtained using structure searching with any *a priori* model, qualitatively agree with Ref [60] in the most part. A small difference is that the Ti-$O_{1.25}$ and SrO-O_2 structures are most stable at $\mu'_O = 0$. This may be a result of the energy correction for molecular oxygen - it is not clear whether Dyer et al. included this term in their calculations. Cheah et al. [56] searched for ultrathin ZrO_2/STO superlattices using a genetic algorithm. Due to the use of interatomic potentials, only charge neutral compositions could be added or removed, limiting exploration of the composition spaces. They also show that strain is a significant contributor to stabilising novel phases at the interface. The cubic fluorite phase of ZrO_2 is not stable under the 7% bi-axial tensile strain [59, 55, 56]. The 2% strain here is unlikely to stabilise new phases for CeO_2. This is also checked by conducting AIRSS searches CeO_2 under up to 7%, and no new stable phases are found.

6.5 Vacancies at the interface

The diffusion of oxygen ions in CeO_2 relies on having mobile vacancies. The interface can affect the distribution of intrinsic defects. Vacancy formation energies are computed at various sites in the SrO-O (Fig. 6.2c) and TiO_2-O (Fig. 6.3c) interfaces. The lowest value of each layer is plotted in Fig. 6.9. The interface is labelled by the dotted vertical line.

Vacancy formation energies are reduced from the bulk value 3.6 eV to 3.2 eV at the SrO-O interface. This reduction is more prominent for the TiO_2-O interface, where the CeO layer has a formation energy of only 2.3 eV. The TiO_2 layer appears to have sites with the same energy, as shown in Fig. 6.9, but this is because the vacancy migrates to the CeO layer during relaxation. The same also happens to the vacancy created in the TiO_2 layer at the SrO-O interface. It should be noted that these values of formation energy are not fully converged with respect to the cell size, especially in the lateral directions, since only 2×2 pseudo-cubic cells are included. Artificial vacancy-vacancy interactions affect the computed formation energy. Nevertheless, their trend should be correct, since systematic errors are cancelled when comparing relative energies.

Interfaces and grain boundaries are known as sinks for defects. Several computational works have studied the effect of interfaces, but have so far been limited to those between identical structure types [195], or based on hand-built models [190, 214]. Dholabhai et al. [214] studied the CeO_2/STO interface using interatomic potentials and found the vacancy energy to

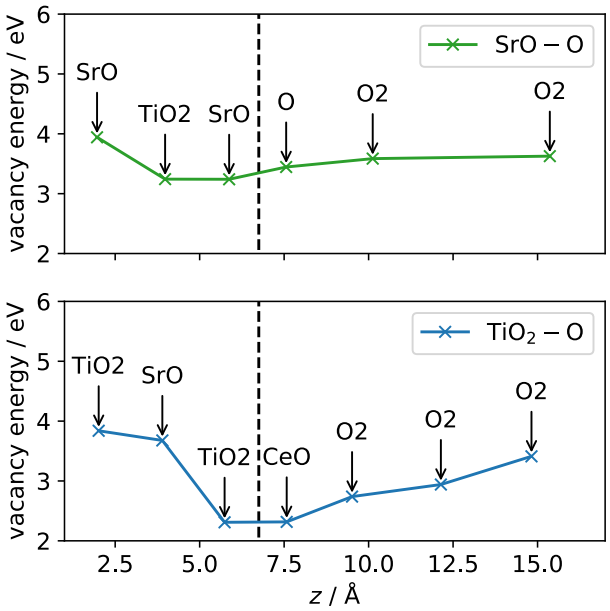

Fig. 6.9 A plot showing the vacancy formation energies of each layer in SrO-O and TiO_2-O interface models. In both cases, vacancies are more stable at the interface.

decrease near the interface on the CeO_2 side. This is also observed here. However, Ref [214] reports an increase in the vacancy energy for the TiO_2 terminated interface. The inconsistency may be attributed to their assumption that the CeO_2 side terminates with a O layer similar to that found for the (001) surface of UO_2 [215], which is very different to the structures obtained by searching here. Also, their values are computed using interatomic potentials that are not as transferable for interface environments. The large reduction of the vacancy formation energy at the TiO_2-O inteface can be attributed to the CeO rock salt layer being less stable compared with the bulk phase. These results show the STO-CeO_2 interface attracts oxygen vacancies, which leads to increased concentration close to the interface. Hence, the ionic conduction in the perpendicular direction is likely to be hindered, since vacancies need to escape from the energetically favoured sites close to the interface. This also leads to the formation of space charge zones next the interface.

6.6 Ionic conduction at interfaces

The stable SrO-O interface has many unoccupied oxygen sites at the interface, depicted by the empty red circles in Fig. 6.2c. These vacancies are, strictly speaking, not point defects, but are a part of the atomic structure. Doping CeO_2 with trivalent elements such as Sm or

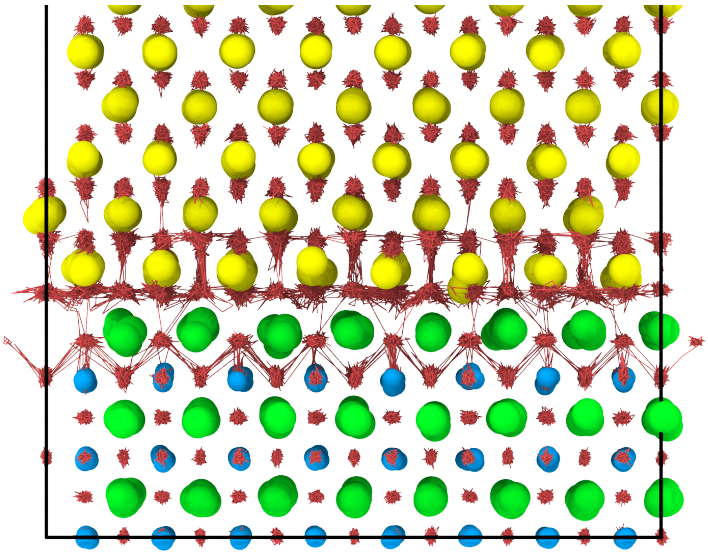

Fig. 6.10 Trajectories (red lines) of oxygen ions over 500 ps in an NVT simulation at 1600 K. The view direction is along STO[010].

Gd is known to enhance the ionic conductivity by creating charge compensation vacancies, thereby increasing the charge carrier concentration. In analogy, at the SrO-O interface, one may consider these vacancies as being induced by Sr^{2+}, although these are confined to the interface. The same does not happen at the TiO_2 interface where the Ti^{4+} ions have the same valence charge as Ce^{4+}. Instead, a buckled rock salt layer is formed to bridge the two sides.

The unoccupied oxygen sites can potentially enhance ionic conduction. Molecular dynamics simulations are performed to investigate ion diffusion at the interface, using the SrO-O structure (Fig. 6.2) as the initial geometry. The trajectories of oxygen ions over a period 500 ps at 1600 K is shown in Fig. 6.10. The oxygen atoms at the interface are clearly mobile, despite there being no explicitly introduced vacancies. The diffusion is confined to within two layers from the interface either side. In contrast, simulations performed for the TiO_2-O interface show no anion diffusion. No cation diffusion is observed in either cases.

Simulations are performed at a range of temperatures, which allows the activation energy to be computed based on the mean square displacements (MSDs) of the anions. The latter is averaged from a range of time origins for a given MD simulation. The results are plotted in Fig. 6.11. The activation energies are found to be $E_a = 1.04$ eV and $E_a = 0.63$ eV for the high and low temperature regimes respectively. This can be related to different environments at STO and CeO_2 side, as the diffusion in the STO side is less active at low temperatures. The temperatures of the MD simulations are much higher than the those in experiment, since vacancy hopping events are rare, and require very long sampling times to obtain trajectories

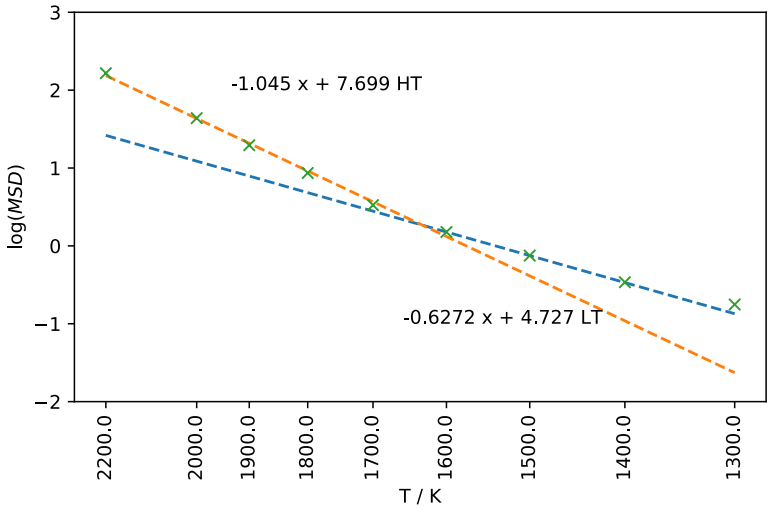

Fig. 6.11 The Arrhenius plot of the mean square displacement (MSD) of the oxygen anions for fitting the activation energies. There are two regimes with $E_a = 1.04$ eV at high temperatures and $E_a = 0.63$ eV at low temperatures.

with statistical significance. Hopping events are much more frequent at high temperatures, allowing the results to be gathered with fewer time steps. This approach is widely used in the literature [200, 59, 57, 179]. The activation energy 0.63 eV is consistent with the reported values of doped CeO_2, which ranges from 0.4 eV to 0.6 eV [216, 217]. The hop of an oxygen ion from one site to the next involves squeezing though a gap between two cations. The radius of Sr^{2+} ions is 132 pm whereas that of Ce^{4+} ions is 101 pm [218]. In addition, oxygen anions in the SrO layer may contribute to the increase of barrier heights. Hence, vacancies are less able to hop around at the interface. Furthermore, their movements may be correlated due to their high concentration. The diffusivity D can be computed from MSD via the equation $MSD = 6Dt$. The oxygen diffusivity is estimated to be in the order of 1×10^{-10}cm s^{-1} at 1000 K, which is similar to that of the pure CeO_2 [216].

To check the transferability of the interatomic potential, transition state energies are computed for a range of paths using both the potentials and DFT. The forward barrier heights obtained by both methods are shown in Fig. 6.12, and the corresponding paths are illustrated in Fig. 6.13, showing only the anion lattice. The large square shows the $\sqrt{2} \times 2\sqrt{2}$ supercell use in calculation. The interatomic potential are found to consistently over-predict the barrier height by up to 1 eV. Thus, the oxygen diffusivity is likely to be underestimated in the MD simulations. The barrier heights also span a range of around 1 eV, which can be related to the vacancy-vacancy interactions, since the interface has a very high effective concentration. It should be noted that the searches are performed under 0 K and are limited to small supercells.

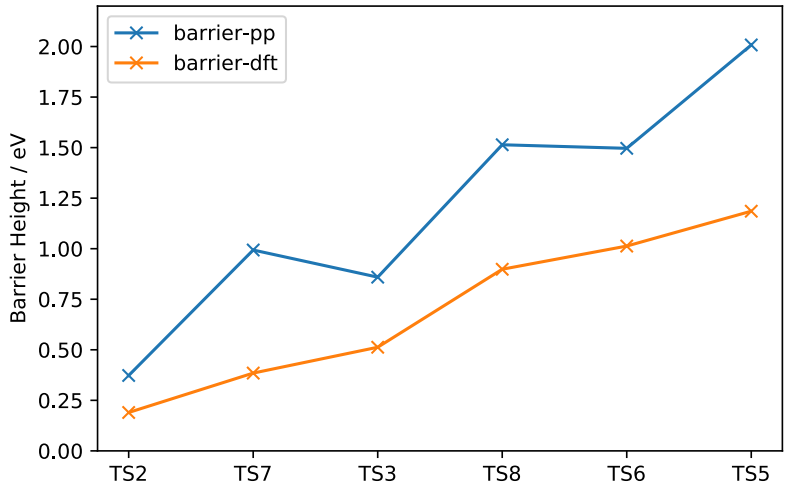

Fig. 6.12 Forward barriers for a range of paths calculated using DFT and an interatomic potential. The latter appears to consistently overestimate by 0.5-1.0 eV.

In real materials, the partially occupied anion sublattice may become disordered at a finite temperature, similar to that in δ-Bi_2O_3 [219]. Further investigation using *ab initio* molecular dynamics (AIMD) are desirable, but can be very challenging because large simulation cells are needed to encapsulate the interface environment.

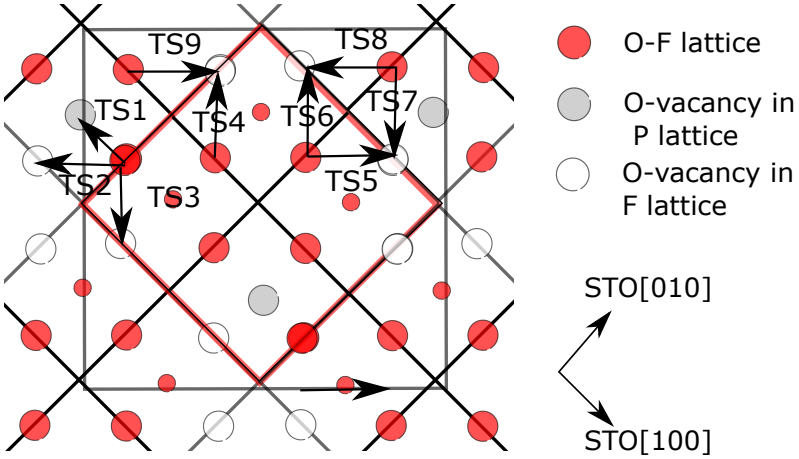

Fig. 6.13 Transition state paths at the SrO-O interface. The red rectangle indicates the search cell, which contains 2×2 pseudo-cubic cells. Oxygen anions are represented by the red circles and empty sites are depicted using hollow circles.

6.7 Conclusion

STO and CeO_2 have different bulk phases. Previously unknown structures of the STO/CeO_2 (001) interfaces are found using AIRSS. The terminations and local stoichiometry at the interfaces are found to have strong influences. A partially occupied anion lattice emerges when STO is terminated by a SrO layer. If STO is terminated by TiO_2, the stable interface structure contains a CeO layer with the rock salt structure. Oxygen vacancy formation energies are computed using the interface structures obtained. The results suggest vacancies are attracted to the interface and become trapped, which hinders ionic conduction in the perpendicular direction. On the other hand, MD simulations show that ionic conduction may be enhanced at the SrO terminated interface due to a partially occupied anion lattice.

The lack of reliable atomistic models for complex heterogeneous interfaces can be overcome by the use of structure searching. Several other systems can be investigated using similar approaches. The interface between $LaAlO_3$ and CeO_2 is an interesting case, since $LaAlO_3$ has the perovskite structure but is polar along the [001] direction. The stable and metastable structures obtained here can be used as prototype models for other perovskite-fluorite systems. Structure searching may also help gain further insights for the $LaAlO_3$/STO interface. The assumption that the bulk perovskite structure is kept at the interface, which is the basis of the polar interface theory [13, 15], needs to be confirmed, especially for the anion lattice, which is often unseen under STEM.

Chapter 7

Octahedral coupling at perovskite-perovskite interfaces

7.1 Introduction

Perovskite structured ABO_3 oxides exhibit a wide range of fascinating properties. They are ideal for making functional thin film devices because of their structural simplicity and being chemically flexible. At ABO_3 interfaces, charge, spin, and orbital orders are closely coupled through the corner connected BO_6 octahedral network [5], as illustrated in the schematic in Fig. 7.1. A prime example of this is the emerging 2D electron gases (2DEGs) at $SrTiO_3$/$LaAlO_3$ interfaces [62], despite the fact that the two constituent phases are both insulators. The requirement of maintaining octahedral connectivity at interfaces gives rise to proximity effects, such that rotations of the BO_6 octahedra in one perovskite can imprint onto the other perovskite [220–222]. These effects have attracted much research attention for tuning film properties and inducing novel functionalities using perovskite-perovskite interfaces [6, 223, 2, 4].

Ultra-thin films that are both ferromagnetic and insulating are needed for generating spin-polarised currents for spintronic and dissipationless quantum electronic devices [224, 225, 37, 38] . However, existing candidate ferromagnetic insulators have relatively low Curie temperature T_c, such as $LaCoO_3$ ($T_c \approx 85$ K) and $BiMnO_3$ ($T_c \approx 105$ K). Materials with high T_c, such as $NiFe_2O_4$ and $CoFe_2O_4$, are less compatible with perovskite-structured electrode materials, preventing the formation of high quality interfaces that are crucial for achieving good performance.

Perovskite structured $La_{0.9}Ba_{0.1}MnO_3$ (LBMO) has been shown to have ferromagnetic and insulating properties in the bulk forms [40, 39]. However, when deposited on $SrTiO_3$

(STO) substrates, LBMO films were found to be electronically conducting and have a ferromagnetic transition temperature T_c of 285 K [226]. However, it was later reported that the insulating state could be recovered in ultrathin LBMO films with 5 unit cells (u.c.) in thickness [41].

In this chapter, first-principles calculations are performed to investigate the lattice and electronic structures of the LBMO and LBMO/STO interfaces. Experimental investigations led by Dr Weiwei Li showed the octahedral tilting in LBMO was suppressed by the interfaces in LBMO/STO bilayer heterostructures and superlattices, which was thought to be related to the change in the electronic and magnetic properties among films with different thicknesses. A few experimental observations can be accounted through simulations of interfaces. However, the predicted octahedral tilt suppressions are much less than observed experimentally. The subsequent study of octahedral network rigidity suggests an alternative tilt configuration can be stabilised at the interface as a result of octahedral corners being pinned. This LBMO phase with $a^-a^-a^-$ tilt configuration is much more susceptible to corner pinning effects of the interfaces.

This chapter is organised as the follows. Section 7.2 gives a summary of the calculation methods and parameters. Section 7.3 presents the results from LDA+U calculations performed for bulk $LaMnO_3$ and LBMO with a focus on the effects of the on-site Coulomb interaction energy U. In Section 7.4, results of interface calculations are presented and discussed with experimental findings. Motivated by the inconsistency between calculated and experimentally observed octahedral tilt suppressions, the octahedral network rigidity is studied in Section 7.5. Section 7.6 presents additional results of network rigidities in other perovskites. Finally, conclusion and outlooks are given in Section 7.7.

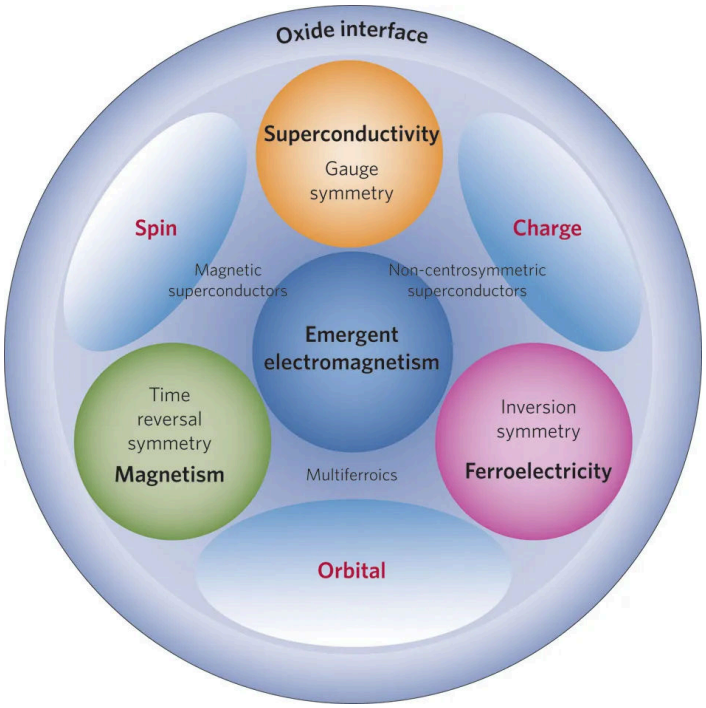

Fig. 7.1 Schematic diagram showing the degrees of freedom of correlated electrons and symmetries. Reproduced with permission from Ref [5]

.

7.2 Methods

DFT calculations are performed using CASTEP [122] with on-the-fly generated core-corrected ultrasoft pseudopotentials, whose generation strings are tabulated in table A.3. The PBE exchange-correlation functional [108] is used in all calculations. A cut-off energy of 600 eV is used for interface calculation, and the studies in Sections 7.5 and 7.6 use a cut-off energy of 700 eV. A set of softer pseudopotentials, tabulated in Table A.1, are used for calculations containing large unit cells, allowing a lower cut-off energy of 350 eV to be used. It is found that theses soft potentials are sufficient for the description of the interface models. The sampling of reciprocal space is performed with a grid spacing of less than $2\pi \times 0.05$ Å^{-1}.

Projected density of states (PDOS) are computed by open source OptaDOS [227] software. During the research, there was a lack of tools for producing *lm* resolved projected DOS from output of CASTEP, which are essential for analysing the crystal filed splitting of the *d* electrons from the transition metal ions occupying the B sties. A modified version of OptaDOS has been developed for obtaining *lb* resolved PDOS data.

7.3 Bulk $LaMnO_3$ and $La_{0.9}Ba_{0.1}MnO_3$

$LaMnO_3$ has a distorted perovskite structure with space group *Pnma*/*Pbnm** [228]. The Mn^{3+} ions have four electrons in the 3*d* orbitals. The octahedral cage consisting of O^{2-} ions around the Mn^{3+} splits its *d* orbitals into doubly degenerate e_g states and triply degenerate t_{2g} states. The former have a higher energy because their electron clouds point towards the O^{2-}.

The conventional cell of $LaMnO_3$ contains $\sqrt{2}\times\sqrt{2}\times 2$ peseudo-cubic units. The MnO_6 octahedral network in $LaMnO_3$ has the $a^-a^-c^+$ tilt pattern. Figs. 7.2a and 7.2c show tilted octahedra viewed along the pseudo-cubic directions. The viewing direction in Fig. 7.2b is used by scanning transmission electron microscopes (STEM) for quantifying the tilt angles, because the oxygen columns are not obstructed by cations, and they are in-phase displaced along the imaging direction.

DFT calculations are performed for bulk $LaMnO_3$ and $La_{0.9}Ba_{0.1}MnO_3$ (LBMO). It is known that DFT often fails to correctly describe transition metal oxides containing localised *d* electrons, which tend to be overly delocalised. The LDA+U correction aims to solve this problem by coupling the Kohn-Sham energy functional with a Hubbard-like hamiltonian of correlated electrons [119, 120]. The on-site Coulomb interaction energy U of the correlated electrons is required as input for the calculation. The value of U is often chosen empirically, although it can also be determined using a first-principles linear response method [121].

Geometry optimisations of $LaMnO_3$ with variable cell size are performed with U ranging from 0 eV to 6 eV. The lattice constants and Mn-O-Mn angles are plotted in Fig. 7.3, and both the A-AFM and FM magnetic ordering are included. For the A-AFM ordering, the Mn atoms in have spins that are anti-parallel between the adjacent MnO_2 (002) planes. Bulk $LaMnO_3$ has lattice constants $a = 5.5353$ Å, $b = 5.7204$ Å, and $c = 7.7029$ Å at a room temperature with Mn-O-Mn angles about 156° [228]. At low temperature, $LaMnO_3$ was found to have A-AFM magnetic ordering, and its lattice constants are $a = 5.5363$ Å, $b = 5.7298$ Å and $c = 7.7622$ Å [229]. The lattice constants of both FM and A-AFM orderings increase with increasing U, as shown in Fig. 7.3. In addition, the A-AFM phase has an abrupt change in b and c lattice constants when the LDA+U correction is turned on. This gives predicted c/a ratios that are more consistent with the experimental values. The MnO_6 octahedral network becomes more tilted with increasing U, as shown by the decreasing Mn-O-Mn angles in Fig. 7.3. Given that the value of U only affects Mn atoms, the observed trend on the ionic structures may be interpreted as if the effective radius of Mn^{3+} being increased with increasing U values.

*These two spaces groups are equivalent, because they only differ in the arrangement of cell vectors.

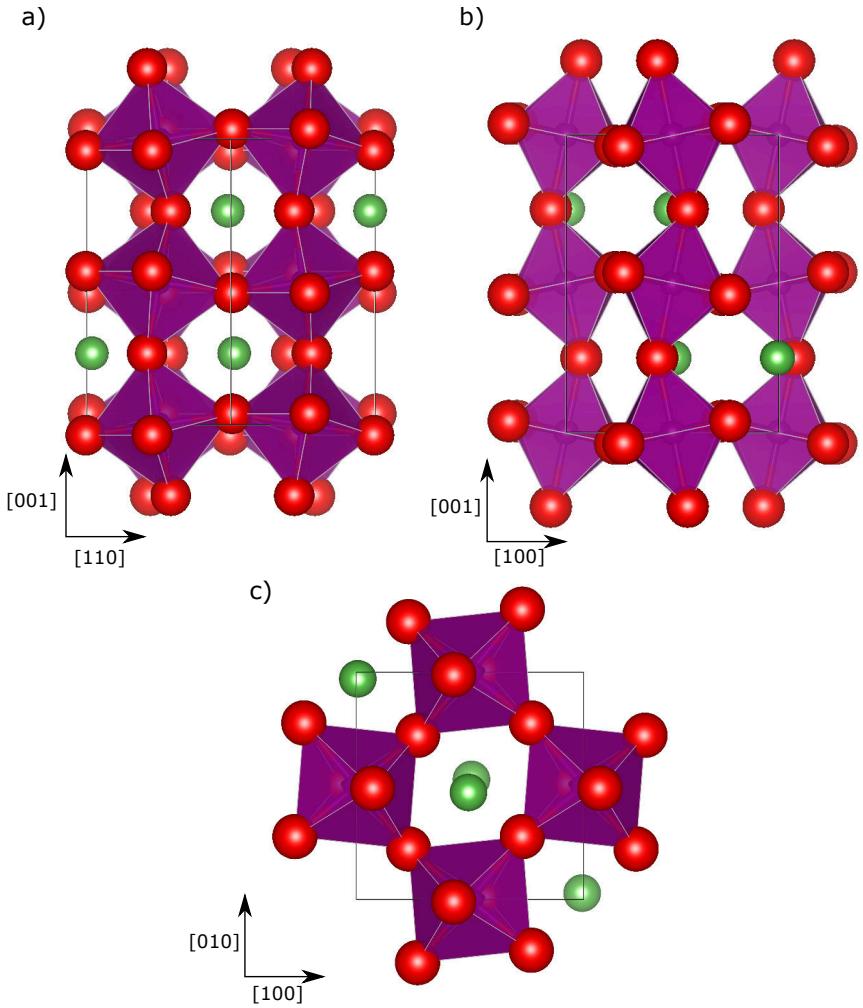

Fig. 7.2 The orthorhombic $LaMnO_3$ structure with $a^-a^-c^+$ rotation pattern. Indicated directions are based on the convention cell vectors. Oxygen atoms are shown in red, lanthanum in purple and strontium in pale green.

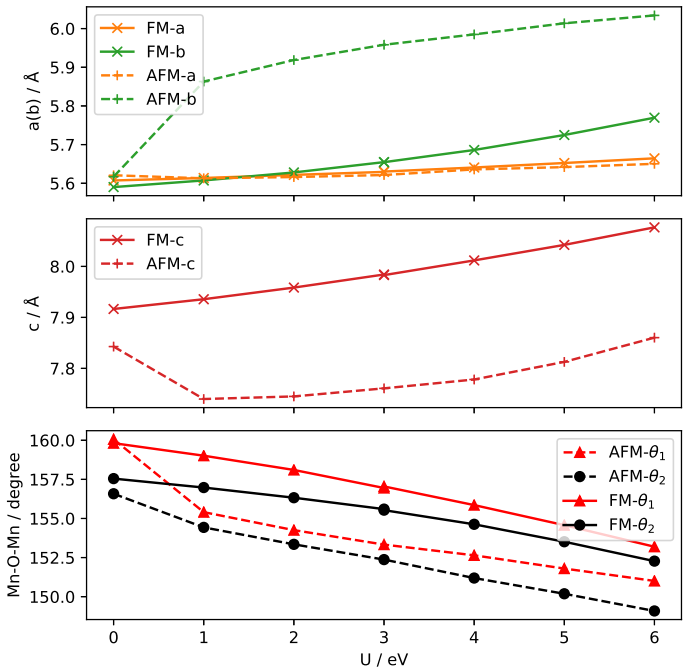

Fig. 7.3 Lattice constants and Mn-O-Mn bond angles oriented perpendicular/parallel (θ_1/θ_2) to the c axis (of anti-phase rotation) in relaxed $LaMNO_3$ plotted against U.

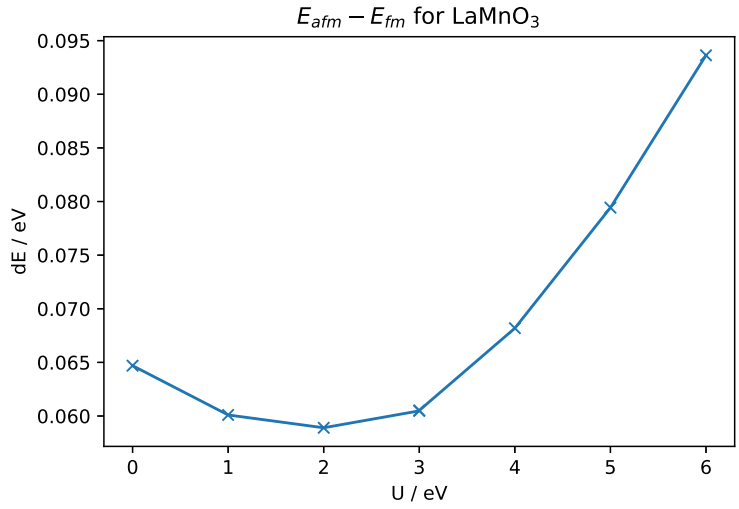

Fig. 7.4 Energy difference between AFM and FM spin states for $LaMnO_3$ per formula unit.

Standard DFT calculations predict FM ordered $LaMnO_3$ to be more stable rather than the AFM state, which is in contradictory to the experimental observations. The energy difference $E_{\mathrm{AFM}} - E_{\mathrm{FM}}$ is plotted for different U values in Fig. 7.4. The Hubbard correction does not solve this discrepancy, as the FM state remains stable for all values of U tested. The minimum

of $E_{\mathrm{AFM}} - E_{\mathrm{FM}}$ is reached when $U = 2$ eV, and the FM ordering is increasingly more stable when $U > 4$ eV. This trend is consistent the work of Mellan et al. [230], although they used the PBEsol functional instead. Also, it should be noted that there is a large spread among the values of $E_{\mathrm{AFM}} - E_{\mathrm{FM}}$ reported in the literature, and a summary can be found in Ref [231].

Fig. 7.5 shows the projected density of state (PDOS) of each element in $LaMnO_3$ with A-AFM and FM magnetic orderings. The fermi level is set to be 0 eV. It can be seen that the valence band is dominated by Mn and oxygen states in both cases, and U appears to redistribute the Mn states inside the valance band. The band gap is opened for the A-AFM ordering only when U is applied, which can be related to the sudden change of the b and c lattice parameters shown in Fig. 7.3. The opened band gap is about 1 eV, and it does not further increase with the value of U. On the other hand, the FM phase is always half-metallic.

PDOS plots of Mn e_g and t_{2g} electrons are shown in Fig. 7.6. The high energy end of the valence band consists of purely e_g electrons, which is consistent with the crystal field splitting. Note that eg and t_{2g} states overlap inside the valence band. The gap between the majority and minority spin states inside the conduction band increases with increasing U. Similar PDOS of Mn d electrons were also reported in literature [232–234].

Based on the results above, a value of 3 eV is chosen for U, because it gives good Mn-O-Mn bond angles, and the FM ordering is not overly stabilised. The target material of this study, $La_{0.9}Ba0.1MnO_3$, is known to be ferromagnetic. Thus, giving a correct description of the AFM/FM stability is not essential here. While U is formally a physical quantity [121], in practice, its value dependents on the choice of exchange-correlation functional, pseudo potentials, and algorithmic implementations. The bottom line is that the findings should not be sensitive to the choice of U.

$La_{0.9}Ba_{0.1}MnO_3$ (LBMO) has the same *Pnma* structure as $LaMnO_3$[39], but with one in ten La atoms substituted by Ba. Each Ba^{2+} cation donates one less electron than La^{3+}, hence the substitution effectively introduces hole doping. Ba^{2+} also has a larger radius compared with La^{3+} (149 pm vs 103 pm) [218]. The Virtual Crystal Approximation (VCA) [235] may be used to simulate impurities. It generates pseudopotentials representing mixtures of elements. The major benefit of VCA is that smaller simulation cells can be used. Gu et al. [236] studied octahedral tilting in $La_{0.67}Sr_{0.33}MnO_3$ using the VCA and found it to give comparable results to explicitly doping. Nevertheless, mixing two dissimilar elements of non-equal valences is not well-justified, and the VCA was originally proposed for modelling alloys. In this work, $LaMnO_3$ is explicitly doped by replacing one out of eight La atoms in a $\sqrt{2} \times \sqrt{2} \times 1$ super cell. This gives an effective doping level of 0.125.

The U dependency of LBMO is very similar to that of $LaMnO_3$ in the FM state (shown in Fig. A.2). Doping with Ba shifts the fermi level to a slightly lower energy, but it is still within

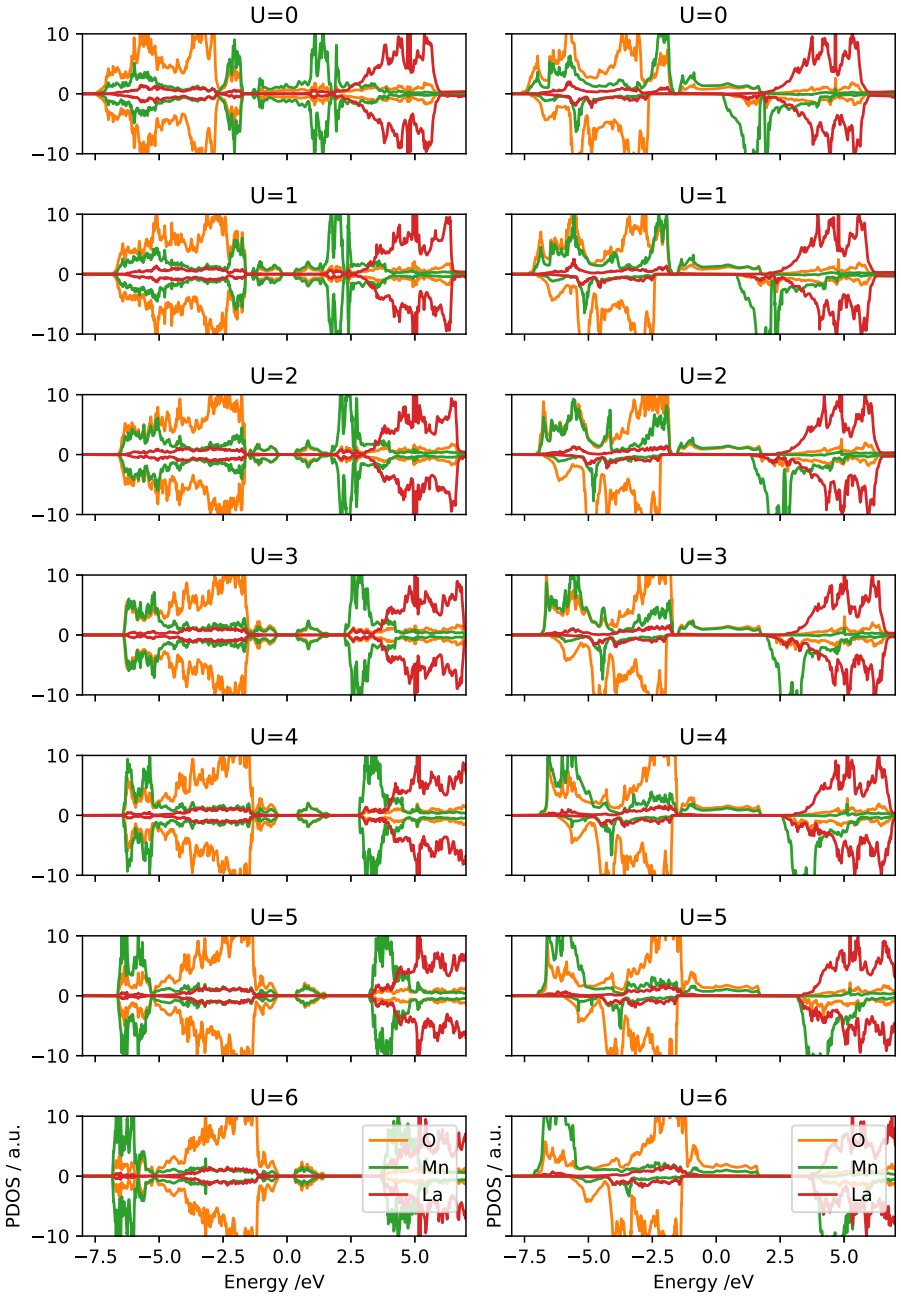

Fig. 7.5 Projected density of states of La, Mn and O in $LaMnO_3$ for a range of U values. The left-hand set of panels corresponds to the AFM state, and the right-hand set of panels corresponds to the FM state. The relaxed geometry was used for each case. The two spin channels are plotted as positive and negative values.

the Mn e_g band, and no band-gap opening is found. The relevant PDOS plots are shown in Fig. A.1. It has been shown that LBMO with higher Ba doping concentrations ($x > 0.12$)

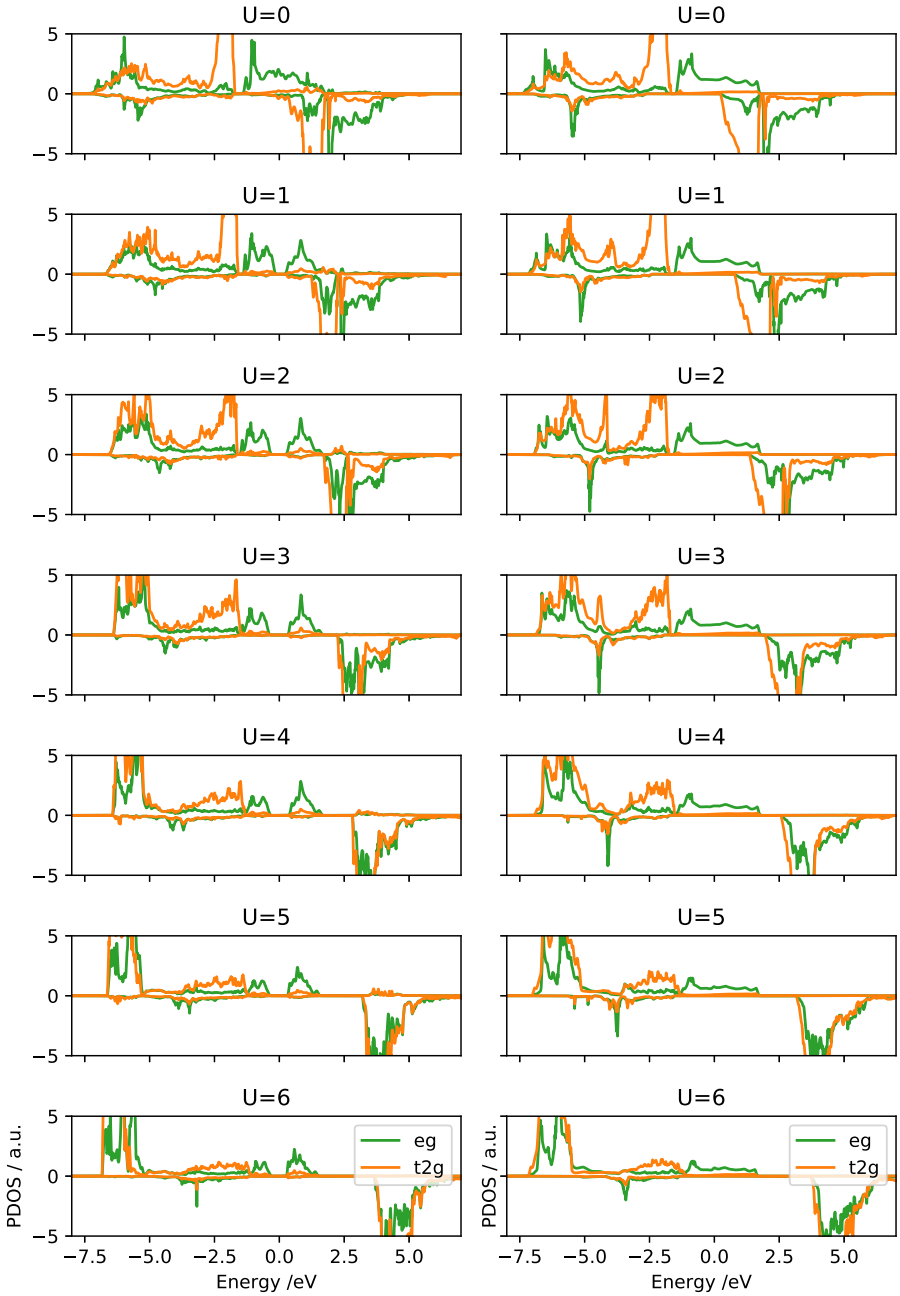

Fig. 7.6 Projected density of states of Mn e_g and Mn t_{2g} states with a range of U values. The left-hand set of panels corresponds to the AFM state, and the right-hand set of panels corresponds to the FM state.

adopts a rhombohedral structure with space group $R\bar{3}c$ [39, 40]. The effective doping level (0.125) in the calculations is slightly above the phase boundary, but the *Pnma* phase is still found to have a lower energy.

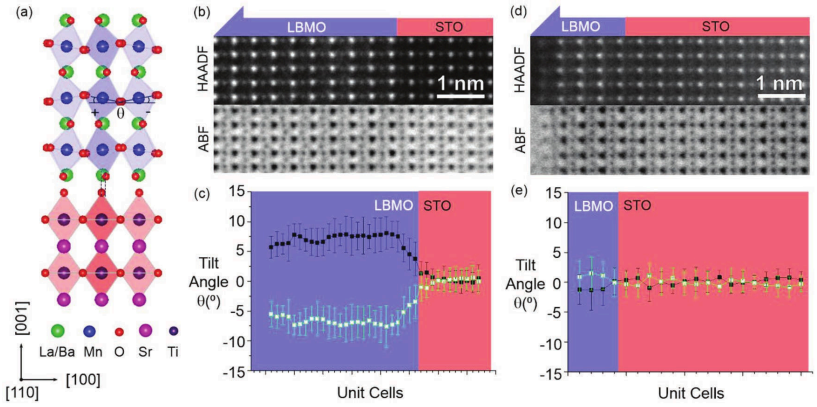

Fig. 7.7 Measured octahedral tilt angles in LBMO/STO bilayer films with (b,c) 40 u.c. and (d,e) 5 u.c. thickness. Reproduced under CC-BY 4.0 License from Ref [42].

7.4 $SrTiO_3/La_{0.875}Ba_{0.125}MnO_3$ interfaces

The studies of $SrTiO_3$(STO)/LBMO interfaces were carried out in collaboration with the experimental investigations conducted by Dr Weiwei Li and other collaborators. The LBMO films deposited on Nb-STO substrates are found to be insulating below a critical thickness of eight unit cells (u.c.). Scanning transmission electron microscope (STEM) images show octahedral tilts being suppressed near the film-substrate interface in the bilayer sample with a LBMO thickness of 5 u.c., which can be seen in Fig. 7.7d&e. The tilt suppression is also found in the 40 u.c. sample, but it is not as strong, shown in Fig. 7.7b&c.

DFT calculations are performed to investigate the structure and properties of LBMO/STO (001) interfaces. The simulation cell contains $2 \times 2 \times 4$ units of STO and $2 \times 2 \times 8$ (pseudo-cubic) units of LBMO, which are stacked in an asymmetric slab configuration with a vacuum of 15 Å separating the periodic images. Based on the experimental conditions and characterisation results, the LBMO film is assumed to be fully strained to the STO substrate, and the latter terminates with a TiO_2 plane. The lateral lattice constant is set to $3.98 \times 2 = 7.96$ Å for keeping LBMO under the tensile strain state that is consistence with the experiment, as its equilibrium volume is increased by U. Significant reductions in octahedral tilt at the interfaces are observed in the STEM images displayed in Fig. 7.7. However, much less reduction in the tilt angles are found in the relaxed interfaced structures. In order to simulate the experimental observed structures, constrained geometry optimisations are performed with all atoms in the STO substrate being fixed to their positions in the bulk phase. The DFT ground state structure of STO has $a^0a^0a^-$ tilt configuration, whilst the STEM images were taken at room temperature, under which the undistorted cubic phase is stable. Constraining

the atomic positions makes the STO infinitely rigid, which also means that the coupling between the two octahedral networks is maximised.

The relaxed structure of LBMO/STO film-substrate interface is shown in Fig. 7.8a&b. To compare with the tilt angles measured under STEM, views along the STO[110] direction are simulated by projecting the atomic positions on a plane, as shown in Fig. 7.8c. Fig. 7.8e illustrates the definition of angle θ. It should be noted that the exact Mn-O-Mn angles cannot be measured under STEM, but the angle θ is expected to reflect the magnitude of the tilt along the two in-plane axes. The angle θ is found to be 12° in the bulk region of the relaxed interface (Fig. 7.8a), and it reduces to 8° at the film-substrate interface, as shown Fig. 7.8d.

Layer-resolved PDOS plots for Mn 3d electrons are displayed in Fig. 7.9a. The states of the oxygen atoms in the adjacent layers are also included. The Mn atoms at the interface have a slightly reduced e_g bandwidth (Fig. 7.9a, bottom plot) compared with that in the middle of the slab. In addition, the overlap between the Mn and O states is reduced at the interface, as shown in the inset. The layer-resolved per-species PDOS plots in Fig. 7.9b suggest that the conduction band comprised of Ti 3d states in STO is occupied at the interface. The electrons injected into the Ti 3d band are spin polarised, and the net spin is parallel to that of the adjacent Mn atoms, which can also be seen in the spin density shown in Fig. 7.9c.

The film-vacuum interface is found to strongly affect the octahedral network. Fig. 7.8d shows that the inclination angle θ is reduced at the surface, and the reduction penetrates up to four layers into the film. It is likely that a surface reconstruction takes place in reality, as the polar surfaces are inherently unstable [237]. The reducing tilt angles can be explained by a reduction of the effective radii of the Mn^{3+} due to electron deficiency in the MnO_2 surface layer.

Surfaces effects may be avoided in superlattices. Two models with four (L4S4) and eight (L8S8) layers of LBMO and STO are used in the studies. The inclination angle measured for each layer is plotted in Fig. 7.11. The atoms in the STO layer are fixed initially, and subsequently allowed to relax. The cell vectors are fixed during the relaxations. As expected, the tilt suppression is further reduced in the fully relaxed structures. In addition, the $a^-a^-c^+$ tilt in LBMO propagates into STO, giving the latter inclination angles of about 6°. Unlike the bilayer films, superlattices contain two interfaces: one is formed between a SrO layer and a MnO_2 layer, and the other is formed between a TiO_2 layer and a LaO layer. Fig. 7.11 shows the tilt suppression from the SrO-MnO_2 interface is stronger than that of the TiO_2-LaO interface. This can be related to the radius of Sr^{2+} being larger than that of La^{3+}, hence the former gives stronger pinning for the corner anions that are within the layer. It should be noted that the asymmetry still exists even if the STO block is fully fixed, which indicates that pinning of corners is not the only cause of the tilt suppression.

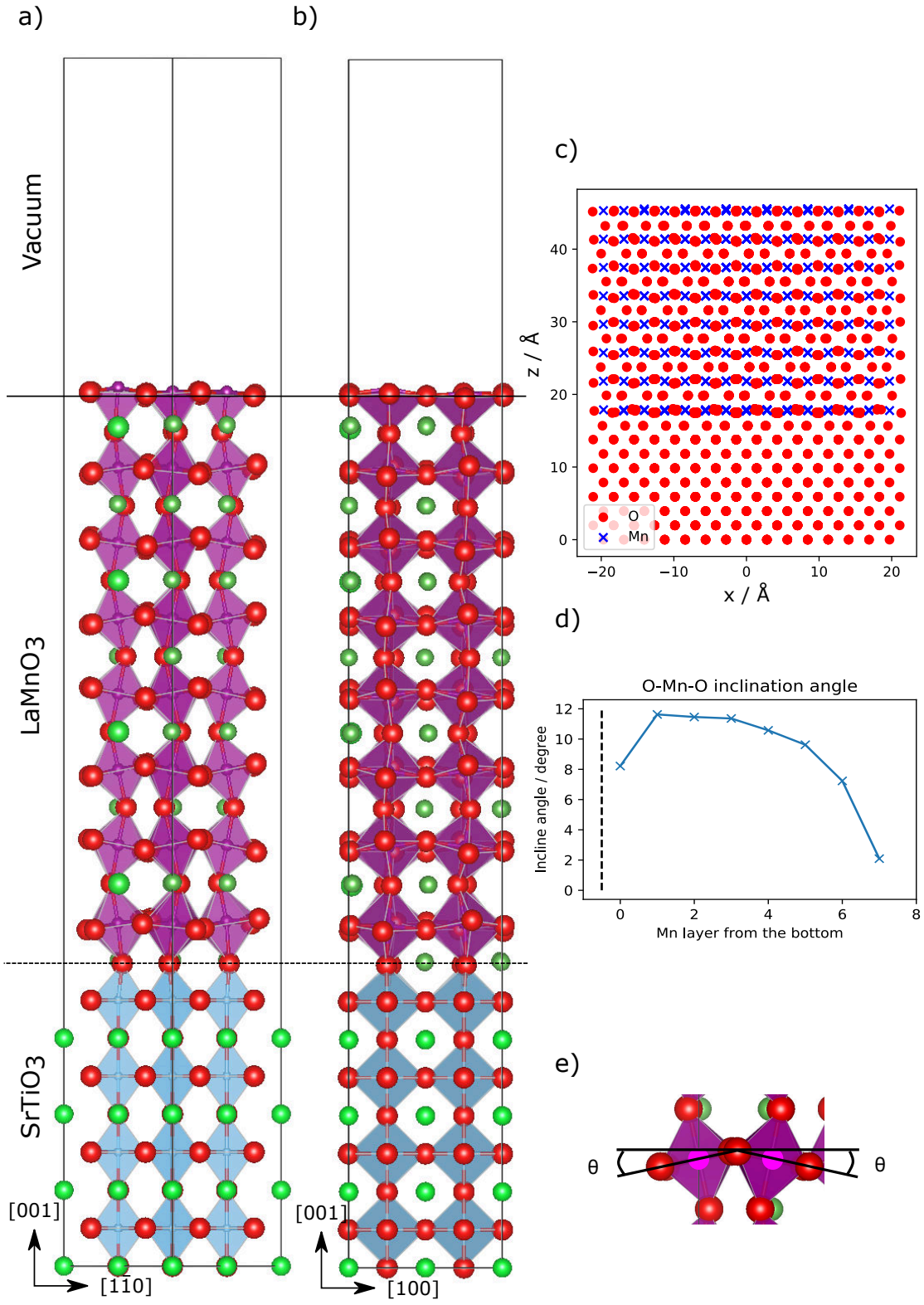

Fig. 7.8 a) The simulation cell viewed along the STO[110] direction. b) Viewed along the STO[010] direction. c) A schematic of the projected atomic positions and tilting viewed along STO[110] direction. Oxygen atoms are represented as circles, and Mn atoms are marked by crosses. d) The O-Mn-O inclination angles in the interface model, as computed from Fig. 7.8c.

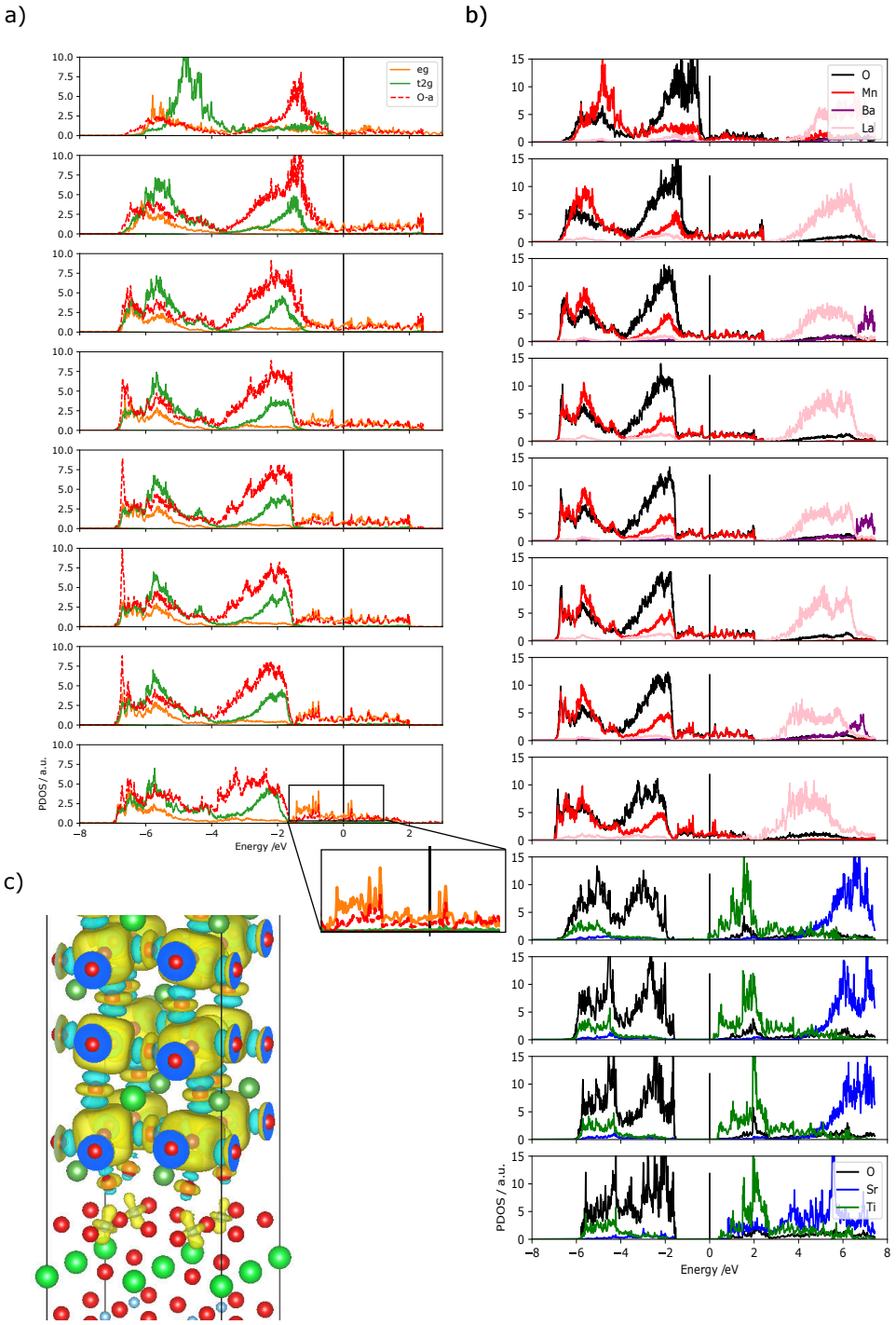

Fig. 7.9 a) Layer-resolved PDOS showing Mn 3d e_g-t_{2g} electrons. The states projected onto oxygen atoms in the adjacent layers are also included. Each subplot correspond to a single MnO_2 layer as shown in 7.8a&c. b) Layer-resolved per-species projected PDOS. The conduction band of Ti is occupied at the interfacial layer. c) A plot of the spin density isosurface (0.01). The Ti atoms at the interface are spin-polarised in parallel with the Mn atoms over them.

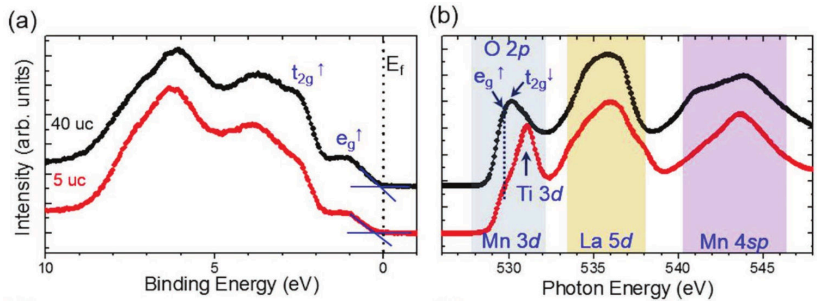

Fig. 7.10 X-ray photoemission spectroscopy and X-ray absorption spectroscopy measurements indicate a change of occupation at the valance band maximum and reduction of the Mn3*d*-O2*p* hybridisation. Reproduced from Ref [42] (Licensed under CC BY 4.0).

The layer-resolved PDOS of the superlattice models have features similar to that of the bilayer model. However, the fully relaxed structures remain insulating, and the Ti 3d orbitals are unoccupied. Similar behaviour was reported for the $LaAlO_3$(LAO)/$SrTiO_3$ interface, where the lattice relaxation is to found to increase the number of layers needed to get a conducting interface [185]. To show the effect of lattice relaxation, the averaged ionic displacement along z is computed for each layer. Cation (anion) displacements in the $+z(-z)$ direction are defined as positive, and the results are displayed in Fig. 7.12. The displacements inside the STO can be attributed to electric field caused by charged LaO $(+1)$ and MnO_2 (-1) layers surrounding it. In addition, the displacements in the LBMO is also affected when the STO is fully relaxed, as shown in Fig. 7.12. This is less noticeable inside the L8S8 structure, which can be explained by the reduction of electric field strengths due to increased STO thickness.

The experimental findings and their connections with the calculations are discussed in the following. Samples of LBMO/STO bilayer films and superlattices are deposited by Dr. Weiwei Li, and characterisations were done in collaboration with other researchers. As mentioned above, tilt suppression was observed in the bilayer films using STEM annular bright field (ABF) imagining. Similar effects were also found in the superlattices containing eight unit cells of STO and LBMO using the integrated differential phase-contrast (iDPC) [238] images, which were captured by Dr. Ruixu Zhu. In Fig. 7.13, the tilt angle inside in the LBMO (2°) is significantly lower than that of the bulk. Notably, tilted octahedra are also found inside the STO. On the other hand, DFT calculations suggest bulk LBMO has an apparent tilt angle of 12°. The TiO_2-LaO and SrO-MnO_2 interfaces give reduced angles of 8° and 3° respectively, and the reductions are halved when the STO side is allowed to relax. It should be noted that the atomic positions displayed in the micrographs are in fact for columns of atoms, and oxygen atoms may not fully align within each column. Because STEM images are sensitive to the image conditions, there can be some systemic errors. The angles extracted

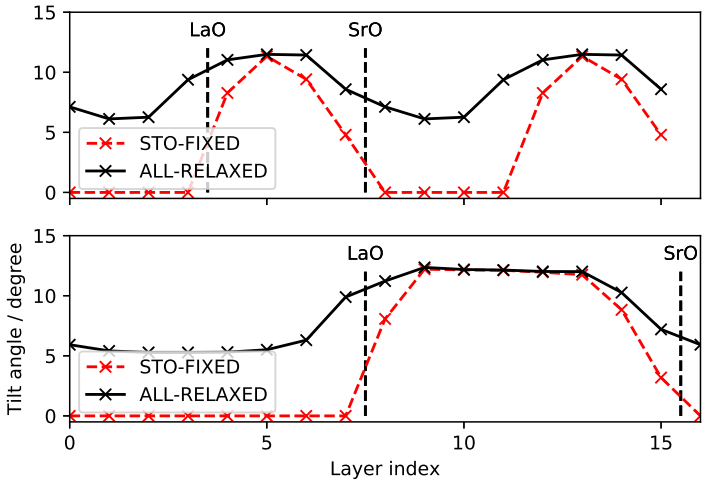

Fig. 7.11 Inclination angles of the O-Mn/Ti-O lines when viewed along STO[110] direction inside the superlattice structure. The top panel: STO-LBMO 4/4 superlattice. Bottom panel: SOT-LBMO 8/8 superlattice.

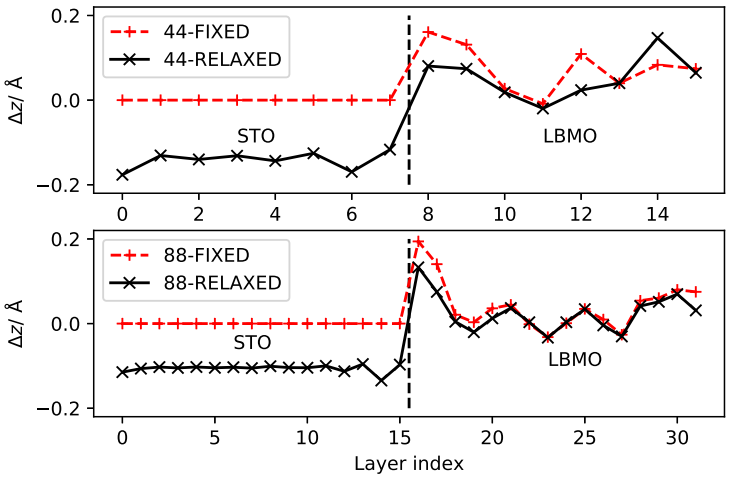

Fig. 7.12 Average ionic displacement within each layer with respect to the mean position. Positive values for displacement of cation in the z direction or anion in the $-z$ direction.

from interface models are measured from averaged projected oxygen positions, whilst STEM images have more complex contrast mechanisms. Nevertheless, there is still significant inconsistency regarding the magnitude of the tilt suppression.

The electronic transport measurement performed by Dr Weiwei Li indicates the films of LBMO are insulating when their thicknesses were below 8 u.c.. This is further supported by valence band spectra measured using X-ray photo emission spectroscopy (XPS), shown in Fig. 7.10a. The spectra also have characteristic peaks arising from the t_{2g} and e_g electrons, and their overall shape resembles the computed density of states. X-ray absorption spectroscopy (XAS) effectively probes unoccupied states in the conduction bands. The characteristic Mn 3d peak in the O-K edge spectra is reduced in 5 u.c. sample compared with the 40 u.c. sample, as shown in Fig. 7.10b. This suggests the Mn3d-O2p hybridisation is reduced in the 5 u.c. sample. Meanwhile, the calculations indicate slight reductions in the e_g bandwidths, with the overlap between O and Mn states being reduced at the interface. X-ray circular magnetic dichroism measurements on Ti L-edges show emerging magnetism from Ti in parallel with that of the Mn atoms, which is consistent with the charge transfer and Ti ferromagnetism observed in the calculations. In addition, X-ray linear dichroism measurements at the Mn L_2 edge suggest a preferential occupation of the out-of-plane $d_{z^2-r^2}$ orbital. This is also found in the PDOS analysis of both bilayer and superlattice models. More details of the experimental results can be found in Ref [42].

The critical thickness for achieving insulating interface is increased in superlattice samples. The samples consisting of less than 12 u.c. of LBMO are found to be insulating, in comparison, the critical thickness of bilayer films is 8 u.c.. This can be attributed to LBMO/STO superlattices having two perovskite-perovskite interfaces per LBMO block.

In summary, DFT calculations of the LBMO-STO interfaces in the bilayer and superlattice models can account for some experimental findings, including the subtle changes in the O-K edge XAS spectra, the XPS valence band spectra, the emerging Ti magnetisation under XMCD, and preferential out-of-plane occupations of the Mn e_g measured with XLD. However, there are two key results not reproduced by the DFT calculations. First, the insulator to metallic transition with film thicknesses is not reflected in the first-principles calculations. This can be an inherent problem of the LDA+U method, as it may not fully capture the correlation effects of Mn 3d electrons. Second, the experimentally observed tilt suppressions are much greater than those found in the relaxed interface structures. Whilst the models assume the interfaces are atomically sharp, in reality, cation mixing is likely to occur. Another issue is that the observed tilting under STEM only confirms that the configuration is a^-a^- along the two pseudo-cubic axes parallel to the interface. The tilting along the axis

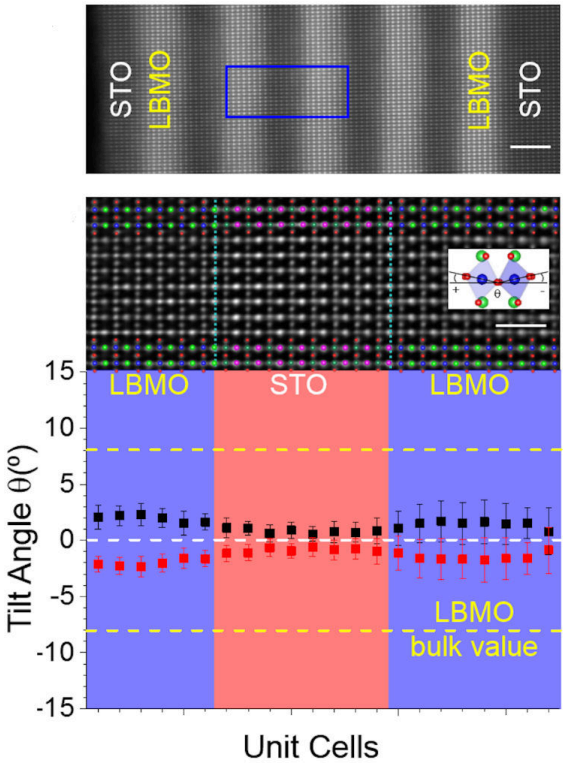

Fig. 7.13 STEM HAADF images showing the LBMO8-STO8 superlattice (top). Tilting of the octahedra can be seen in the i-DPC image (middle). Measured tilt angles indicates a suppression of the tilting inside the LBMO region, down to 2°, note that tilting is also found in the STO block (bottom). Courtesy of Dr Weiwei Li and Rui Zhu.

perpendicular to the interface cannot be determined. It has been assumed, so far, that the tilting is in-phase along this direction, which is the same as that in the bulk phase.

7.5 Perturbing octahedral networks

The octahedral network must be continuous across the interface, even if the two bulk constituent materials have different tilt configurations and/or magnitudes. As a first approximation, tilt suppression can be considered as a response to the displacements of the corners. This is illustrated in Fig. 7.14 for $LaMnO_3$, where the directions of the corner anion displacements are marked by the arrows. When interfaced with an infinitely rigid cubic perovskite, the anions are forced to take positions directly above/underneath the B site cations. Materials with such infinitely rigid structures are of course hypothetical, but the flexibility of the octahedral network can be deduced from the changes in structure and energy when external perturbations are applied to the corner. For very flexible networks, the energy costs of moving the corners should be small, and the distortion can propagate into the bulk material. On the other hand, moving the corners of a rigid octahedral network would incur high energy costs, and any changes would be localised to where the displacements are applied.

Motivated by the inconsistency between the predicted and the observed tilt suppressions at LBMO/STO interfaces, the network rigidity is investigated for the relevant materials by performing constrained DFT geometry optimisations. The anions in the *AO* planes are moved in analogy to the pinning effect of an interface. The perturbation $\Delta\vec{d}$ is chosen to be parallel with the existing displacement $\vec{d}$, which is given by $\vec{d} = (o_x - B_x, o_y - B_y)$, where B_x and B_y are the x and y coordinates of the B site cation directly above/below the anion, as illustrated in Fig. 7.15. The anions in one of the two (002) *AO* planes (coloured red) perpendicular to the c^+ axis are displaced. The x and y coordinates of the displaced anion and that of the adjacent B site cations are fixed in the relaxation. First, the structure is fully relaxed, including all cell vectors. Then a collection of perturbed frames are created using on the fully relaxed structure, and they are subsequently optimised with the constraints applied. The cell parameter is allowed to change along the [001] (c) direction during the relaxation, while keeping other components fixed.

The changes in energy ΔE_{tot} under a range of perturbation magnitudes are shown in Fig. 7.16 for STO, $LaMnO_3$ (LMO) and LBMO. All of them are initially in the *Pnma* structure with $a^-a^-c^+$ tilt configuration. The tilt angle θ_0 is measured between the out-of-plane B-O bond and the z direction, as indicated in Fig. 7.15. Positive perturbations, e.g. parallel to the existing displacements, increase the angle θ_0. LMO and LBMO have almost identical changes in energy with a given perturbation magnitude Δd. On the other hand, the equilibrium tilt angle is reduced in LBMO compared with LMO, which can be explained by Ba^{2+} having larger radius than La^{3+}. The curves of STO, as shown in Fig. 7.16, suggest its octahedral network is much more susceptible to distortions. Notably, a full relaxation of the *Pnma* structured STO does not recover its cubic phase, which is consistent with the fact

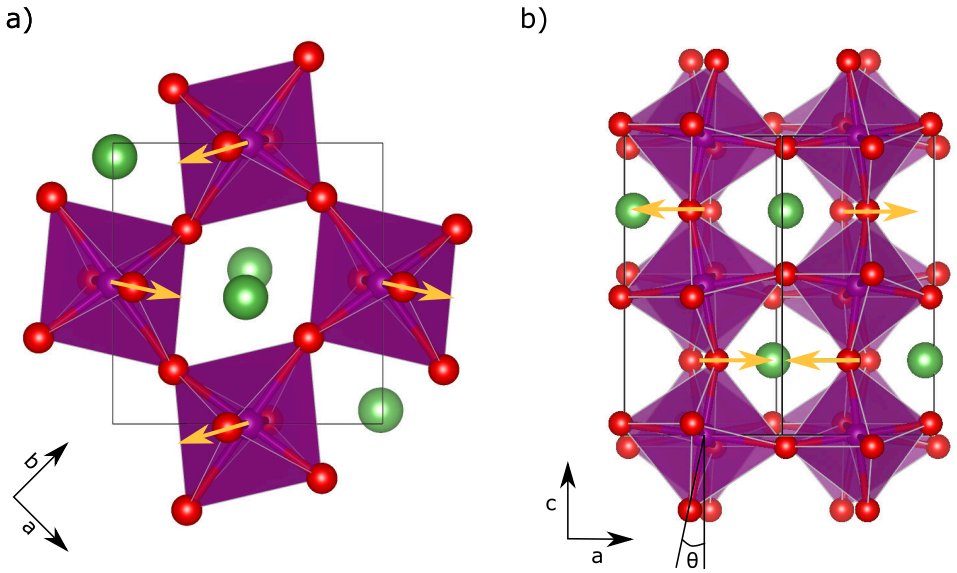

Fig. 7.14 $LaMnO_3$ in the *Pbnm* structure viewed along a) [001] and b) [110] directions. The three pseudo cubic directions are labelled by a, b and c. The displacement of the octahedral corners (anions) are depicted by the arrows.

that the cubic phase is a saddle point in the configuration space. It is known that the ground state of STO is the anti-ferrodistortive (AFD) $I4/mcm$ phase ($a^0a^0c^-$) [209]. The $I4/mcm$ phase has almost flat response curves. It turns out the *Pnma*-like corner displacements make the anti-phase rotation (c^-) axis switch from the c (z) direction to the b direction. These results suggest STO is a rather poor choice for controlling octahedral rotations via interface coupling.

Given that the BO_6 octahedral network in STO is much softer than that in LBMO, the observation of reduced tilt angles in LBMO superlattices and bilayer films is rather intriguing (Figs. 7.7 and 7.13). So far it has been assumed that LBMO films have the *Pnma* structure, which is the same as in bulk material [42, 39, 40]. On the other hand, bulk LBMO with a higher doping concentration is in the $R\bar{3}c$ phase with $a^-a^-a^-$ tilt configuration similar to that of $La_{0.67}Sr_{0.33}MnO_3$[239]. The same corner displacement "experiment" are performed with LMO and LBMO in the $R\bar{3}c$ phase (r-LMO/r-LBMO). The results are displaced in Figs 7.17 and 7.18 respectively. In both plots, the DFT total energy is shown in the upper plane for comparison. The r-LMO is metastable and has a higher energy than LMO, and its instability is reflected by a slight decrease of energy under a small positive corner displacement (Δd), which breaks the three-fold symmetry. On the other hand, the octahedral network of r-LMO is more susceptible to distortions, as shown in Fig. 7.17. Because of this, r-LMO can have a lower energy when the corners are displaced. The cross-over takes place at $\theta_0 \approx 8^\circ$.

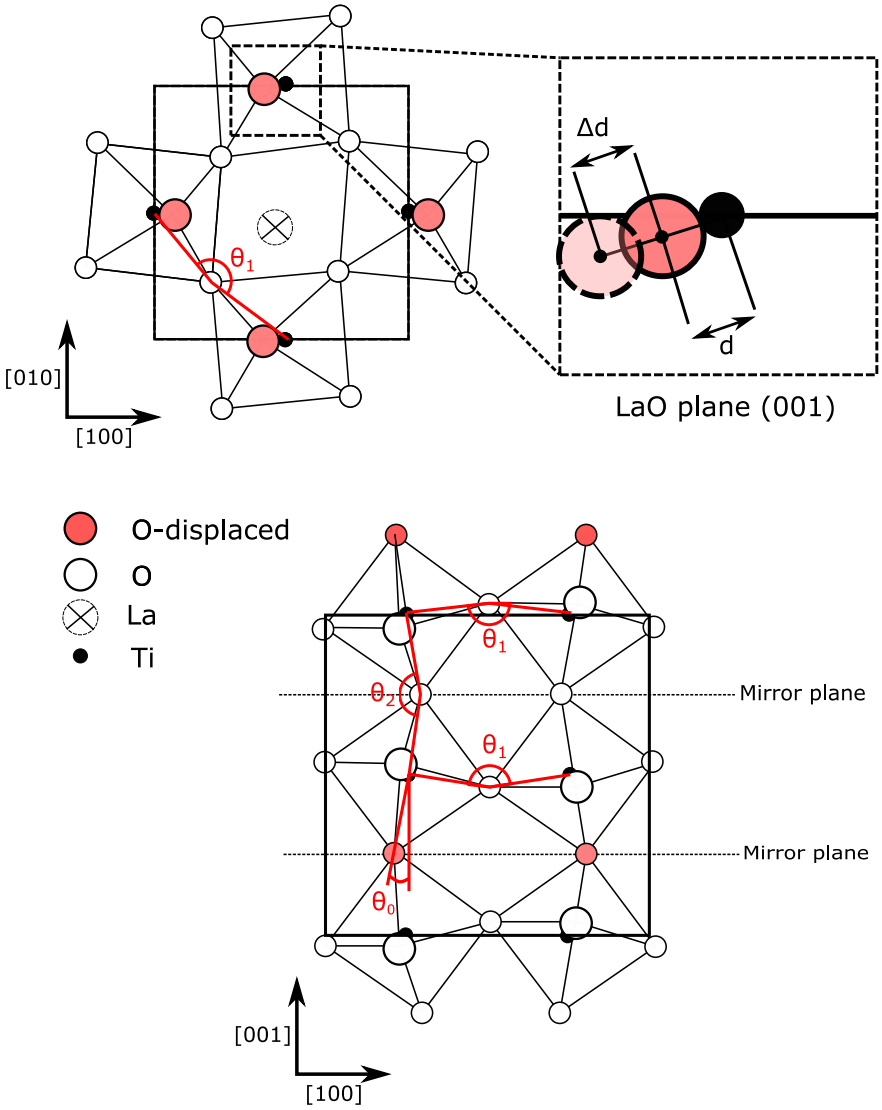

Fig. 7.15 A schematic of the octahedral rotation pattern ($a^-a^-c^+$) showing in-plane (θ_1) and out-of-plane (θ_2) Mn-O-Mn angles. The tilt angle θ_0 is defined with respect to the z axis, and its corresponding Mn-O-Mn angle is given by $180 - 2\theta_0$.

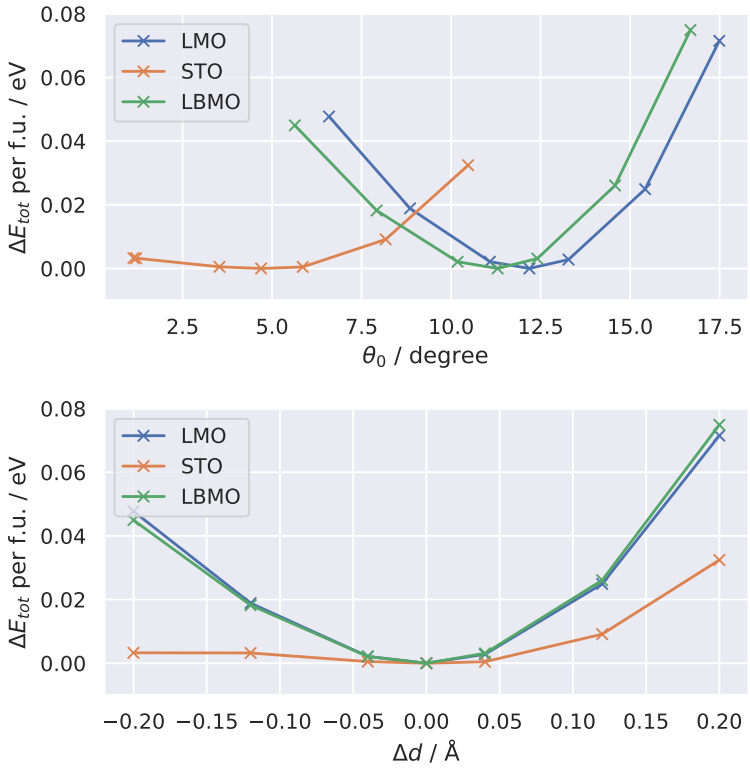

Fig. 7.16 Energies of perturbed structures plotted against the tilt angle (with respect to z) and the magnitude of the introduced displacements. All structures are in the *Pnma* phase.

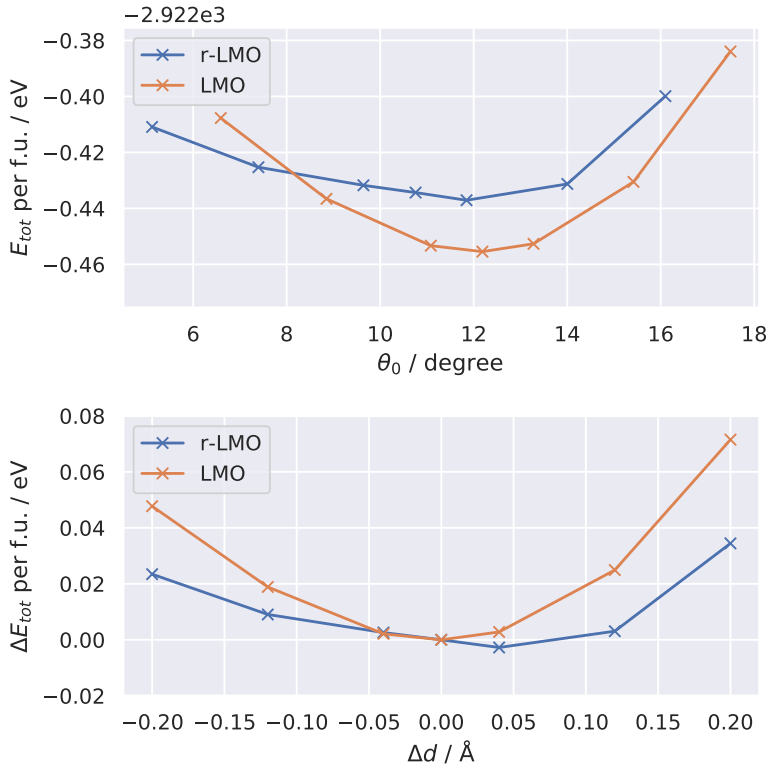

Fig. 7.17 Response curves to anion displacement for LMO in *Pnma* and $R\bar{3}c$ phases. DFT total energies are plotted in the upper panel, and the lower panel shows relative energy changes.

Similar results are found for LBMO and r-LBMO, whose response curves are plotted in Fig. 7.18. Notably, the energy difference between the two phases before applying any perturbations is much smaller compared with that between r-LMO and LMO (5 meV per f.u. vs 20 meV). This is consistent with the dopant effects, which are known to stabilise the $R\bar{3}c$ phase with increasing concentrations [39]. As a result, only a small reduction of 1.8° in θ_0 is needed to make r-LBMO stable, as shown in 7.18.

The curves of r-LBMO and r-LBMO are asymmetric, and the energy cost of reducing tilt angles are smaller than that needed to increase them. To study the cause of this, the Mn-O-Mn bond angles are plotted against the magnitude of corner displacements Δd in Fig. 7.19. The θ_1 and θ_2 are the in-plane and out-of-plane angles respectively, as shown in Fig. 7.15. In both materials, θ_2 decreases with increasing Δd, which is consistent with the increased octahedral tilt along the two in-plane pseudo-cubic axes (a and b). The value of θ_1 also decreases with increasing Δd in the orthorhombic *Pnma* phase. However, θ_1 in the rhombohedral phase ($a^-a^-a^-$ tilt) has an increasing trend with decreasing θ_2.

The tilted octahedra under the perturbations are shown in Fig. 7.20 and Fig. 7.21 respectively. The octahedral tilt along the c axis, shown in the first row marked by the circles, barely changes in the *Pnma* structure with increasing Δd, whilst that of the $R\bar{3}c$ phase decreases, compensating the increased rotations along a and b. This explains the shape of the response curve in Fig. 7.19 and Fig. 7.17, where the energy cost of perturbing the octahedral network is much smaller with $a^-a^-a^-$ tilt configuration . The asymmetric shape of the response curves can be attributed to the rotations along c being completely suppressed when d increases, but it is free to increase when d decreases.

So far only small unit cells are used when computing the response. The cell size in the c direction may be increased to investigate the coupling length of corner displacements. The response curves of LBMO computed with twice the cell size along c is shown in Fig. 7.22. For a given Δd, the change in energy per formula unit is halved, but this is because only half of the *AO* planes are perturbed. The two lines overlap with each other when this is taken into account. In contrast, the response curves of the extended r-LBMO model deviate from that of the standard model, indicating the distortion of the octahedral network can propagate further into the material.

In Fig. 7.23, the average Mn-O-Mn bond angles in the extended LBMO and r-LBMO models are plotted against the Δd applied to the networks. Those angles marked with $'$ are measured further away from the LaO plane being perturbed. The overall offsets are due to the explicit Ba substitution. It can be seen that θ_1' and θ_2' of the orthorhombic phase are almost unaffected by the perturbations. On the other hand, θ_1' and θ_2' of the rhombohedral

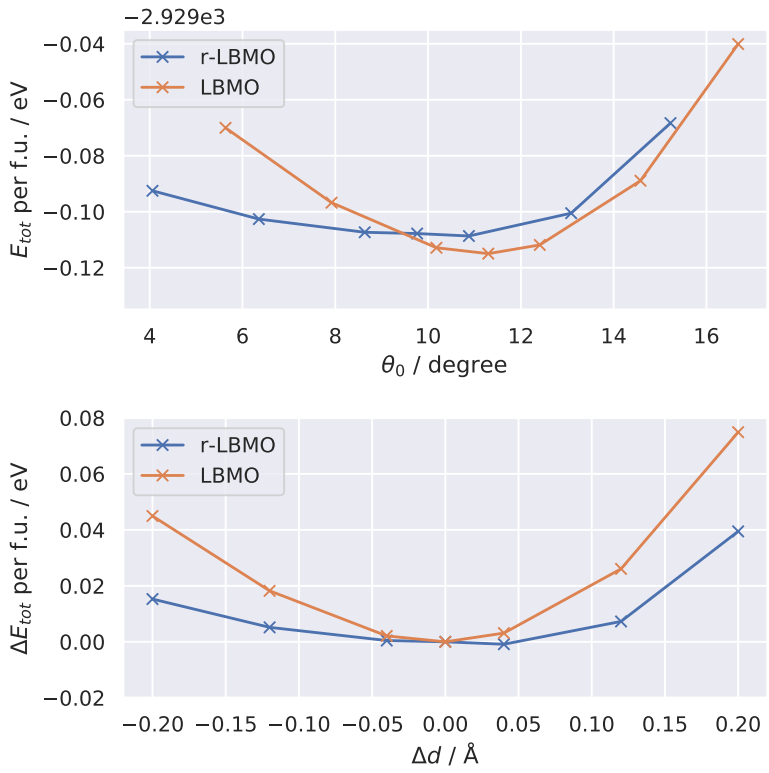

Fig. 7.18 Response curves to anion displacement for LBMO in *Pnma* and $R\bar{3}c$ phases. DFT total energies are used in the upper panel, and the lower panel shows relative energy changes.

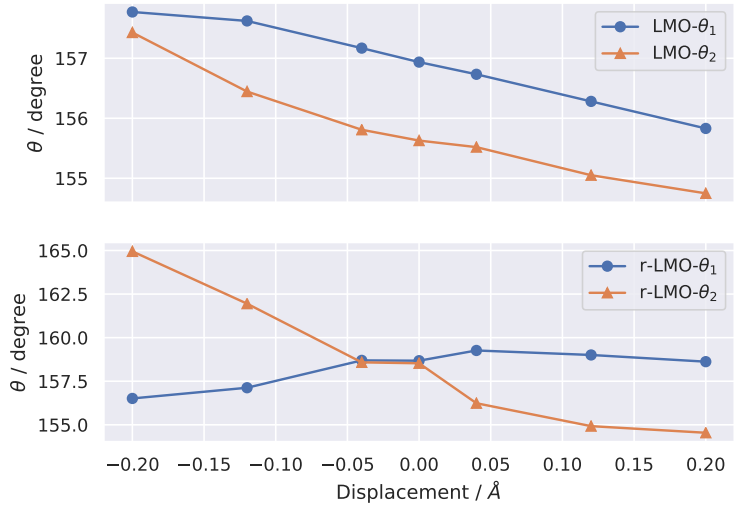

Fig. 7.19 Change of Mn-O-Mn angles in response to the anion displacements. θ_1 and θ_2 are the two inequivalent in-plane Mn-O-Mn angles, and θ_3 is the out-of-plane Mn-O-Mn angle where O is not directly distorted.

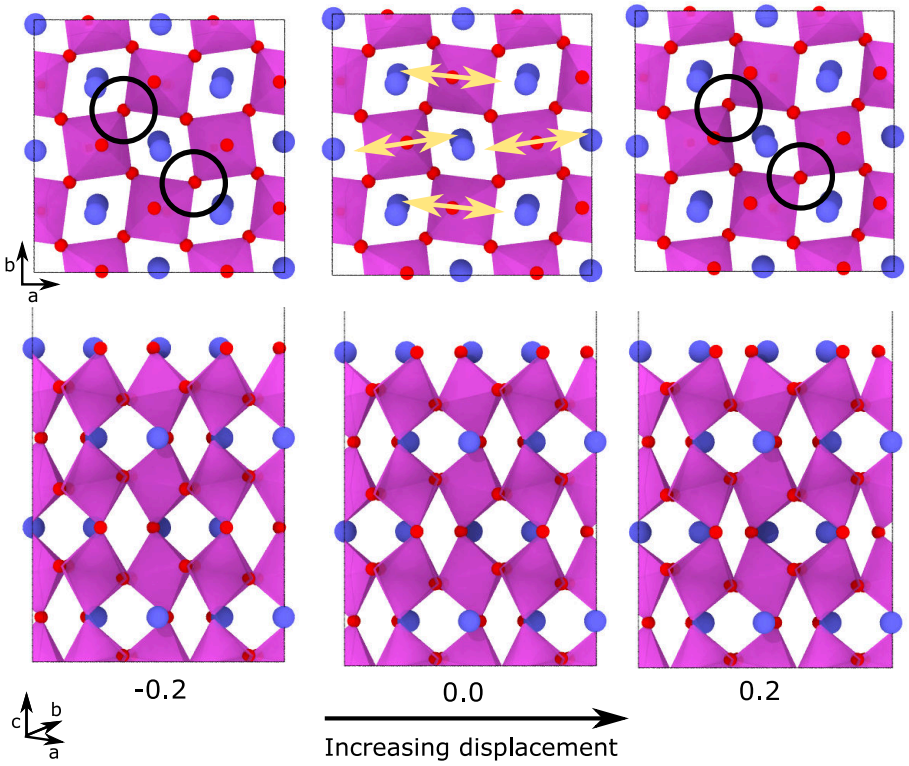

Fig. 7.20 Structures of *Pnma* LMO viewed along *c* (upper) and *b* (lower) directions with increasing distortions.

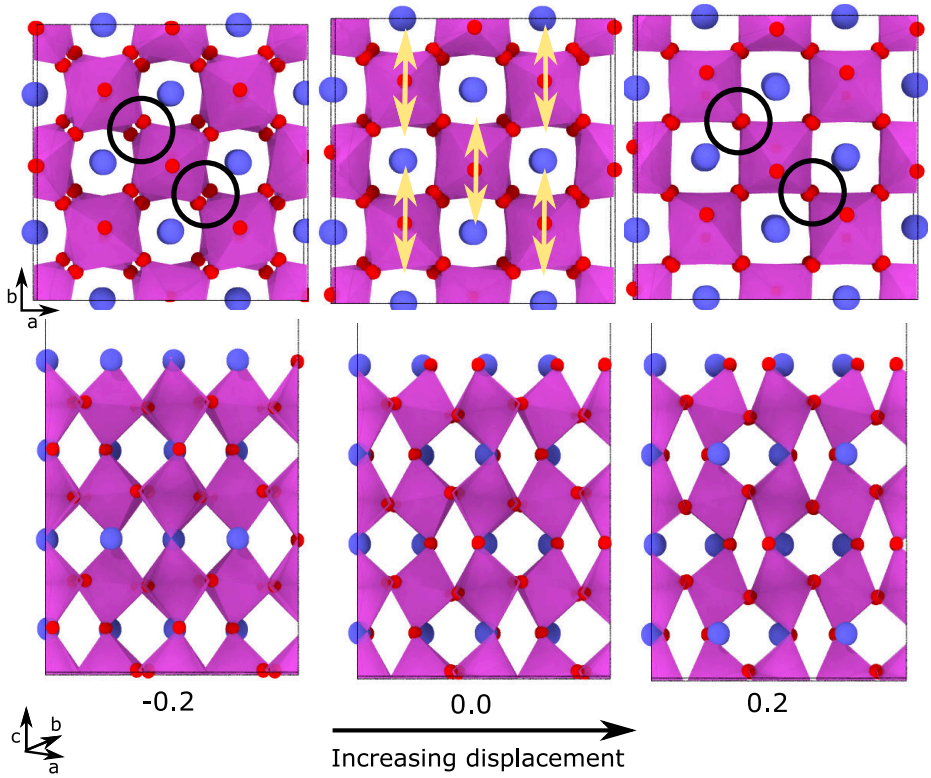

Fig. 7.21 Structures of $R\bar{3}c$ LMO viewed along c (upper) and b (lower) directions with increasing distortions.

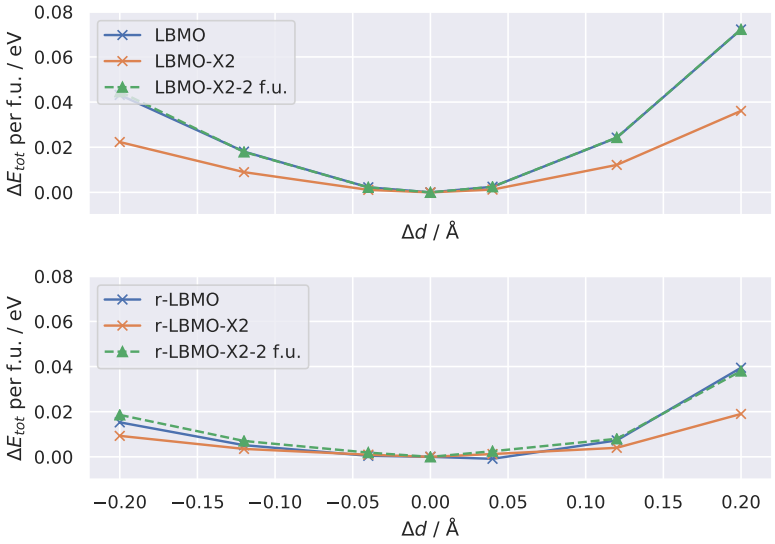

Fig. 7.22 Response curves of (r)-LBMO with doubled cell sizes along c.

phase closely follow their counterparts in the plane closer to the perturbation. The interfacial tilt suppression in the *Pnma* phase is highly localised.

The octahedral proximity effects have also been studied by a few prior works. He et al. [240] investigated the effect of interfacial symmetry mismatch on octahedral tilts. In their simulations, zero tilt angles were imposed in one perovskite units within an elongated simulated cell. The two materials they investigated were $La_{0.75}Sr_{0.25}MnO_3$ (LSMO) and $SrRuO_3$, which have $a^-a^-a^-$ and $a^-a^-a^+$ tilt configurations respectively. It was found that the former can sustain the tilt reduction from the vertical interface, while disruptions in the latter are quickly reduced. These results are consistent with the findings here, but He et al. attributed the difference to other factors such as magnetic anisotropy and Jahn-Teller activity. Rondinelli et al. [220] showed the $a^0a^0c^-$ tilt in STO can propagate into $SrFeO_3$ in $STO/SrFeO_3$ superlattices. The conventional way to explore the potential energy landscape of tilted perovskite phases is to obtain the distortion modes using phonon calculations or group theory analysis [241], and then compute the potential energy as function of the amplitude [220, 242]. However, distorted structures generated this way may deviate from the valleys on the potential energy surface. On the other hand, the constrained optimisation approach allows the structure to follow the energy landscape. As a result, the energy versus displacement curves given here are usually flatter compared with those reported in literature [220, 243, 244].

In summary, first-principles calculations are used to reveal the response of octahedral networks under corner displacements that mimic an ideal interface between two perovskite

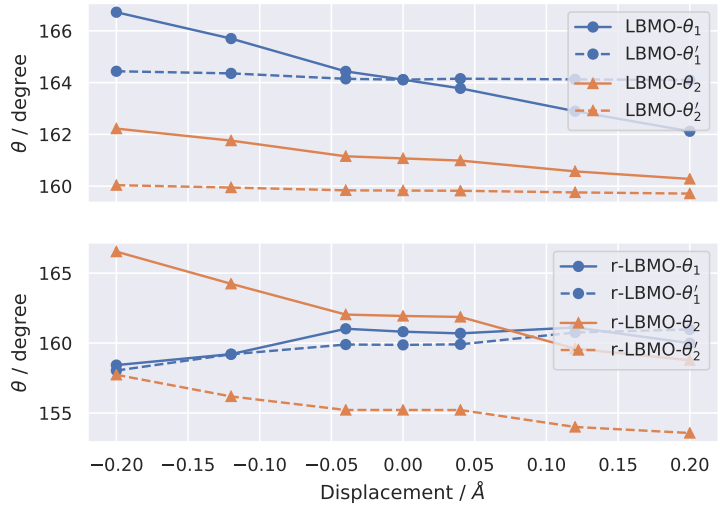

Fig. 7.23 Mn-O-Mn angles of (r)-LBMO with doubled cell sizes along c. The angles marked with "′" are further away form the LaO plane where the anion displacements are applied.

structured materials. It is found that the tilted octahedra in *Pnma* structured LBMO are not susceptible to pinning effects originating from interfaces, owing to the lack of mechanisms for compensating changes in tilt angles. In contrast, the $R\bar{3}c$ phase with $a^-a^-a^-$ tilt configuration is susceptible to tilt suppression, as changes in tilt along the two pseudo-cubic axes parallel to the interface plane can be compensated by that along the third axis. These results suggest the experimentally observed the tilt angle suppressions at LBMO/STO interfaces were likely to be accompanied by a change of the octahedral tilt from $a^-a^-a^+$ to $a^-a^-a^-$.

7.6 Octahedral rigidity of other perovskites

The rigidity of octahedral networks in other perovskites can be studied using the same method described in the previous section. Knowing how flexible the octahedral networks are would help to establish design principles for interfaces exploiting the octahedral proximity effects. Using $CaTiO_3$ as a model system, it is find that the relative energy changes ΔE are relatively insensitive to convergence related parameters such as the plane wave cut-off energy, k-space sampling, and FFT grid. In addition, the response curves computed for $LaMnO_3$ using a range of U and magnetic orderings differ only slightly. This can be attributed to the interaction between atoms being predominately ionic.

The energy curves for a range of other perovskites are shown in Fig. 7.24. Among these materials, $LaMnO_3$ has a relatively hard octahedral network. The energy changes

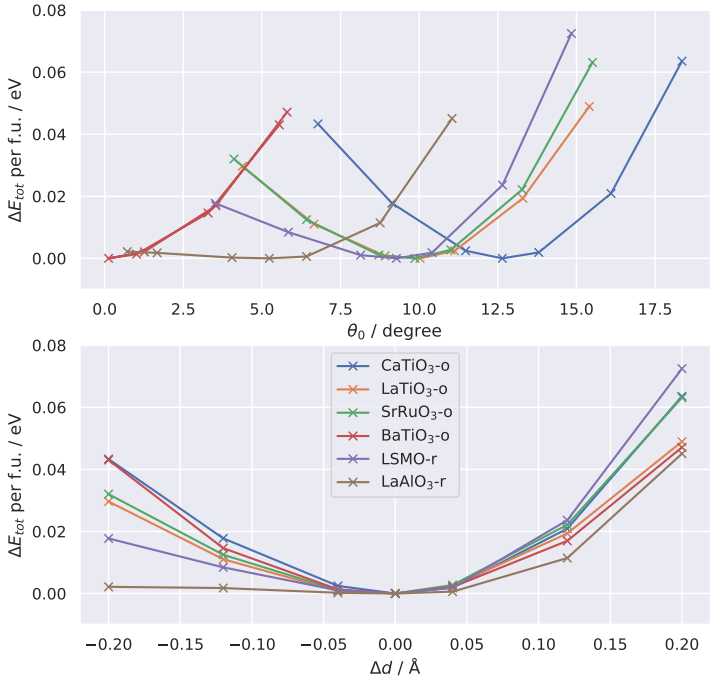

Fig. 7.24 Response curves for a range of other perovskites.

after applying $+0.2$ Å and -0.2 Å corner displacements (Δd) are compared in Fig. 7.25. Materials with $a^-a^-a^-$ rotation patterns, such as $LaAlO_3$ and $La_{0.67}Sr_{0.33}MnO_3$ are found to be susceptible to such displacements, in accordance with the findings in the previous section. Notably, $BaTiO_3$ has a relatively hard octahedral network and with zero tilt angle if not perturbed, which can be related to it having a tolerance factor greater than one. This makes $BaTiO_3$ a good buffer layer for enhancing tilt suppression, although the effects of Ti displacements, i.e. ferroelectric distortions, are neglected here.

Epitaxial films are often strained. One of the advantages of LBMO is the relatively small interface strain when deposited onto STO substrates. It is known that the strain induced by epitaxial interfaces affects the stability of perovskite phases in a range of materials including $LaAlO_3$ [245], $BiFeO_3$ [246], $LaNiO_3$ [247], and $SrRuO_3$ [248]. On the other hand, little is known about how strain affects the rigidity of octahedral networks.

The responses to corner perturbations can be computed with strained perovskite structures in an analogous manner to that described earlier. To simulate the substrate clamping effect, the in-plane cell vectors are enforced to form a square lattice, and they are constrained during

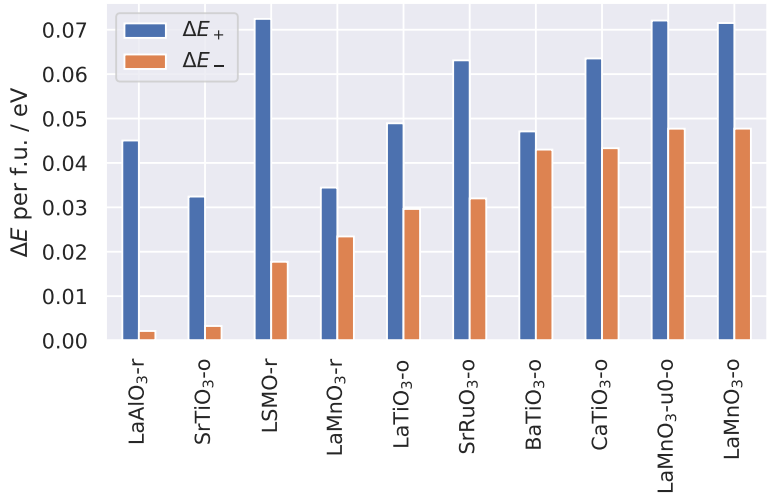

Fig. 7.25 Energy changes per formula unit under $+0.2$ Å (ΔE_+) and -0.2 Å (ΔE_-) vertex displacements for a range of perovskites. o- $a^-a^-c^+$ rotation pattern; r-$a^-a^-c^-$ rotation pattern.

the initial relaxation, and the resulting relaxed structures are subsequently used for creating perturbed frames.

The responses of $LaMnO_3$ (FM) to perturbations under biaxial strain are shown in Fig. 7.26. The tensile strain reduces the tilt angles in the relaxed structures. However, the rigidity remains almost unchanged by the strain, as show by the overlapping response curves in the upper panel. Different behaviour is observed for $LaAlO_3$, which has $a^-a^-a^-$ tilt. In Fig. 7.27, the energy cost for increasing the tilt angle is increased by compressive strain, and tensile train makes the networks less susceptible to tilt suppression. The negative energy differences (ΔE_{tot}) can be explained by the $R\bar{3}c$ phase[†] becoming unstable when compressively strained, and a competing $I4/mcm$ phase with $a^0a^0a^-$ tilts emerges [245].

[†]The actual space group symmetry is $C2/c$ after imposing square lattice.

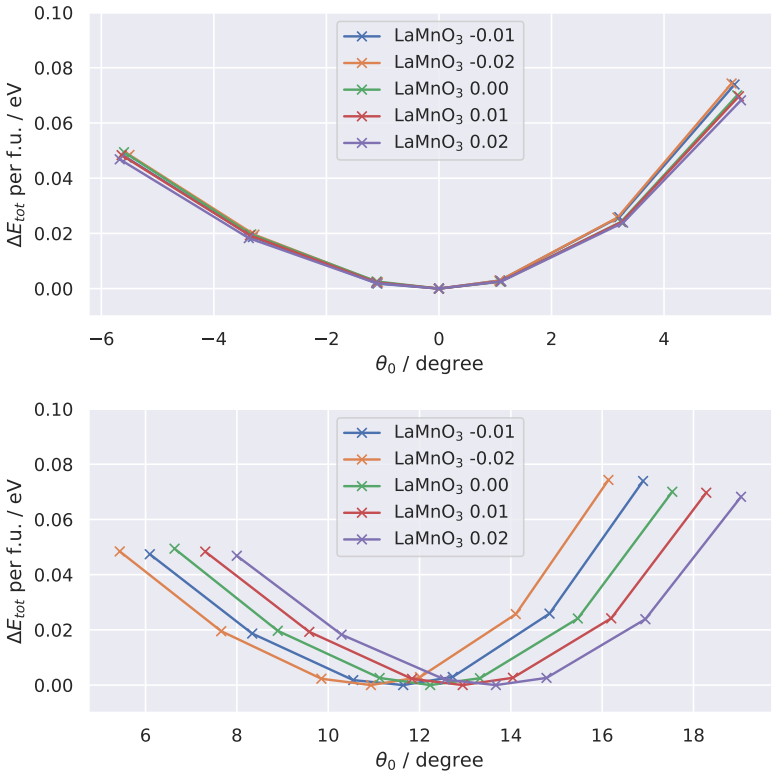

Fig. 7.26 The response of $LaMnO_3$ to perturbations under biaxial strain.

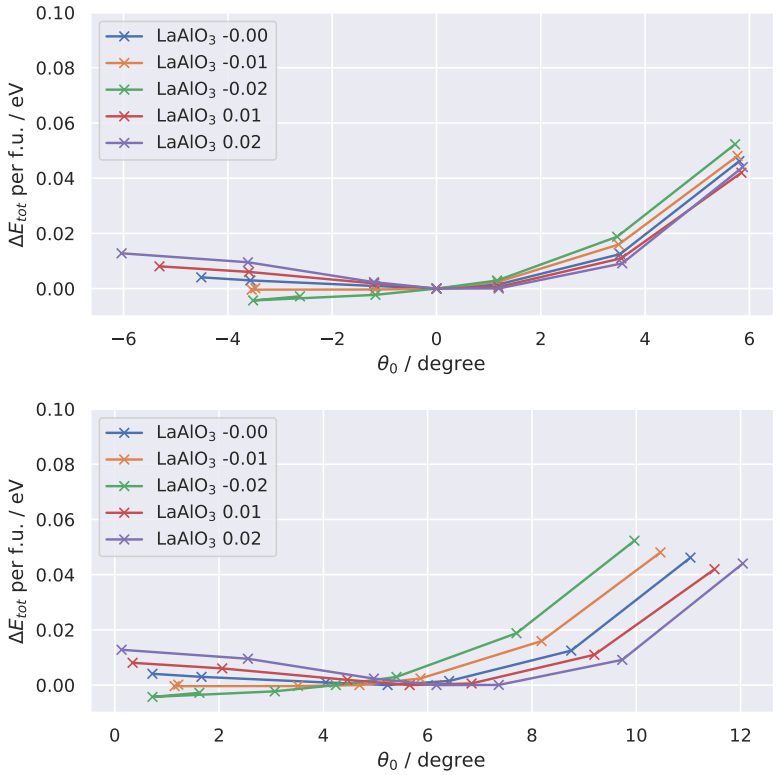

Fig. 7.27 The response of $LaAlO_3$ to perturbations under biaxial strain.

7.7 Conclusion and further work

The mode and magnitude of octahedral tilting can have significant effects on the functional properties of perovskite structured oxide materials. Motivated by the appearance and disappearance of ferromagnetic insulating properties in LBMO/STO bilayer/superlattice films, the effects of interfaces on the lattice and the electronic structure are investigated using first-principles calculations. Some experimental observations are successfully accounted for, such as interface charge transfer and associated ferromagnetism of interfacial Ti atoms. The rigidity of octahedral networks is quantified by exploring the energy landscapes of perovskite structures under corner distortions that mimics octahedral coupling at interfaces. An alternative rhombohedral LBMO phase with $a^-a^-a^-$ tilt configuration is shown to be more stable when corners of octahedra are being pinned. The bulk orthorhombic phase with $a^-a^-a^+$ tilt is very resistant to corner displacements. The flexibility of the octahedral network in $a^-a^-a^-$ tilt configuration can be attributed to the existence of a compensation mechanism.

The method developed for studying octahedral network rigidity can be applied to many other perovskites. More comprehensive studies of the general rules behind tilt suppression are beneficial for designing interfaces that can better exploit the octahedral proximity effects. Other factors such as radii of the ions and covalent B-O bonding, are also worth studying. Many perovskites have transitions from low to high symmetry phases with increasing temperature, which is also likely to affect the rigidity of the octahedral networks.

Chapter 8

Other works

8.1 Interface strain in high temperature superconductors

The work described below has been published in Refs [69, 249]. I performed the analyses of the STEM images in order to understand the interface strain in the nanostructured films, which helped to explain the enhanced superconducting T_c. Here, only key findings related to my contributions are described.

Superconducting cuprates have attracted a tremendous amount of research interest since the discovery of high temperature superconductivity in yttrium barium copper oxide (YBCO) [250]. Unlike the conventional superconductors, where the origin of superconductivity is well described by the BCS theory [251], there are few theoretical frameworks for predicting superconducting transition temperatures (T_c) for high temperature superconductors (type-II superconductors). However, phenomenological theories can still be established, and it has been proposed that the T_c is strongly affected by the number of connected CuO layers in the crystal lattice, as well as the in-plane and out-of-plane Cu-O distances [252].

Vertically aligned nanocomposites, described in Sec. 2.3, allow independent control of out-of-plane lattice constants through vertical interfaces. VANs consist of a $LaCuO_3$ matrix and $La_2Cu_1O_{4+\delta}$ (214) pillars were fabricated by Dr Eun-Mi Choi, who also characterised these films in collaboration with other researches. Some VAN films were found to be superconducting with a $T_c = 50$ K, which is higher that of conventional planar 214 films ($T_c = 35$ K). More intriguingly, magnetic measurements showed superconductivity with a T_c of 120 K, but the same was not found with the transport measurements.

The data obtained using atomic force microscopy and scanning transmission electron microscopy suggest the composite films consist of orthogonally arranged elongated grains of 214 whose c axis is in the out-of-plane direction. The structure of La_2CuO_4 can be found in

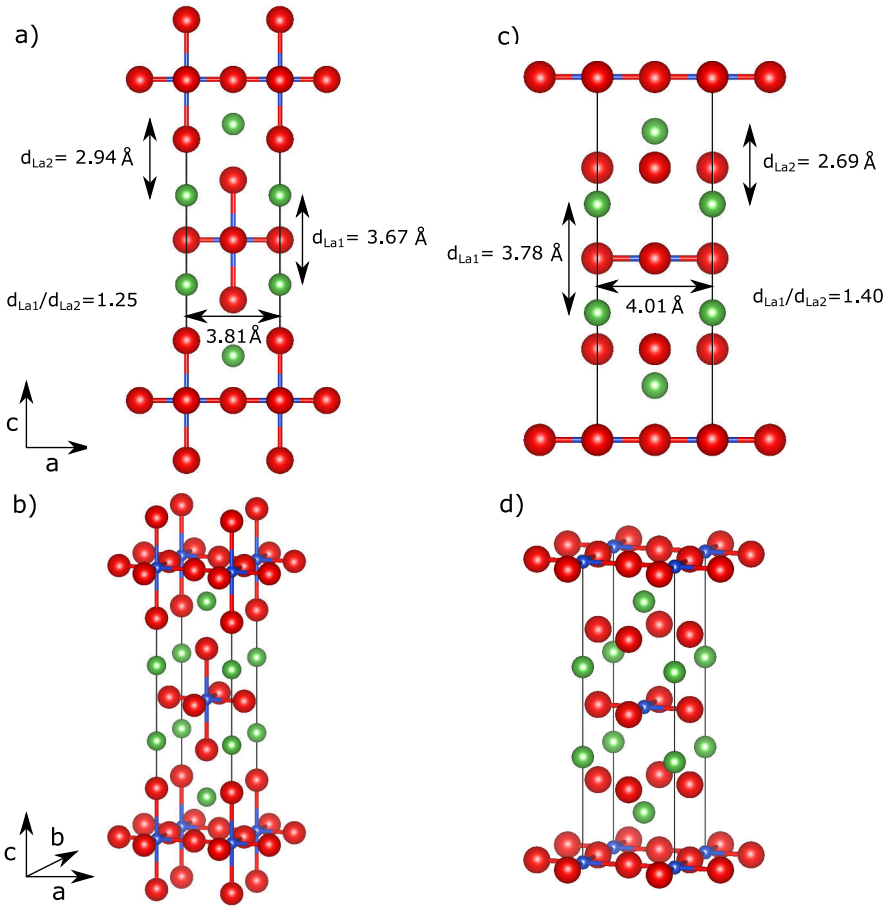

Fig. 8.1 Structures of the T (a.b) and T′ (c,d) phases of La_2CuO_4.

Fig. 8.1a&b. These grains are embedded in a matrix made of $LaCuO_3$. Alternatively oriented 214 grains that have the c axis along the in-plane directions (a-214) are found at some vertical interfaces (Fig. 8.3a).

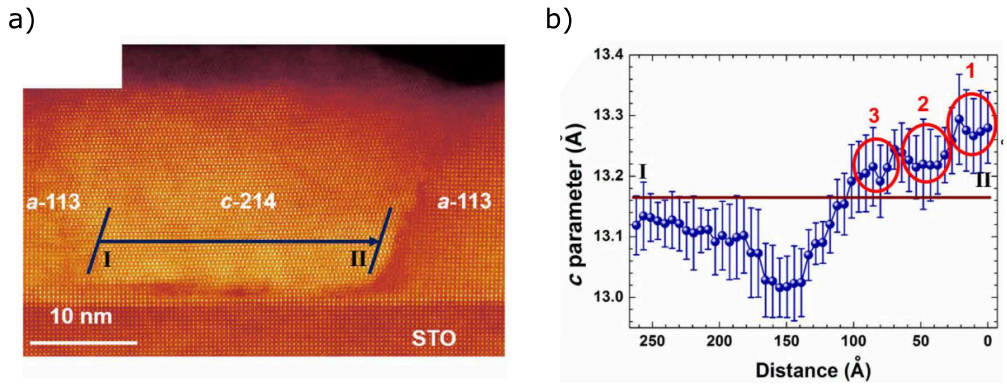

Fig. 8.2 a) The cross-sectional STEM-HAADF image of the c-214 grain. b) The c lattice parameter increases near the vertical interface, highlighted by the red circles. Adapted from Ref [249] (Licensed under CC BY 4.0).

The STEM-HAADF images are analysed to reveal the strain and distortions inside the films. Positions of the atomic columns are systematically extracted and refined using 2D Gaussian fitting, based on the routines provided by the open source software `atomap` [253]. Maps of lattice constants and La-La distances are produced using the extracted atomic positions. In conventional planar epitaxial films, the strain state is controlled by the substrate, but the same is not true in VANs. The line-averaged c and a lattice constants inside the c-214 grain are displayed in Fig. 8.2. The increase of the c lattice constant close to the vertical interface, highlighted by the three red circles, shows that the tensile strain is caused by the vertical interfaces. The apical Cu-O distance should also increase with increasing c*, which can be related to the increased T_c.

Another important finding is that the a-214 grain (Fig. 8.3a) is in fact made of a non-superconducting T' phase, where each Cu-O plane are separated by fluorite structured LaO blocks [254]. Although the oxygen atoms are not visible in the HAADF images, the T′ phase have a different ratio between the two non-equivalent La-La plane distances ($d_{La1}/d_{La2} = 1.40$), as shown in Fig. 8.1a&c, allowing it to be identified. In Fig. 8.3a, a coherent 45° interface can be seen between the c-214 and the a-214. The perovskite blocks in 214 is anisotropic, but at this interface both a-214 and c-214 share the common perovskite-

*This assumption is consistent with experimental data, and its validity using is also checked using DFT calculations.

like blocks, which gives rise to increased La-La distances and apical Cu-O distances in c-214. The greatly increased T_c of 120 K may be attributed to the highly distorted structure at the a-214/c-214 interface. Because a-214 grains only nucleate after a few layers of c-214 have been deposited, these interfaces do not contact the substrate. Hence, transport measurements were not able to confirm the 120 K superconductivity.

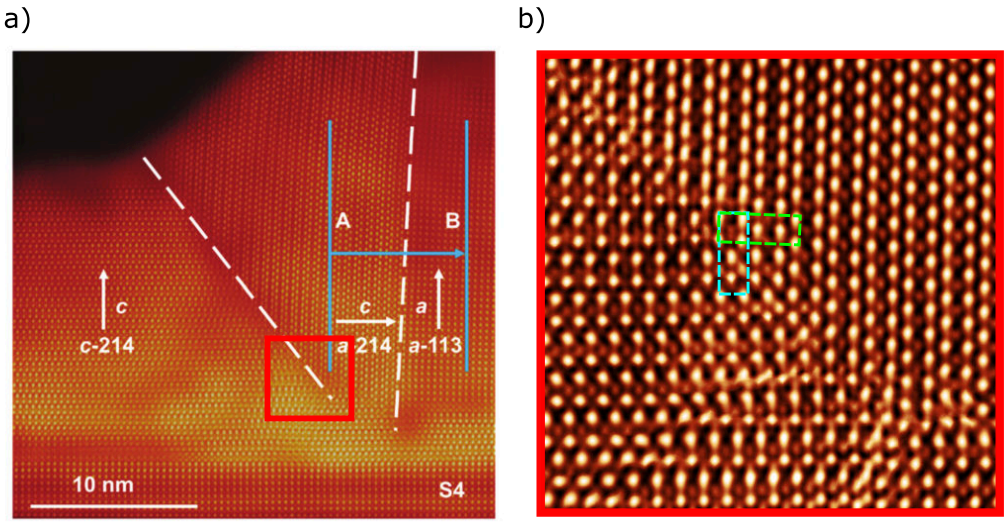

Fig. 8.3 a) The cross-sectional STEM-HAADF image showing c-214 (left) a-214 (middle) and $LaCuO_3$ (right) grains. Reproduced from Ref [69] with permission from The Royal Society of Chemistry. b) A zoom-in of the interface region showing the a-214 (green) and c-214 (cyan) unit cells.

8.2 Code development

Several software packages are developed during the PhD research. A brief description is given for each of them in this section.

8.2.1 `aiida-castep` - a plugin to interface CASTEP with AiiDA for workflow automation

Scientific research should be reproducible. This can be fulfilled easily, in principles, when conducting computational studies, since executions of computer programs are inherently deterministic. In principle, the result of a single calculation can always be reproduced with the exact same input. Unfortunately, it is rarely the case that performing a single calculation

is sufficient for scientific discoveries. For example, when studying the band structure of a material, the crystal structure needs to be optimised first, followed by a self-consistent calculation to obtain the charge density, and then a non-self-consistent calculation should be performed to get the Kohn-Sham eigenvalues along specific paths in the reciprocal space. To study the response of the band structure under external forces, the ionic structure may undergo constrained geometry optimisation starting from deformed geometries that are based on the relaxed structure. Whilst the reproducibility of each calculation can be guaranteed by simply saving their input and output as files, it is not easy to keep track of the relationships among chains and/or branches of calculations.

The Automated Interactive Infrastructure and Database for Computational Science (AiiDA) [255, 256] is a platform for running automated, high-throughput calculations with the focus of preserving the provenance relationships among them. This is achieved by storing all information on a directed acyclic graph. The input and output of each *process* and the *process* itself are stored as nodes in the graph, and they are connected with links satisfying a set of rules that ensure the integrity. The word *process* refers to anything that generates or returns new data, such as lengthy computations ran on remote computers, local manipulations of the data, and high-level workflows. Consequently, the exact history of any result can be traced all the way back. It also provides a daemon for automated job submission, monitoring, retrieval, and parsing output files. The database is stored on the local computer, and no specialised configurations are needed on the remote cluster.

The AiiDA framework is designed to be extendable with plugins. The `aiida-core` package is general and not locked-in with any specific codes. The `aiida-castep` package has been developed to interface AiiDA with CASTEP. Writers and parsers are implemented to work with input and output files of CASTEP. More importantly, it defines how CASTEP calculations are incorporated into the acyclic graph. In Fig. 8.4, the immediate input and output nodes of a CASTEP calculation are displayed. The input nodes include data such as the input parameters, a pointer to the exact binary executable stored on the remote computer, and in this case a `RemoteData`, which is the output of a previous calculation. The links between nodes are annotated by their types and labels. The `INPUT_CALC` link relates this calculation to the workflow `CastepBaseWorkChain`, which launches this calculation and checks for errors when it finishes. It allows a few common errors, such as electron convergence failure and wall-time limits being reached, to be mediated through resubmission with revised settings. Each node has a universal identifier, part of which is displayed the brackets in Fig. 8.4. This allows it to be uniquely referenced in subsequent data analysis.

Fig. 8.5 shows the ancestors and descents of the calculation (yellow coloured), up to a depth of three generations. The provenance graph can appear complex even with a simple

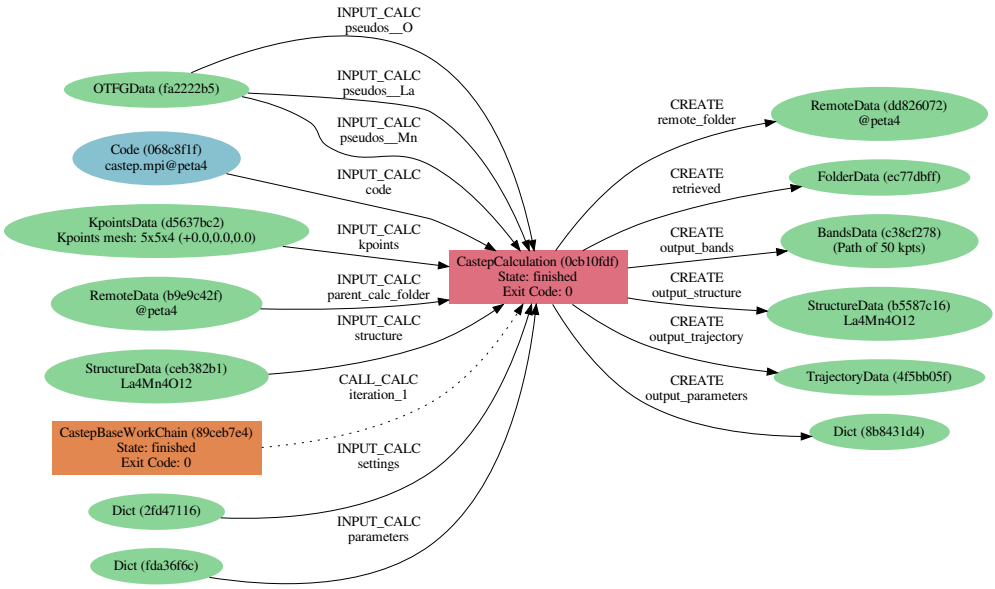

Fig. 8.4 The provenance graph of a single CASTEP calculation including only the immediate input and output nodes.

chain of geometry optimisation, because all information are included. The AiiDA framework provides tools to transverse the graph and extract data along the way. For example, the trajectory of a multi-step geometry optimisation involving a chain of restarted/continued calculations can be obtained by locating the ancestral calculations following the path connecting their output/input structures.

The `aiida-castep` plugin also ships with basic workflows for performing geometry optimisations, which automatically submit continuation jobs if the current calculation fails to fully relax the ionic structure, or it is terminated due to wall-time limit. They can be used as building blocks for more complex workflows. The study of octahedral network rigidity presented in Chapter 7 is automated using these infrastructures. A few helper functions are also implemented in `aiida-castep`. The input parameters of CASTEP are always checked to prevent erroneous calculations being submitted to the remote computer. Local dry runs can be performed for estimating memory requirements and finding the optimum parallelisation strategy.

AiiDA (`aiida-core`) is an open source software released under the MIT License. I also contributed code to `aiida-core` and participated workshops organised by its developers. The `aiida-castep` plugin is open source and released under the MIT License. Home page: https://github.com/zhubonan/aiida-castep.

8.2.2 Other computer codes developed

Descriptions are given below for a few other computer codes developed during my research.

`castepinput` is a python tool for working with input files of CASTEP. Atomic Simulation Environment (ASE) can also prepare CASTEP input files, but it is tightly integrated with its own `Atoms` object-orientated interface. `castepinput` is designed to be light-weight and has fewer dependencies. The code is open source and released under the MIT license. It is one of the dependencies of `aiida-castep`. Home page: https://github.com/zhubonan/castepinput.

`airsspy` is a python tool for programmatically generating the input files used by the open source *Ab initio* Random Structure Searching (AIRSS) package [181]. It extends ASE and allows per-site randomisation tags to be set using an object-orientated interface, which is particularly useful for setting up interfaces searches (Chapters 5 and 6). The code is open source and released under the GPL V2.0 license. Home page: https://github.com/zhubonan/airsspy.

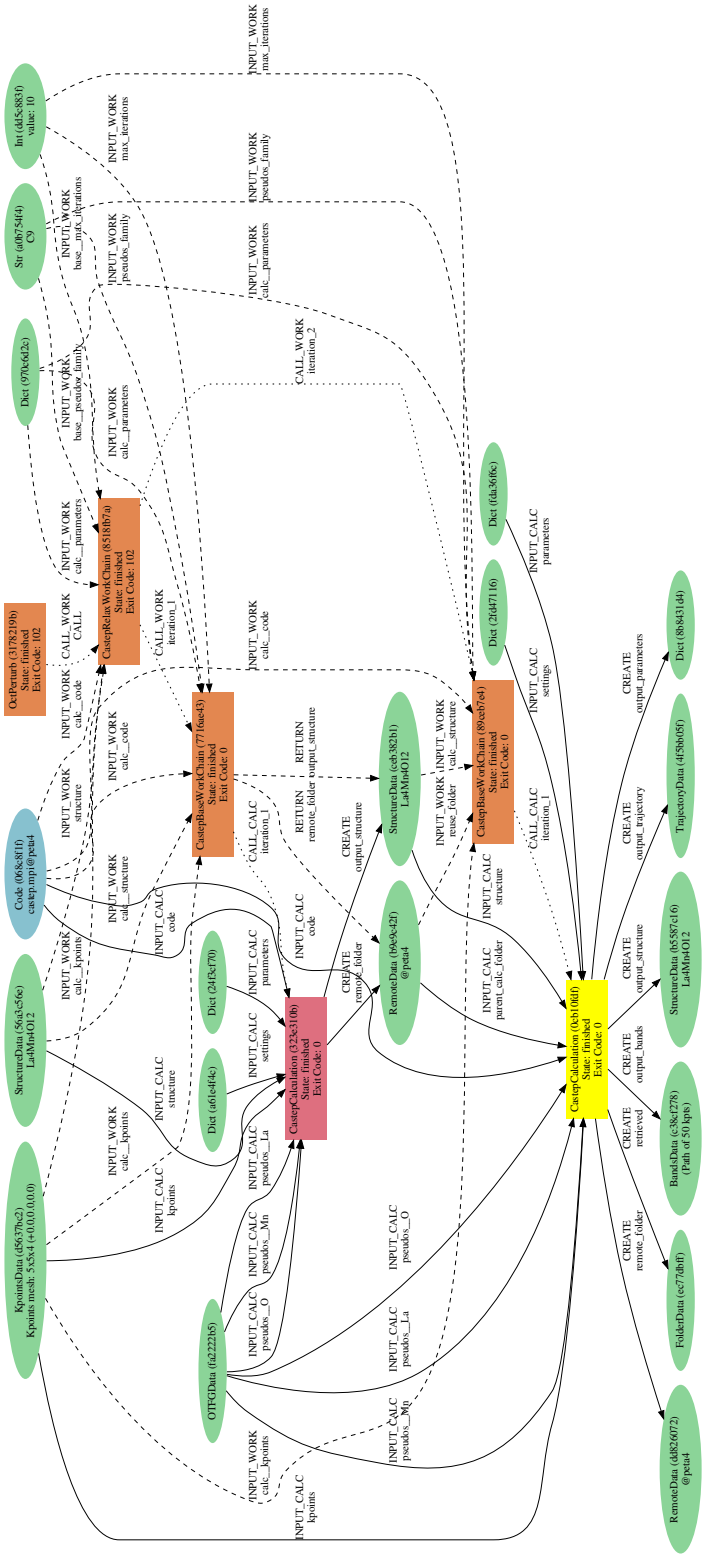

Fig. 8.5 The provenance graph of the CASTEP calculation (coloured yellow) as in Fig. 8.4, but includes ancestors up to a depth of three levels.

`airssff` is an alternative driver package for performing random structure searching, written in python. It uses ad-hoc per-search database for dynamically allocating jobs to a pool of workers, and allows automatic scheduler-aware continuation/checkpointing. These functionalities are essential for interface searches, as the geometry optimisations often exceed the wall time limit set by the scheduler of the remote cluster. An object-oriented design allows individual searches to be customised easily, which comes in handy when developing and testing search protocols.

A list of other software packages used in this project can be found in Appendix A.2.

Chapter 9

Conclusions and outlook

Interfaces in oxide thin films play important roles in tuning properties and inducing novel and emergent functionalities. Computational approaches are ideal for studying interfaces, as the effects of constituent bulk phases can be excluded easily, which can be difficult to achieve in experiment. However, very often the exact atomic structures of the interfaces, which are the essential input for computational studies, are unknown in the first place. As a result, most existing computational studies are limited to the interfaces between materials with the same crystal structure, or those already well characterised experimentally.

In this thesis, this problem is tackled by using random structure searching to predict the interface structures. This enables us to investigate interfaces that are formed between materials with different structures. The oxygen ionic conductivity in oxides is highly sensitive to the underlying crystal structures, and interfaces are like to affect the ionic conductivity. In Chapter 5, structures of the interfaces in ionic conducting STO/CeO_2 vertically aligned nanocomposites (VANs) are determined. The majority STO(100)/CeO_2(110) interfaces are found to have highly distorted anion lattices, and the resulting complex energy landscapes for oxygen vacancies migration suggest these interfaces are unlikely to directly enhance the ionic conductivity. On the other hand, a parallel O^{17} solid-state NMR study by our collaborators have found chemical shifts corresponding to interface environments, and the change of signal strength with enrichment temperature suggests interfaces do give rise to faster ionic conduction. Results of the first-principles NMR calculations reveal that the observed signals are not from the majority STO(100)//CeO_2(110) interfaces initially studied; instead, they are consistent with that of the minority STO(110)/CeO_2(100) interfaces.

The fluorite-perovskite interfaces have attracted much research attention over the last decade, since the controversial report of colossally enhanced ionic conductivity in YSZ/STO heterostructures [11]. In Chapter 6, the planar epitaxial (001) interfaces between CeO_2 and STO are studied. Stable interface structures are obtained by performing first-principles

searches including a range of terminations and local stoichiometries. The SrO terminated interface contains a partially occupied anion lattice, which allows oxygen anions to diffuse laterally, as found in the molecular dynamics simulations. This study suggests a new route for enhancing ionic conductivity by exploiting interface reconstruction.

In Chapter 7, the perovskite-perovskite interfaces formed between $La_{0.9}Ba_{0.1}MnO_3$ (LBMO) and STO are studied in collaboration with experimental investigations. LBMO is a bulk ferromagnetic insulator, which makes it ideal for spintronics applications. However, when deposited as thin films, its properties are strongly controlled by the octahedral proximity effects at the interfaces. Because STO and LBMO both have perovskite structures, interface models were constructed by hand and subsequently optimised. While some experimental findings, such as the emerging ferromagnetism from Ti atoms, can be accounted for, much weaker octahedral tilt suppressions are predicted by the calculations. The subsequent studies about the rigidity of the relevant octahedral networks suggests a competing LBMO phase with an octahedral network that is more flexible can be stabilised as a result of the interface proximity effects.

The studies present in this thesis highlight the importance of reliable computational predictions about atomic structures of interfaces, and random structure searching has been shown to be a valuable tool for resolving complex reconstructions at interfaces. In Chapter 7, the perovskite-perovskite interfaces that are initially thought to be structurally trivial are in fact rather complex. This shows that the stabilities of the constituent bulk phases should not be overlooked in interface studies. Experimental knowledge of the system is also important, as they can greatly benefit computational studies by limiting the search space, and ultimately the predictions have to be tested with the reality. Care should be taken not to over-interpret the experimental data though. In Chapter 5, the minor interfaces are not included in the searching initially, and in Chapter 7 the hand-built interface models do not take account the existence of different bulk phases. These choices were motivated by the prior experimental information, with which the alternatives are also consistent.

Computational studies of interface can be challenging due to their diversity and complexity, but there are also plenty of opportunities and interesting topics worth investigating. Some directions emerged during the PhD study are listed below.

First, in Chapter 5, only a preliminary study has been carried out for the minority STO(110)/CeO_2(100) interfaces, and there are still questions regarding the exact stoichiometry of these interfaces. A comprehensive investigation of their structures under a range of local oxygen concentrations would certainly help explain the cause of the enhanced oxygen diffusivity.

Secondly, the applicability of interatomic potentials at interfaces needs be thoroughly investigated. Because they are fitted to specific properties of the bulk phases, there is no guarantee that they behave well at interfaces. In Chapter 6, it is shown that the transition state barriers are systematically overestimated by the interatomic potentials. More transferable potentials that work at both bulk and interface environments are needed for studying systems that are too large for DFT calculations. An alternative is to explore hybrid quantum mechanics/molecular mechanics (QM/MM) approaches, where only the interface regions of the interest are treated with first-principles methods.

Lastly, the octahedral networks in only a few perovskites are studied in Chapter 7. The protocol developed, which involves explicitly perturbing octahedral corners, provides a practical way for exploring the energy landscapes associated with complex distortions in perovskites. Future studies should make the displacements of the corners span the *xy* plane, instead of being limited to be on a single line. The investigations about the strain and doping effects can be applied to other perovskites such as $La_{0.67}Sr_{0.33}O_3$ and $SrRuO_3$. Future studies of these topics will certainly help establish the design principles of perovskite interfaces to fully exploit the octahedral proximity effects.

References

[1] P. R. Willmott. Deposition of complex multielemental thin films. *Progress in Surface Science*, 76(6):163–217, October 2004.

[2] Lior Kornblum. Conductive Oxide Interfaces for Field Effect Devices. *Advanced Materials Interfaces*, 6(15):1900480, August 2019.

[3] Herbert Kroemer. Heterostructure Devices: A Device Physicist Looks at Interfaces. In Giorgio Margaritondo, editor, *Electronic Structure of Semiconductor Heterojunctions*, Perspectives in Condensed Matter Physics, pages 116–149. Springer Netherlands, Dordrecht, 1988.

[4] J. Chakhalian, A. J. Millis, and J. Rondinelli. Whither the oxide interface. *Nature Materials*, 11(2):92–94, February 2012.

[5] H. Y. Hwang, Y. Iwasa, M. Kawasaki, B. Keimer, N. Nagaosa, and Y. Tokura. Emergent phenomena at oxide interfaces. *Nature Materials*, 11(2):103–113, February 2012.

[6] A. Ohtomo and H. Y. Hwang. A high-mobility electron gas at the LaAlO3/SrTiO3 heterointerface. *Nature*, 427(6973):423–426, January 2004.

[7] J. Chakhalian, J. W. Freeland, G. Srajer, J. Strempfer, G. Khaliullin, J. C. Cezar, T. Charlton, R. Dalgliesh, C. Bernhard, G. Cristiani, H.-U. Habermeier, and B. Keimer. Magnetism at the interface between ferromagnetic and superconducting oxides. *Nature Physics*, 2(4):244–248, April 2006.

[8] Karen Michaeli, Andrew C. Potter, and Patrick A. Lee. Superconducting and ferromagnetic phases in $SrTiO_3/LaAlO_3$ oxide interface structures: Possibility of finite momentum pairing. *Physical Review Letters*, 108(11):117003, March 2012.

[9] Eric Bousquet, Matthew Dawber, Nicolas Stucki, Céline Lichtensteiger, Patrick Hermet, Stefano Gariglio, Jean-Marc Triscone, and Philippe Ghosez. Improper ferroelectricity in perovskite oxide artificial superlattices. *Nature*, 452(7188):732–736, April 2008.

[10] A. Brinkman, M. Huijben, M. van Zalk, J. Huijben, U. Zeitler, J. C. Maan, W. G. van der Wiel, G. Rijnders, D. H. A. Blank, and H. Hilgenkamp. Magnetic effects at the interface between non-magnetic oxides. *Nature Materials*, 6(7):493–496, July 2007.

[11] J. Garcia-Barriocanal, A. Rivera-Calzada, M. Varela, Z. Sefrioui, E. Iborra, C. Leon, S. J. Pennycook, and J. Santamaria. Colossal Ionic Conductivity at Interfaces of Epitaxial ZrO2:Y2O3/SrTiO3 Heterostructures. *Science*, 321(5889):676–680, August 2008.

[12] Emiliana Fabbri, Daniele Pergolesi, and Enrico Traversa. Ionic conductivity in oxide heterostructures: The role of interfaces. *Science and Technology of Advanced Materials*, 11(5):054503, 2010.

[13] Satoshi Okamoto, Andrew J. Millis, and Nicola A. Spaldin. Lattice relaxation in oxide heterostructures: LaTiO3/SrTiO3 superlattices. *Physical Review Letters*, 97(5):056802, August 2006.

[14] Alexey Kalabukhov, Robert Gunnarsson, Johan Börjesson, Eva Olsson, Tord Claeson, and Dag Winkler. Effect of oxygen vacancies in the $SrTiO_3$ substrate on the electrical properties of the $LaAlO_3/SrTiO_3$ interface. *Physical Review B*, 75(12):121404, March 2007.

[15] Zoran S. Popović, Sashi Satpathy, and Richard M. Martin. Origin of the two-dimensional electron gas carrier density at the $LaAlO_3$ on $SrTiO_3$ interface. *Physical Review Letters*, 101(25):256801, December 2008.

[16] Naoyuki Nakagawa, Harold Y. Hwang, and David A. Muller. Why some interfaces cannot be sharp. *Nature Materials*, 5(3):204–209, March 2006.

[17] Z. Q. Liu, C. J. Li, W. M. Lü, X. H. Huang, Z. Huang, S. W. Zeng, X. P. Qiu, L. S. Huang, A. Annadi, J. S. Chen, J. M. D. Coey, T. Venkatesan, and Ariando. Origin of the Two-Dimensional Electron Gas at LaAlO 3 / SrTiO 3 Interfaces: The Role of Oxygen Vacancies and Electronic Reconstruction. *Physical Review X*, 3(2):021010–021010, May 2013.

[18] N. C. Bristowe, Philippe Ghosez, P. B. Littlewood, and Emilio Artacho. Origin of two-dimensional electron gases at oxide interfaces: Insights from theory. *Journal of Physics: Condensed Matter*, 26(14):143201, April 2014.

[19] M. P. Warusawithana, C. Richter, J. A. Mundy, P. Roy, J. Ludwig, S. Paetel, T. Heeg, A. A. Pawlicki, L. F. Kourkoutis, M. Zheng, M. Lee, B. Mulcahy, W. Zander, Y. Zhu, J. Schubert, J. N. Eckstein, D. A. Muller, C. Stephen Hellberg, J. Mannhart, and D. G. Schlom. LaAlO3 stoichiometry is key to electron liquid formation at LaAlO3/SrTiO3 interfaces. *Nature Communications*, 4:2351, August 2013.

[20] A. Ohtomo, D. A. Muller, J. L. Grazul, and H. Y. Hwang. Artificial charge-modulationin atomic-scale perovskite titanate superlattices. *Nature*, 419(6905):378–380, September 2002.

[21] J. Chakhalian, J. W. Freeland, H.-U. Habermeier, G. Cristiani, G. Khaliullin, M. van Veenendaal, and B. Keimer. Orbital Reconstruction and Covalent Bonding at an Oxide Interface. *Science*, 318(5853):1114–1117, November 2007.

[22] Artem R. Oganov, Chris J. Pickard, Qiang Zhu, and Richard J. Needs. Structure prediction drives materials discovery. *Nature Reviews Materials*, 4(5):331, May 2019.

[23] Chris J. Pickard, Ion Errea, and Mikhail I. Eremets. Superconducting Hydrides Under Pressure. *Annual Review of Condensed Matter Physics*, 11(1):null, 2020.

[24] Alexander G. Kvashnin, Zahed Allahyari, and Artem R. Oganov. Computational discovery of hard and superhard materials. *Journal of Applied Physics*, 126(4):040901, July 2019.

[25] M. R. Palacín and A. de Guibert. Why do batteries fail? *Science*, 351(6273), February 2016.

[26] Eric D. Wachsman and Kang Taek Lee. Lowering the Temperature of Solid Oxide Fuel Cells. *Science*, 334(6058):935–939, November 2011.

[27] Chengxiang Wang, Longwei Yin, Luyuan Zhang, Dong Xiang, and Rui Gao. Metal Oxide Gas Sensors: Sensitivity and Influencing Factors. *Sensors (Basel, Switzerland)*, 10(3):2088–2106, March 2010.

[28] Tao Wan, Lepeng Zhang, Haiwei Du, Xi Lin, Bo Qu, Haolan Xu, Sean Li, and Dewei Chu. Recent Developments in Oxide-Based Ionic Conductors: Bulk Materials, Nanoionics, and Their Memory Applications. *Critical Reviews in Solid State and Materials Sciences*, 43(1):47–82, January 2018.

[29] Andrea Cavallaro, Mónica Burriel, Jaume Roqueta, Alexandra Apostolidis, Alessandro Bernardi, Albert Tarancón, Rajagopalan Srinivasan, Stuart N. Cook, Hamish L. Fraser, John A. Kilner, David W. McComb, and José Santiso. Electronic nature of the enhanced conductivity in YSZ-STO multilayers deposited by PLD. *Solid State Ionics*, 181(13–14):592–601, May 2010.

[30] Xin Guo. Comment on "Colossal Ionic Conductivity at Interfaces of Epitaxial ZrO2:Y2O3/SrTiO3 Heterostructures". *Science*, 324(5926):465–465, April 2009.

[31] R. A. De Souza and A. H. H. Ramadan. Ionic conduction in the SrTiO3|YSZ|SrTiO3 heterostructure. *Physical Chemistry Chemical Physics*, 15(13):4505–4509, March 2013.

[32] Sang Mo Yang, Shinbuhm Lee, Jie Jian, Wenrui Zhang, Ping Lu, Quanxi Jia, Haiyan Wang, Tae Won Noh, Sergei V. Kalinin, and Judith L. MacManus-Driscoll. Strongly enhanced oxygen ion transport through samarium-doped CeO2 nanopillars in nanocomposite films. *Nature Communications*, 6, October 2015.

[33] Shinbuhm Lee, Wenrui Zhang, Fauzia Khatkhatay, Haiyan Wang, Quanxi Jia, and Judith L MacManus-Driscoll. Ionic Conductivity Increased by Two Orders of Magnitude in Micrometer-Thick Vertical Yttria-Stabilized ZrO2 Nanocomposite Films. *Nano letters*, 15(11):7362–9, November 2015.

[34] Judith L. MacManus-Driscoll. Self-Assembled Heteroepitaxial Oxide Nanocomposite Thin Film Structures: Designing Interface-Induced Functionality in Electronic Materials. *Advanced Functional Materials*, 20(13):2035–2045, July 2010.

[35] V. M. Goldschmidt. Die Gesetze der Krystallochemie. *Naturwissenschaften*, 14(21):477–485, May 1926.

[36] A. M. Glazer. The classification of tilted octahedra in perovskites. *Acta Crystallographica Section B: Structural Crystallography and Crystal Chemistry*, 28(11):3384–3392, November 1972.

[37] Martin Gajek, Manuel Bibes, Stéphane Fusil, Karim Bouzehouane, Josep Fontcuberta, Agnès Barthélémy, and Albert Fert. Tunnel junctions with multiferroic barriers. *Nature Materials*, 6(4):296–302, April 2007.

[38] Guo-Xing Miao, Martina Müller, and Jagadeesh S. Moodera. Magnetoresistance in Double Spin Filter Tunnel Junctions with Nonmagnetic Electrodes and its Unconventional Bias Dependence. *Physical Review Letters*, 102(7):076601, February 2009.

[39] V. A. Cherepanov, E. A. Filonova, V. I. Voronin, and I. F. Berger. Phase Equilibria in the LaCoO3–LaMnO3–BaCoOz–BaMnO3 System. *Journal of Solid State Chemistry*, 153(2):205–211, September 2000.

[40] B. Dabrowski, K. Rogacki, X. Xiong, P. W. Klamut, R. Dybzinski, J. Shaffer, and J. D. Jorgensen. Synthesis and properties of the vacancy-free $La_{1-x}Ba_xMnO_3$. *Physical Review B*, 58(5):2716–2723, August 1998.

[41] Weiwei Li, Josee E. Kleibeuker, Rui Wu, Kelvin H. L. Zhang, Chao Yun, and Judith L. MacManus-Driscoll. Insulating-to-conducting behavior and band profile across the La0.9Ba0.1MnO3/Nb:SrTiO3 epitaxial interface. *PHYSICAL REVIEW B*, 96(16), October 2017.

[42] Weiwei Li, Bonan Zhu, Qian He, Albina Y. Borisevich, Chao Yun, Rui Wu, Ping Lu, Zhimin Qi, Qiang Wang, Aiping Chen, Haiyan Wang, Stuart A. Cavill, Kelvin H. L. Zhang, and Judith L. MacManus-Driscoll. Interface Engineered Room-Temperature Ferromagnetic Insulating State in Ultrathin Manganite Films. *Advanced Science*, 7(1):1901606, 2020.

[43] Guus Rijnders and Dave H. A. Blank. Growth Kinetics During Pulsed Laser Deposition. In Robert Eason, editor, *Pulsed Laser Deposition of Thin Films*, pages 177–190. John Wiley & Sons, Inc., 2006.

[44] Douglas H. Lowndes, D. B. Geohegan, A. A. Puretzky, D. P. Norton, and C. M. Rouleau. Synthesis of Novel Thin-Film Materials by Pulsed Laser Deposition. *Science*, 273(5277):898–903, August 1996.

[45] David P. Norton. Pulsed Laser Deposition of Complex Materials: Progress Toward Applications. In Robert Eason, editor, *Pulsed Laser Deposition of Thin Films*, pages 1–31. John Wiley & Sons, Inc., 2006.

[46] R.M. Tromp and J.B. Hannon. Thermodynamics of nucleation and growth. *Surface Review and Letters*, 9(3-4):1565–1593, 2002.

[47] H. M. Christen and G. Eres. Recent advances in pulsed-laser deposition of complex oxides. *Journal of Physics: Condensed Matter*, 20(26):264005, June 2008.

[48] Ayahiko Ichimiya, Philip I. Cohen, and Philip I. Cohen. *Reflection High-Energy Electron Diffraction*. Cambridge University Press, December 2004.

[49] N. Sata, K. Eberman, K. Eberl, and J. Maier. Mesoscopic fast ion conduction in nanometre-scale planar heterostructures. *Nature*, 408(6815):946–949, December 2000.

[50] Carlos Leon, Jacobo Santamaria, and Bernard A. Boukamp. Oxide interfaces with enhanced ion conductivity. *MRS Bulletin*, 38(12):1056–1063, December 2013.

[51] T. J. Pennycook, M. P. Oxley, J. Garcia-Barriocanal, F. Y. Bruno, C. Leon, J. Santamaria, S. T. Pantelides, M. Varela, and S. J. Pennycook. Seeing oxygen disorder in YSZ/SrTiO3 colossal ionic conductor heterostructures using EELS. *The European Physical Journal Applied Physics*, 54(3):33507, June 2011.

[52] Bilge Yildiz. "Stretching" the energy landscape of oxides—Effects on electrocatalysis and diffusion. *MRS Bulletin*, 39(2):147–156, February 2014.

[53] Akihiro Kushima and Bilge Yildiz. Oxygen ion diffusivity in strained yttria stabilized zirconia: Where is the fastest strain? *Journal of Materials Chemistry*, 20(23):4809–4809, 2010.

[54] Roger A. De Souza, Amr Ramadan, and Stefanie Hörner. Modifying the barriers for oxygen-vacancy migration in fluorite-structured CeO2 electrolytes through strain: A computer simulation study. *Energy & Environmental Science*, 5(1):5445–5453, January 2012.

[55] Dilpuneet S. Aidhy, Bin Liu, Yanwen Zhang, and William J. Weber. Strain-Induced Phase and Oxygen-Vacancy Stability in Ionic Interfaces from First-Principles Calculations. *Journal of Physical Chemistry C*, 118(51):30139–30144, December 2014.

[56] Wei Li Cheah and Michael W. Finnis. Structure of multilayer ZrO2/SrTiO3. *Journal of Materials Science*, 47(4):1631–1640, February 2012.

[57] Timothy J. Pennycook, Matthew J. Beck, Kalman Varga, Maria Varela, Stephen J. Pennycook, and Sokrates T. Pantelides. Origin of Colossal Ionic Conductivity in Oxide Multilayers: Interface Induced Sublattice Disorder. *Physical Review Letters*, 104(11):115901, March 2010.

[58] Feng Li, Ruifeng Lu, Haiping Wu, Erjun Kan, Chuanyun Xiao, Kaiming Deng, and Don E. Ellis. The strain effect on colossal oxygen ionic conductivity in nanoscale zirconia electrolytes: A first-principles-based study. *Physical Chemistry Chemical Physics*, 15(8):2692–2697, 2013.

[59] M. Oka, H. Kamisaka, T. Fukumura, and T. Hasegawa. DFT-based ab initio MD simulation of the ionic conduction in doped ZrO2 systems under epitaxial strain. *Physical Chemistry Chemical Physics*, 17(43):29057–29063, October 2015.

[60] Matthew S. Dyer, George R. Darling, John B. Claridge, and Matthew J. Rosseinsky. Chemical Bonding and Atomic Structure in Y2O3:ZrO2-SrTiO3 Layered Heterostructures. *Angewandte Chemie International Edition*, 51(14):3418–3422, April 2012.

[61] Alvin L.-S. Chua, Nicole A. Benedek, Lin Chen, Mike W. Finnis, and Adrian P. Sutton. A genetic algorithm for predicting the structures of interfaces in multicomponent systems. *Nature Materials*, 9(5):418–422, May 2010.

[62] Satoshi Okamoto and Andrew J. Millis. Electronic reconstruction at an interface between a Mott insulator and a band insulator. *Nature*, 428(6983):630–633, April 2004.

[63] Wenrui Zhang, Ramamoorthy Ramesh, Judith L. MacManus-Driscoll, and Haiyan Wang. Multifunctional, self-assembled oxide nanocomposite thin films and devices. *MRS Bulletin*, 40(09):736–745, September 2015.

[64] Aiping Chen, Zhenxing Bi, Quanxi Jia, Judith L. MacManus-Driscoll, and Haiyan Wang. Microstructure, vertical strain control and tunable functionalities in self-assembled, vertically aligned nanocomposite thin films. *Acta Materialia*, 61(8):2783–2792, May 2013.

[65] Judith L. MacManus-Driscoll, Patrick Zerrer, Haiyan Wang, Hao Yang, Jongsik Yoon, Arnaud Fouchet, Rong Yu, Mark G. Blamire, and Quanxi Jia. Strain control and spontaneous phase ordering in vertical nanocomposite heteroepitaxial thin films. *Nature Materials*, 7(4):314–320, April 2008.

[66] H. Zheng, F. Straub, Q. Zhan, P.-L. Yang, W.-K. Hsieh, F. Zavaliche, Y.-H. Chu, U. Dahmen, and R. Ramesh. Self-Assembled Growth of BiFeO3–CoFe2O4 Nanostructures. *Advanced Materials*, 18(20):2747–2752, October 2006.

[67] Haimei Zheng, Qian Zhan, Florin Zavaliche, Matt Sherburne, Florian Straub, Maria P. Cruz, Long-Qing Chen, Uli Dahmen, and R. Ramesh. Controlling Self-Assembled Perovskite-Spinel Nanostructures. *Nano Letters*, 6(7):1401–1407, July 2006.

[68] H. Zheng, J. Wang, L. Mohaddes-Ardabili, M. Wuttig, L. Salamanca-Riba, D. G. Schlom, and R. Ramesh. Three-dimensional heteroepitaxy in self-assembled BaTiO3–CoFe2O4 nanostructures. *Applied Physics Letters*, 85(11):2035–2037, September 2004.

[69] Eun-Mi Choi, Bonan Zhu, Ping Lu, John Feighan, Xing Sun, Haiyan Wang, and Judith L. MacManus-Driscoll. Magnetic signatures of 120 K superconductivity at interfaces in La2CuO4+δ. *Nanoscale*, 12(5):3157–3165, February 2020.

[70] Sophie A. Harrington, Junyi Zhai, Sava Denev, Venkatraman Gopalan, Haiyan Wang, Zhenxing Bi, Simon A. T. Redfern, Seung-Hyub Baek, Chung W. Bark, Chang-Beom Eom, Quanxi Jia, Mary E. Vickers, and Judith L. MacManus-Driscoll. Thick lead-free ferroelectric films with high Curie temperatures through nanocomposite-induced strain. *Nature Nanotechnology*, 6(8):491–495, 2011.

[71] H. Zheng, J. Wang, S. E. Lofland, Z. Ma, L. Mohaddes-Ardabili, T. Zhao, L. Salamanca-Riba, S. R. Shinde, S. B. Ogale, F. Bai, D. Viehland, Y. Jia, D. G. Schlom, M. Wuttig, A. Roytburd, and R. Ramesh. Multiferroic BaTiO3-CoFe2O4 Nanostructures. *Science*, 303(5658):661–663, January 2004.

[72] Shinbuhm Lee, Wenrui Zhang, Fauzia Khatkhatay, Quanxi Jia, Haiyan Wang, and Judith L. MacManus-Driscoll. Strain Tuning and Strong Enhancement of Ionic Conductivity in SrZrO3-RE2O3 (RE = Sm, Eu, Gd, Dy, and Er) Nanocomposite Films. *Advanced Functional Materials*, 25(27):4328–4333, July 2015.

[73] Shinbuhm Lee and Judith L. MacManus-Driscoll. Research Update: Fast and tunable nanoionics in vertically aligned nanostructured films. *APL Materials*, 5(4):042304, March 2017.

[74] Seungho Cho, Chao Yun, Stefan Tappertzhofen, Ahmed Kursumovic, Shinbuhm Lee, Ping Lu, Quanxi Jia, Meng Fan, Jie Jian, Haiyan Wang, Stephan Hofmann, and Judith L. MacManus-Driscoll. Self-assembled oxide films with tailored nanoscale ionic and electronic channels for controlled resistive switching. *Nature Communications*, 7, August 2016.

[75] Daniele Ielmini. Resistive switching memories based on metal oxides: Mechanisms, reliability and scaling. *Semiconductor Science and Technology*, 31(6):063002, June 2016.

[76] Akihito Sawa. Resistive switching in transition metal oxides. *Materials Today*, 11(6):28–36, June 2008.

[77] Shinbuhm Lee, Abhijeet Sangle, Ping Lu, Aiping Chen, Wenrui Zhang, Jae Sung Lee, Haiyan Wang, Quanxi Jia, and Judith L. MacManus-Driscoll. Novel Electroforming-Free Nanoscaffold Memristor with Very High Uniformity, Tunability, and Density. *Advanced Materials*, 26(36):6284–6289, September 2014.

[78] Marita O'Sullivan, Joke Hadermann, Matthew S. Dyer, Stuart Turner, Jonathan Alaria, Troy D. Manning, Artem M. Abakumov, John B. Claridge, and Matthew J. Rosseinsky. Interface control by chemical and dimensional matching in an oxide heterostructure. *Nature Chemistry*, 8(4):347–353, April 2016.

[79] Shiyou Liang, Xiang Zheng, Jing Zhu, and Rong Yu. Coherent Topotactic Interface between Corundum and Rutile Structures. *The Journal of Physical Chemistry C*, 123(1):534–540, January 2019.

[80] S. von Alfthan, P. D. Haynes, K. Kaski, and A. P. Sutton. Are the Structures of Twist Grain Boundaries in Silicon Ordered at 0 K? *Physical Review Letters*, 96(5):055505, February 2006.

[81] Shin Kiyohara, Hiromi Oda, Tomohiro Miyata, and Teruyasu Mizoguchi. Prediction of interface structures and energies via virtual screening. *Science Advances*, 2(11):e1600746, November 2016.

[82] Shin Kiyohara, Hiromi Oda, Koji Tsuda, and Teruyasu Mizoguchi. Acceleration of stable interface structure searching using a kriging approach. *Japanese Journal of Applied Physics*, 55(4):045502, April 2016.

[83] Qiang Zhu, Amit Samanta, Bingxi Li, Robert E. Rudd, and Timofey Frolov. Predicting phase behavior of grain boundaries with evolutionary search and machine learning. *Nature Communications*, 9(1):467, February 2018.

[84] Wei Li Cheah, David W. McComb, and Michael W. Finnis. Structure and ionic diffusivity in an yttria-stabilised zirconia/strontium titanate multilayer. *Acta Materialia*, 129:388–397, May 2017.

[85] H. J. Xiang, Juarez L. F. Da Silva, Howard M. Branz, and Su-Huai Wei. Understanding the clean interface between covalent si and ionic Al_2O_3. *Physical Review Letters*, 103(11):116101, September 2009.

[86] Xin Zhao, Qiang Shu, Manh Cuong Nguyen, Yangang Wang, Min Ji, Hongjun Xiang, Kai-Ming Ho, Xingao Gong, and Cai-Zhuang Wang. Interface Structure Prediction from First-Principles. *Journal of Physical Chemistry C*, 118(18):9524–9530, May 2014.

[87] Georg Schusteritsch and Chris J. Pickard. Predicting interface structures: From SrTiO3 to graphene. *Physical Review B - Condensed Matter and Materials Physics*, 90(3):1–7, 2014.

[88] Anastasia V. Tyurnina, Hanako Okuno, Pascal Pochet, and Jean Dijon. CVD graphene recrystallization as a new route to tune graphene structure and properties. *Carbon*, 102:499–505, June 2016.

[89] C. J. Howard and H. T. Stokes. Group-Theoretical Analysis of Octahedral Tilting in Perovskites. *Acta Crystallographica Section B: Structural Science*, 54(6):782–789, December 1998.

[90] C. J. Howard and H. T. Stokes. Group-Theoretical Analysis of Octahedral Tilting in Perovskites. Erratum. *Acta Crystallographica Section B: Structural Science*, 58(3):565–565, June 2002.

[91] D. Hanneke, S. Fogwell, and G. Gabrielse. New Measurement of the Electron Magnetic Moment and the Fine Structure Constant. *Physical Review Letters*, 100(12):120801, March 2008.

[92] Paul Adrien Maurice Dirac and Ralph Howard Fowler. Quantum mechanics of many-electron systems. *Proceedings of the Royal Society of London. Series A, Containing Papers of a Mathematical and Physical Character*, 123(792):714–733, April 1929.

[93] P. Hohenberg and W. Kohn. Inhomogeneous Electron Gas. *Physical Review*, 136(3B):B864–B871, November 1964.

[94] Axel D. Becke. Perspective: Fifty years of density-functional theory in chemical physics. *The Journal of Chemical Physics*, 140(18):18A301, April 2014.

[95] Kieron Burke. Perspective on density functional theory. *The Journal of Chemical Physics*, 136(15):150901, April 2012.

[96] Richard M. Martin. *Electronic Structure: Basic Theory and Practical Methods / Richard M. Martin.* University Press, Cambridge, reprint of 2008 ed. with corrections. edition, 2010.

[97] M. C. Payne, M. P. Teter, D. C. Allan, T. A. Arias, and J. D. Joannopoulos. Iterative minimization techniques for ab initio total-energy calculations: Molecular dynamics and conjugate gradients. *Reviews of Modern Physics*, 64(4):1045–1097, October 1992.

[98] Jorge Kohanoff. *Electronic Structure Calculations for Solids and Molecules: Theory and Computational Methods*. Cambridge University Press, Cambridge, 2006.

[99] M. Born and R. Oppenheimer. Zur Quantentheorie der Molekeln. *Annalen der Physik*, 389(20):457–484, 1927.

[100] Richard E Bellman. *Dynamic Programming*. 2010.

[101] D. R. Hartree. The Wave Mechanics of an Atom with a Non-Coulomb Central Field. Part I. Theory and Methods. *Mathematical Proceedings of the Cambridge Philosophical Society*, 24(1):89–110, January 1928.

[102] Frank Jensen. *Introduction to Computational Chemistry, 2nd Edition*. Second edition, 2013.

[103] E Fermi. Un metodo statistico per la determinazione di alcune priorieta dell atome. Rend. Acad. *Nat. Lincei*, 6, 1927.

[104] L. H. Thomas. The calculation of atomic fields. *Mathematical Proceedings of the Cambridge Philosophical Society*, 23(5):542–548, January 1927.

[105] W. Kohn and L. J. Sham. Self-Consistent Equations Including Exchange and Correlation Effects. *Physical Review*, 140(4A):A1133–A1138, November 1965.

[106] E. Wigner. Effects of the electron interaction on the energy levels of electrons in metals. *Transactions of the Faraday Society*, 34(0):678–685, January 1938.

[107] D. M. Ceperley and B. J. Alder. Ground State of the Electron Gas by a Stochastic Method. *Physical Review Letters*, 45(7):566–569, August 1980.

[108] John P. Perdew, Kieron Burke, and Matthias Ernzerhof. Generalized Gradient Approximation Made Simple. *Physical Review Letters*, 77(18):3865–3868, October 1996.

[109] John P. Perdew and Yue Wang. Accurate and simple analytic representation of the electron-gas correlation energy. *Physical Review B*, 45(23):13244–13249, June 1992.

[110] Philipp Haas, Fabien Tran, and Peter Blaha. Calculation of the lattice constant of solids with semilocal functionals. *Physical Review B*, 79(8):085104, February 2009.

[111] John P. Perdew, Adrienn Ruzsinszky, Gábor I. Csonka, Oleg A. Vydrov, Gustavo E. Scuseria, Lucian A. Constantin, Xiaolan Zhou, and Kieron Burke. Restoring the Density-Gradient Expansion for Exchange in Solids and Surfaces. *Physical Review Letters*, 100(13):136406, April 2008.

[112] Jianwei Sun, Adrienn Ruzsinszky, and John P. Perdew. Strongly Constrained and Appropriately Normed Semilocal Density Functional. *Physical Review Letters*, 115(3):036402, July 2015.

[113] Albert P. Bartók and Jonathan R. Yates. Regularized SCAN functional. *The Journal of Chemical Physics*, 150(16):161101, April 2019.

[114] Aliaksandr V. Krukau, Oleg A. Vydrov, Artur F. Izmaylov, and Gustavo E. Scuseria. Influence of the exchange screening parameter on the performance of screened hybrid functionals. *The Journal of Chemical Physics*, 125(22):224106, December 2006.

[115] Richard L. Martin and Francesc Illas. Antiferromagnetic Exchange Interactions from Hybrid Density Functional Theory. *Physical Review Letters*, 79(8):1539–1542, August 1997.

[116] Carlo Adamo and Vincenzo Barone. Toward reliable density functional methods without adjustable parameters: The PBE0 model. *The Journal of Chemical Physics*, 110(13):6158–6170, March 1999.

[117] Stewart J. Clark and John Robertson. Screened exchange density functional applied to solids. *Physical Review B*, 82(8):085208, August 2010.

[118] M. J. Lucero, T. M. Henderson, and G. E. Scuseria. Improved semiconductor lattice parameters and band gaps from a middle-range screened hybrid exchange functional. *Journal of Physics: Condensed Matter*, 24(14):145504, March 2012.

[119] A. I. Liechtenstein, V. I. Anisimov, and J. Zaanen. Density-functional theory and strong interactions: Orbital ordering in Mott-Hubbard insulators. *Physical Review B*, 52(8):R5467–R5470, August 1995.

[120] S. L. Dudarev, G. A. Botton, S. Y. Savrasov, C. J. Humphreys, and A. P. Sutton. Electron-energy-loss spectra and the structural stability of nickel oxide: An LSDA+U study. *Physical Review B*, 57(3):1505–1509, January 1998.

[121] Matteo Cococcioni and Stefano de Gironcoli. Linear response approach to the calculation of the effective interaction parameters in the LDA+U method. *Physical Review B*, 71(3):035105, January 2005.

[122] Stewart J. Clark, Matthew D. Segall, Chris J. Pickard, Phil J. Hasnip, Matt I. J. Probert, Keith Refson, and Mike C. Payne. First principles methods using CASTEP. *Zeitschrift für Kristallographie*, 220(5-6-2005):567–570, 2005.

[123] Shigeji Fujita and Kei Ito. Bloch Theorem. In Shigeji Fujita and Kei Ito, editors, *Quantum Theory of Conducting Matter: Newtonian Equations of Motion for a Bloch Electron*, pages 85–95. Springer, New York, NY, 2007.

[124] James W. Cooley and John W. Tukey. An algorithm for the machine calculation of complex Fourier series. *Mathematics of Computation*, 19(90):297–301, 1965.

[125] R. Car and M. Parrinello. Unified Approach for Molecular Dynamics and Density-Functional Theory. *Physical Review Letters*, 55(22):2471–2474, November 1985.

[126] G. Kresse and J. Furthmüller. Efficient iterative schemes for ab initio total-energy calculations using a plane-wave basis set. *Physical Review B*, 54(16):11169–11186, October 1996.

[127] Ernest R. Davidson. The iterative calculation of a few of the lowest eigenvalues and corresponding eigenvectors of large real-symmetric matrices. *Journal of Computational Physics*, 17(1):87–94, January 1975.

[128] C. G. Broyden. A class of methods for solving nonlinear simultaneous equations. *Mathematics of Computation*, 19(92):577–593, 1965.

[129] Péter Pulay. Convergence acceleration of iterative sequences. the case of scf iteration. *Chemical Physics Letters*, 73(2):393–398, July 1980.

[130] Volker Heine. The Pseudopotential Concept. In Henry Ehrenreich, Frederick Seitz, and David Turnbull, editors, *Solid State Physics*, volume 24, pages 1–36. Academic Press, January 1970.

[131] Marvin L. Cohen and Volker Heine. The Fitting of Pseudopotentials to Experimental Data and Their Subsequent Application. In Henry Ehrenreich, Frederick Seitz, and David Turnbull, editors, *Solid State Physics*, volume 24, pages 37–248. Academic Press, January 1970.

[132] Peter Schwerdtfeger. The Pseudopotential Approximation in Electronic Structure Theory. *ChemPhysChem*, 12(17):3143–3155, 2011.

[133] D. R. Hamann, M. Schlüter, and C. Chiang. Norm-Conserving Pseudopotentials. *Physical Review Letters*, 43(20):1494–1497, November 1979.

[134] Leonard Kleinman and D. M. Bylander. Efficacious Form for Model Pseudopotentials. *Physical Review Letters*, 48(20):1425–1428, May 1982.

[135] David Vanderbilt. Soft self-consistent pseudopotentials in a generalized eigenvalue formalism. *Physical Review B*, 41(11):7892–7895, April 1990.

[136] P. E. Blöchl. Projector augmented-wave method. *Physical Review B*, 50(24):17953–17979, December 1994.

[137] G. Kresse and D. Joubert. From ultrasoft pseudopotentials to the projector augmented-wave method. *Physical Review B*, 59(3):1758–1775, January 1999.

[138] Chris J. Pickard and Francesco Mauri. All-electron magnetic response with pseudopotentials: NMR chemical shifts. *Physical Review B*, 63(24):245101, May 2001.

[139] Jonathan R. Yates and Chris J. Pickard. Computations of Magnetic Resonance Parameters for Crystalline Systems: Principles. *eMagRes*, 2008.

[140] Thomas Gregor, Francesco Mauri, and Roberto Car. A comparison of methods for the calculation of NMR chemical shifts. *The Journal of Chemical Physics*, 111(5):1815–1822, July 1999.

[141] Jonathan R. Yates, Chris J. Pickard, and Francesco Mauri. Calculation of NMR chemical shifts for extended systems using ultrasoft pseudopotentials. *Physical Review B*, 76(2):024401, July 2007.

[142] Richard LeSar. *Introduction to Computational Materials Science: Fundamentals to Applications*. Cambridge University Press, Cambridge, 2013.

[143] R. A. Buckingham and John Edward Lennard-Jones. The classical equation of state of gaseous helium, neon and argon. *Proceedings of the Royal Society of London. Series A. Mathematical and Physical Sciences*, 168(933):264–283, October 1938.

[144] Nicole A. Benedek, Alvin L.-S. Chua, Christian Elsässer, Adrian P. Sutton, and Mike W. Finnis. Interatomic potentials for strontium titanate: An assessment of their transferability and comparison with density functional theory. *Physical Review B*, 78(6):064110, August 2008.

[145] J. E. Jones and Sydney Chapman. On the determination of molecular fields. —II. From the equation of state of a gas. *Proceedings of the Royal Society of London. Series A, Containing Papers of a Mathematical and Physical Character*, 106(738):463–477, October 1924.

[146] William C. Swope, Hans C. Andersen, Peter H. Berens, and Kent R. Wilson. A computer simulation method for the calculation of equilibrium constants for the formation of physical clusters of molecules: Application to small water clusters. *The Journal of Chemical Physics*, 76(1):637–649, January 1982.

[147] Glenn J. Martyna, Michael L. Klein, and Mark Tuckerman. Nosé–Hoover chains: The canonical ensemble via continuous dynamics. *The Journal of Chemical Physics*, 97(4):2635–2643, August 1992.

[148] Julian D. Gale and Andrew L. Rohl. The General Utility Lattice Program (GULP). *Molecular Simulation*, 29(5):291–341, May 2003.

[149] Steve Plimpton. Fast Parallel Algorithms for Short-Range Molecular Dynamics. *Journal of Computational Physics*, 117(1):1–19, March 1995.

[150] Lambert Ben Freund and Subra Suresh. *Thin Film Materials: Stress, Defect Formation and Surface Evolution*. Cambridge University Press, 2004.

[151] Frederick Charles Frank, J. H. Van Der Merwe, and Nevill Francis Mott. One-dimensional dislocations. II. Misfitting monolayers and oriented overgrowth. *Proceedings of the Royal Society of London. Series A. Mathematical and Physical Sciences*, 198(1053):216–225, August 1949.

[152] Tatau Nishinga. *Handbook of Crystal Growth Thin Films and Epitaxy: Basic Techniques*, volume III. Second edition edition, 2015.

[153] J. Narayan and B. C. Larson. Domain epitaxy: A unified paradigm for thin film growth. *Journal of Applied Physics*, 93(1):278–285, December 2002.

[154] Blas Pedro Uberuaga, Pratik P. Dholabhai, Ghanshyam Pilania, and Aiping Chen. Semicoherent oxide heterointerfaces: Structure, properties, and implications. *APL Materials*, 7(10):100904, October 2019.

[155] David S. Sholl and Janice A. Steckel. *Density Functional Theory: A Practical Introduction*. Wiley, Hoboken, N.J, 2009.

[156] In-Chul Yeh and Max L. Berkowitz. Ewald summation for systems with slab geometry. *The Journal of Chemical Physics*, 111(7):3155–3162, August 1999.

[157] Jörg Neugebauer and Matthias Scheffler. Adsorbate-substrate and adsorbate-adsorbate interactions of Na and K adlayers on Al(111). *Physical Review B*, 46(24):16067–16080, December 1992.

[158] Jr Malcolm W. Chase. *NIST-JANAF Thermochemical Tables*. Fourth edition. Washington, DC : American Chemical Society ; New York : American Institute of Physics for the National Institute of Standards and Technology, 1998., 1998.

[159] Bin Feng, Issei Sugiyama, Hajime Hojo, Hiromichi Ohta, Naoya Shibata, and Yuichi Ikuhara. Atomic structures and oxygen dynamics of CeO_2 grain boundaries. *Scientific Reports*, 6:20288, February 2016.

[160] R. I. Eglitis and David Vanderbilt. First-principles calculations of atomic and electronic structure of SrTiO3 (001) and (011) surfaces. *Physical Review B*, 77(19):195408, May 2008.

[161] Frank H. Stillinger. Exponential multiplicity of inherent structures. *Physical Review E*, 59(1):48–51, January 1999.

[162] S. Kirkpatrick, Jr. Gelatt, and M.P. Vecchi. Optimization by simulated annealing. *Science*, 220(4598):671–680, 1983.

[163] David J. Wales and Harold A. Scheraga. Global Optimization of Clusters, Crystals, and Biomolecules. *Science*, 285(5432):1368–1372, August 1999.

[164] Stefan Goedecker. Minima hopping: An efficient search method for the global minimum of the potential energy surface of complex molecular systems. *The Journal of Chemical Physics*, 120(21):9911–9917, May 2004.

[165] Thomas Bäck. *Evolutionary Algorithms in Theory and Practice: Evolution Strategies, Evolutionary Programming, Genetic Algorithms*. Oxford University Press, Inc., USA, 1996.

[166] Artem R. Oganov, Andriy O. Lyakhov, and Mario Valle. How Evolutionary Crystal Structure Prediction Works—and Why. *Accounts of Chemical Research*, 44(3):227–237, March 2011.

[167] Eberhart and Yuhui Shi. Particle swarm optimization: Developments, applications and resources. In *Proceedings of the 2001 Congress on Evolutionary Computation (IEEE Cat. No.01TH8546)*, volume 1, pages 81–86 vol. 1, May 2001.

[168] Yanchao Wang, Jian Lv, Li Zhu, and Yanming Ma. CALYPSO: A method for crystal structure prediction. *Computer Physics Communications*, 183(10):2063–2070, October 2012.

[169] D.H. Wolpert and W.G. Macready. No free lunch theorems for optimization. *IEEE Transactions on Evolutionary Computation*, 1(1):67–82, April 1997.

[170] Chris J. Pickard and R. J. Needs. High-Pressure Phases of Silane. *Physical Review Letters*, 97(4):045504, July 2006.

[171] Chris J Pickard and R J Needs. Ab initio random structure searching. *Journal of physics. Condensed matter : an Institute of Physics journal*, 23(5):053201–053201, 2011.

[172] Chris J. Pickard and Richard J. Needs. Structure of phase III of solid hydrogen. *Nature Physics*, 3(7):473–476, July 2007.

[173] Joseph R. Nelson, Richard J. Needs, and Chris J. Pickard. High-pressure CaF_2 revisited: A new high-temperature phase and the role of phonons in the search for superionic conductivity. *Physical Review B*, 98(22):224105, December 2018.

[174] Bartomeu Monserrat, Miguel Martinez-Canales, Richard J. Needs, and Chris J. Pickard. Helium-Iron Compounds at Terapascal Pressures. *Physical Review Letters*, 121(1):015301, July 2018.

[175] Andrew J. Morris, Chris J. Pickard, and R. J. Needs. Hydrogen/nitrogen/oxygen defect complexes in silicon from computational searches. *Physical Review B*, 80(14):144112, October 2009.

[176] Ji Chen, Georg Schusteritsch, Chris J. Pickard, Christoph G. Salzmann, and Angelos Michaelides. Two Dimensional Ice from First Principles: Structures and Phase Transitions. *Physical Review Letters*, 116(2):025501, January 2016.

[177] Jonathan P. K. Doye, David J. Wales, and Mark A. Miller. Thermodynamics and the global optimization of Lennard-Jones clusters. *The Journal of Chemical Physics*, 109(19):8143–8153, November 1998.

[178] Claire P. Massen and Jonathan P. K. Doye. Power-law distributions for the areas of the basins of attraction on a potential energy landscape. *Physical Review E*, 75(3):037101, March 2007.

[179] Lixin Sun, Dario Marrocchelli, and Bilge Yildiz. Edge dislocation slows down oxide ion diffusion in doped CeO_2 by segregation of charged defects. *Nature Communications*, 6:ncomms7294, February 2015.

[180] Licia Minervini, Matthew O. Zacate, and Robin W. Grimes. Defect cluster formation in M2O3-doped CeO2. *Solid State Ionics*, 116(3):339–349, January 1999.

[181] Chris Pickard. AIRSS, 2019. https://www.mtg.msm.cam.ac.uk/Codes/AIRSS.

[182] YongMan Choi, M. Scott, T. Söhnel, and Hicham Idriss. A DFT + U computational study on stoichiometric and oxygen deficient M–CeO2 systems (M = Pd1, Rh1, Rh10, Pd10 and Rh4Pd6). *Physical Chemistry Chemical Physics*, 16(41):22588–22599, September 2014.

[183] C. W. M. Castleton, J. Kullgren, and K. Hermansson. Tuning LDA+U for electron localization and structure at oxygen vacancies in ceria. *The Journal of Chemical Physics*, 127(24):244704, December 2007.

[184] Leonardo Triggiani, Ana B. Muñoz-García, Angela Agostiano, and Michele Pavone. Promoting oxygen vacancy formation and p-type conductivity in SrTiO 3 via alkali metal doping: A first principles study. *Physical Chemistry Chemical Physics*, 18(41):28951–28959, 2016.

[185] Rossitza Pentcheva and Warren E. Pickett. Avoiding the polarization catastrophe in LaAlO3 overlayers on SrTiO3(001) through polar distortion. *Physical Review Letters*, 102(10):3–6, 2009.

[186] Y. A. Abramov, V. G. Tsirelson, V. E. Zavodnik, S. A. Ivanov, and I. D. Brown. The chemical bond and atomic displacements in SrTiO3 from X-ray diffraction analysis. *Acta Crystallographica Section B: Structural Science*, 51(6):942–951, December 1995.

[187] J. D. McCullough. An X-Ray Study of the Rare-earth Oxide Systems: CeIV—NdIII, CrIV—PrIII, CeIV—PrIV and PrIV—NdIII1. *Journal of the American Chemical Society*, 72(3):1386–1390, March 1950.

[188] Albert P. Bartók, Risi Kondor, and Gábor Csányi. On representing chemical environments. *Physical Review B*, 87(18):184115, May 2013.

[189] N. F. Mott and M. J. Littleton. Conduction in polar crystals. I. Electrolytic conduction in solid salts. *Transactions of the Faraday Society*, 34(0):485–499, January 1938.

[190] Pratik P. Dholabhai, Enrique Martinez, Nicholas T. Brown, and Blas Pedro Uberuaga. On the mobility of carriers at semi-coherent oxide heterointerfaces. *Physical Chemistry Chemical Physics*, 19(34):23122–23130, September 2017.

[191] Hajime Hojo, Eita Tochigi, Teruyasu Mizoguchi, Hiromichi Ohta, Naoya Shibata, Bin Feng, and Yuichi Ikuhara. Atomic structure and strain field of threading dislocations in CeO2 thin films on yttria-stabilized ZrO2. *Applied Physics Letters*, 98(15):153104, April 2011.

[192] Marc Legros, Gerhard Dehm, Eduard Arzt, and T. John Balk. Observation of Giant Diffusivity Along Dislocation Cores. *Science*, 319(5870):1646–1649, March 2008.

[193] Kazuya Otsuka, Akihide Kuwabara, Atsutomo Nakamura, Takahisa Yamamoto, Katsuyuki Matsunaga, and Yuichi Ikuhara. Dislocation-enhanced ionic conductivity of yttria-stabilized zirconia. *Applied Physics Letters*, 82(6):877–879, February 2003.

[194] M. J. D. Rushton, A. Chroneos, S. J. Skinner, J. A. Kilner, and R. W. Grimes. Effect of strain on the oxygen diffusion in yttria and gadolinia co-doped ceria. *Solid State Ionics*, 230:37–42, January 2013.

[195] Dilpuneet S. Aidhy, Yanwen Zhang, and William J. Weber. Strained Ionic Interfaces: Effect on Oxygen Diffusivity from Atomistic Simulations. *The Journal of Physical Chemistry C*, 118(8):4207–4212, February 2014.

[196] Stephen Hull. Superionics: Crystal structures and conduction processes. *Reports on Progress in Physics*, 67(7):1233, 2004.

[197] G. Herranz, M. Basletić, M. Bibes, C. Carrétéro, E. Tafra, E. Jacquet, K. Bouzehouane, C. Deranlot, A. Hamzić, J.-M. Broto, A. Barthélémy, and A. Fert. High mobility in $LaAlO_3/SrTiO_3$ heterostructures: Origin, dimensionality, and perspectives. *Physical Review Letters*, 98(21):216803, May 2007.

[198] Liping Yu and Alex Zunger. A polarity-induced defect mechanism for conductivity and magnetism at polar–nonpolar oxide interfaces. *Nature Communications*, 5(1):1–9, October 2014.

[199] Igor Kosacki, Christopher M. Rouleau, Paul F. Becher, James Bentley, and Douglas H. Lowndes. Nanoscale effects on the ionic conductivity in highly textured YSZ thin films. *Solid State Ionics*, 176(13–14):1319–1326, April 2005.

[200] Thi X. T. Sayle, Stephen C. Parker, and Dean C. Sayle. Ionic conductivity in nano-scale CeO2/YSZ heterolayers. 16(11):1067–1081, March 2006.

[201] C. Korte, A. Peters, J. Janek, D. Hesse, and N. Zakharov. Ionic conductivity and activation energy for oxygen ion transport in superlattices—the semicoherent multilayer system YSZ (ZrO2 + 9.5 mol% Y2O3)/Y2O3. *Physical Chemistry Chemical Physics*, 10(31):4623–4635, July 2008.

[202] Andrea Cavallaro, Belén Ballesteros, Romain Bachelet, and José Santiso. Heteroepitaxial orientation control of YSZ thin films by selective growth on SrO-, TiO2-terminated SrTiO3 crystal surfaces. *CrystEngComm*, 13(5):1625–1631, February 2011.

[203] S. A. Pauli, S. J. Leake, B. Delley, M. Björck, C. W. Schneider, C. M. Schlepütz, D. Martoccia, S. Paetel, J. Mannhart, and P. R. Willmott. Evolution of the interfacial structure of $LaAlO_3$ on $SrTiO_3$. *Physical Review Letters*, 106(3):036101, January 2011.

[204] Jichao C. Li, Juan Ignacio Beltrán, and M. Carmen Muñoz. Multiorbital structure of the two-dimensional electron gas in $\mathbf{LaAlO_3/SrTiO_3}$ heterostructures: The formation of a $\mathbf{d_{xy}}$ ferromagnetic sheet. *Physical Review B*, 87(7):075411, February 2013.

[205] Jun ZHANG, Feng WEI, Zhimin YANG, Qiuyun CHEN, Jun CHEN, and Shuming WANG. Structure and chemical states of highly eptiaxial CeO2(001) films grown on SrTiO3 substrate by laser molecular beam epitaxy. *Journal of Rare Earths*, 31(12):1191–1194, December 2013.

[206] Niranjan Govind, Max Petersen, George Fitzgerald, Dominic King-Smith, and Jan Andzelm. A generalized synchronous transit method for transition state location. *Computational Materials Science*, 28(2):250–258, October 2003.

[207] Graeme Henkelman, Blas P. Uberuaga, and Hannes Jónsson. A climbing image nudged elastic band method for finding saddle points and minimum energy paths. *The Journal of Chemical Physics*, 113(22):9901–9904, November 2000.

[208] Ask Hjorth Larsen, Jens Jørgen Mortensen, Jakob Blomqvist, Ivano E. Castelli, Rune Christensen, Marcin Dułak, Jesper Friis, Michael N. Groves, Bjørk Hammer, Cory Hargus, Eric D. Hermes, Paul C. Jennings, Peter Bjerre Jensen, James Kermode, John R. Kitchin, Esben Leonhard Kolsbjerg, Joseph Kubal, Kristen Kaasbjerg, Steen Lysgaard, Jón Bergmann Maronsson, Tristan Maxson, Thomas Olsen, Lars Pastewka, Andrew Peterson, Carsten Rostgaard, Jakob Schiøtz, Ole Schütt, Mikkel Strange, Kristian S. Thygesen, Tejs Vegge, Lasse Vilhelmsen, Michael Walter, Zhenhua Zeng, and Karsten W. Jacobsen. The atomic simulation environment—a Python library for working with atoms. *Journal of Physics: Condensed Matter*, 29(27):273002, 2017.

[209] K. Tsuda and M. Tanaka. Refinement of crystal structure parameters using convergent-beam electron diffraction: The low-temperature phase of SrTiO3. *Acta Crystallographica Section A: Foundations of Crystallography*, 51(1):7–19, January 1995.

[210] Mario Burbano, David O. Scanlon, and Graeme W. Watson. Sources of Conductivity and Doping Limits in CdO from Hybrid Density Functional Theory. *Journal of the American Chemical Society*, 133(38):15065–15072, September 2011.

[211] Anderson Janotti and Chris G. Van de Walle. Native point defects in ZnO. *Physical Review B*, 76(16):165202, October 2007.

[212] Alexey A. Sokol, Aron Walsh, and C. Richard A. Catlow. Oxygen interstitial structures in close-packed metal oxides. *Chemical Physics Letters*, 492(1):44–48, May 2010.

[213] Lei Wang, Thomas Maxisch, and Gerbrand Ceder. Oxidation energies of transition metal oxides within the GGA+U framework. *Physical Review B*, 73(19):195107, May 2006.

[214] Pratik P. Dholabhai, Jeffery A. Aguiar, Amit Misra, and Blas P. Uberuaga. Defect interactions with stepped CeO2/SrTiO3 interfaces: Implications for radiation damage evolution and fast ion conduction. *The Journal of Chemical Physics*, 140(19):194701, May 2014.

[215] C. R. Stanek, M. R. Bradford, and R. W. Grimes. Segregation of Ba2+, Sr2+, Ce4+ and Zr4+ to UO2 surfaces. *Journal of Physics: Condensed Matter*, 16(27):S2699–S2714, June 2004.

[216] Paula Neuderth, Pascal Hille, Sara Martí-Sánchez, María de la Mata, Mariona Coll, Jordi Arbiol, and Martin Eickhoff. Optical Analysis of Oxygen Self-Diffusion in Ultrathin CeO2 Layers at Low Temperatures. *Advanced Energy Materials*, 8(29):1802120, 2018.

[217] Zhiwei Cui, Yi Sun, and Jianmin Qu. Molecular dynamics simulation of reduced CeO2. *Solid State Ionics*, 226:24–29, October 2012.

[218] R. D. Shannon. Revised effective ionic radii and systematic studies of interatomic distances in halides and chalcogenides. *Acta Crystallographica Section A: Crystal Physics, Diffraction, Theoretical and General Crystallography*, 32(5):751–767, September 1976.

[219] N. M. Sammes, G. A. Tompsett, H. Näfe, and F. Aldinger. Bismuth based oxide electrolytes— structure and ionic conductivity. *Journal of the European Ceramic Society*, 19(10):1801–1826, August 1999.

[220] James M. Rondinelli and Nicola A. Spaldin. Substrate coherency driven octahedral rotations in perovskite oxide films. *Physical Review B*, 82(11):113402, September 2010.

[221] Zhaoliang Liao, Nicolas Gauquelin, Robert J. Green, Sebastian Macke, Julie Gonnissen, Sean Thomas, Zhicheng Zhong, Lin Li, Liang Si, Sandra Van Aert, Philipp Hansmann, Karsten Held, Jing Xia, Johan Verbeeck, Gustaaf Van Tendeloo, George A.

Sawatzky, Gertjan Koster, Mark Huijben, and Guus Rijnders. Thickness Dependent Properties in Oxide Heterostructures Driven by Structurally Induced Metal–Oxygen Hybridization Variations. *Advanced Functional Materials*, 27(17):1606717, 2017.

[222] M. Huijben, G. Koster, Z. L. Liao, and G. Rijnders. Interface-engineered oxygen octahedral coupling in manganite heterostructures. *Applied Physics Reviews*, 4(4):041103, October 2017.

[223] James M. Rondinelli, Steven J. May, and John W. Freeland. Control of octahedral connectivity in perovskite oxide heterostructures: An emerging route to multifunctional materials discovery. *MRS Bulletin*, 37(3):261–270, March 2012.

[224] J. S. Moodera, X. Hao, G. A. Gibson, and R. Meservey. Electron-Spin Polarization in Tunnel Junctions in Zero Applied Field with Ferromagnetic EuS Barriers. *Physical Review Letters*, 61(5):637–640, August 1988.

[225] P. LeClair, J. K. Ha, H. J. M. Swagten, J. T. Kohlhepp, C. H. van de Vin, and W. J. M. de Jonge. Large magnetoresistance using hybrid spin filter devices. *Applied Physics Letters*, 80(4):625–627, January 2002.

[226] Jun Zhang, Hidekazu Tanaka, Teruo Kanki, Jae-Hyoung Choi, and Tomoji Kawai. Strain effect and the phase diagram of $La_{1-x}Ba_xMnO_3$ thin films. *Physical Review B*, 64(18):184404, October 2001.

[227] Andrew J. Morris, Rebecca J. Nicholls, Chris J. Pickard, and Jonathan R. Yates. OptaDOS: A tool for obtaining density of states, core-level and optical spectra from electronic structure codes. *Computer Physics Communications*, 185(5):1477–1485, May 2014.

[228] P. Norby, I. G. Krogh Andersen, E. Krogh Andersen, and N. H. Andersen. The crystal structure of lanthanum manganate(iii), LaMnO3, at room temperature and at 1273 K under N2. *Journal of Solid State Chemistry*, 119(1):191–196, October 1995.

[229] Bjørn C. Hauback, Helmer Fjellvåg, and Natsuko Sakai. Effect of Nonstoichiometry on Properties of La1-tMnO3+δ: III. Magnetic Order Studied by Powder Neutron Diffraction. *Journal of Solid State Chemistry*, 124(1):43–51, June 1996.

[230] Thomas A. Mellan, Furio Corà, Ricardo Grau-Crespo, and Sohrab Ismail-Beigi. Importance of anisotropic coulomb interaction in $LaMnO_3$. *Physical Review B*, 92(8):085151, August 2015.

[231] T. Hashimoto, S. Ishibashi, and K. Terakura. Jahn-teller distortion and magnetic structure in $LaMnO_3$: A first-principles theoretical study with full structure optimizations. *Physical Review B*, 82(4):045124, July 2010.

[232] D. J. Singh and W. E. Pickett. Lattice effects in ferromagnetic manganite perovskites. *Journal of Applied Physics*, 83(11):7354–7356, June 1998.

[233] D. J. Singh and W. E. Pickett. Pseudogaps, Jahn-Teller distortions, and magnetic order in manganite perovskites. *Physical Review B*, 57(1):88–91, January 1998.

[234] Pablo Rivero, Vincent Meunier, and William Shelton. Uniaxial pressure-induced half-metallic ferromagnetic phase transition in LaMnO3. *Physical Review B*, 93(9):094409, March 2016.

[235] L. Bellaiche and David Vanderbilt. Virtual crystal approximation revisited: Application to dielectric and piezoelectric properties of perovskites. *Physical Review B*, 61(12):7877–7882, March 2000.

[236] Teng Gu, Timothy Scarbrough, Yurong Yang, Jorge Íñiguez, L. Bellaiche, and H. J. Xiang. Cooperative Couplings between Octahedral Rotations and Ferroelectricity in Perovskites and Related Materials. *Physical Review Letters*, 120(19):197602, May 2018.

[237] P. W. Tasker. The stability of ionic crystal surfaces. *Journal of Physics C: Solid State Physics*, 12(22):4977–4984, November 1979.

[238] Ivan Lazić, Eric G. T. Bosch, and Sorin Lazar. Phase contrast STEM for thin samples: Integrated differential phase contrast. *Ultramicroscopy*, 160:265–280, January 2016.

[239] P. G. Radaelli, G. Iannone, M. Marezio, H. Y. Hwang, S-W. Cheong, J. D. Jorgensen, and D. N. Argyriou. Structural effects on the magnetic and transport properties of perovskite $A_{1-x}A'_x\mathrm{MnO}_3$ ($x = 0.25,\ 0.30$). *Physical Review B*, 56(13):8265–8276, October 1997.

[240] Jun He. Control of Octahedral Tilts and Magnetic Properties of Perovskite Oxide Heterostructures by Substrate Symmetry. *Physical Review Letters*, 105(22), 2010.

[241] B. J. Campbell, H. T. Stokes, D. E. Tanner, and D. M. Hatch. ISODISPLACE: A web-based tool for exploring structural distortions. *Journal of Applied Crystallography*, 39(4):607–614, August 2006.

[242] Johan Klarbring and Sergei I. Simak. Nature of the octahedral tilting phase transitions in perovskites: A case study of CaMnO_3. *Physical Review B*, 97(2):024108, January 2018.

[243] Jun Hee Lee, Kris T. Delaney, Eric Bousquet, Nicola A. Spaldin, and Karin M. Rabe. Strong coupling of jahn-teller distortion to oxygen-octahedron rotation and functional properties in epitaxially strained orthorhombic LaMnO_3. *Physical Review B*, 88(17):174426, November 2013.

[244] Jerry L. Bettis, Myung-Hwan Whangbo, Jürgen Köhler, Annette Bussmann-Holder, and A. R. Bishop. Lattice dynamical analogies and differences between SrTiO_3 and EuTiO_3 revealed by phonon-dispersion relations and double-well potentials. *Physical Review B*, 84(18):184114, November 2011.

[245] Alison J. Hatt and Nicola A. Spaldin. Structural phases of strained laalo_3 driven by octahedral tilt instabilities. *Physical Review B*, 82(19):195402, November 2010.

[246] Alison J. Hatt, Nicola A. Spaldin, and Claude Ederer. Strain-induced isosymmetric phase transition in BiFeO_3. *Physical Review B*, 81(5):054109, February 2010.

[247] S. J. May, J.-W. Kim, J. M. Rondinelli, E. Karapetrova, N. A. Spaldin, A. Bhattacharya, and P. J. Ryan. Quantifying octahedral rotations in strained perovskite oxide films. *Physical Review B*, 82(1):014110, July 2010.

[248] A. T. Zayak, X. Huang, J. B. Neaton, and Karin M. Rabe. Structural, electronic, and magnetic properties of $SrRuO_3$ under epitaxial strain. *Physical Review B*, 74(9):094104, September 2006.

[249] Eun-Mi Choi, Angelo Di Bernardo, Bonan Zhu, Ping Lu, Hen Alpern, Kelvin H. L. Zhang, Tamar Shapira, John Feighan, Xing Sun, Jason Robinson, Yossi Paltiel, Oded Millo, Haiyan Wang, Quanxi Jia, and Judith L. MacManus-Driscoll. 3D strain-induced superconductivity in La2CuO4+δ using a simple vertically aligned nanocomposite approach. *Science Advances*, 5(4):eaav5532, April 2019.

[250] M. K. Wu, J. R. Ashburn, C. J. Torng, P. H. Hor, R. L. Meng, L. Gao, Z. J. Huang, Y. Q. Wang, and C. W. Chu. Superconductivity at 93 K in a new mixed-phase Y-Ba-Cu-O compound system at ambient pressure. *Physical Review Letters*, 58(9):908–910, March 1987.

[251] J. Bardeen, L. N. Cooper, and J. R. Schrieffer. Theory of Superconductivity. *Physical Review*, 108(5):1175–1204, December 1957.

[252] Vladimir Y. Butko, Gennady Logvenov, Natasha Božović, Zoran Radović, and Ivan Božović. Madelung Strain in Cuprate Superconductors – A Route to Enhancement of the Critical Temperature. *Advanced Materials*, 21(36):3644–3648, 2009.

[253] Magnus Nord, Per Erik Vullum, Ian MacLaren, Thomas Tybell, and Randi Holmestad. Atomap: A new software tool for the automated analysis of atomic resolution images using two-dimensional Gaussian fitting. *Advanced Structural and Chemical Imaging*, 3(1):9, December 2017.

[254] M. Naito, A. Tsukada, T. Greibe, and H. Sato. Phase control in La-214 epitaxial thin films. *arXiv:cond-mat/0209277*, page 140, November 2002.

[255] Giovanni Pizzi, Andrea Cepellotti, Riccardo Sabatini, Nicola Marzari, and Boris Kozinsky. AiiDA: Automated interactive infrastructure and database for computational science. *Computational Materials Science*, 111:218–230, January 2016.

[256] Sebastiaan P. Huber, Spyros Zoupanos, Martin Uhrin, Leopold Talirz, Leonid Kahle, Rico Häuselmann, Dominik Gresch, Tiziano Müller, Aliaksandr V. Yakutovich, Casper W. Andersen, Francisco F. Ramirez, Carl S. Adorf, Fernando Gargiulo, Snehal Kumbhar, Elsa Passaro, Conrad Johnston, Andrius Merkys, Andrea Cepellotti, Nicolas Mounet, Nicola Marzari, Boris Kozinsky, and Giovanni Pizzi. AiiDA 1.0, a scalable computational infrastructure for automated reproducible workflows and data provenance. *arXiv:2003.12476 [cond-mat]*, March 2020.

Appendix A

Appendix I

A.1 The use of soft pseudopotentials

The accuracy of plane wave pseudopotential DFT calculations depends on the quality of the pseudopotentials used. In general, potentials with the smaller core radii (r_c) have better transferability, but they require higher plane wave cut off energies. Having a large plane wave basis set can significantly increase the computational cost, especially for large systems, where the parallelisation is achieved by distributing **G** vectors to different CPUs. Studies included in this thesis mostly concern ionic solids, where the electron density typically varies smoothly, and the atoms have large separations. This justifies the use of relatively soft pseudopotentials for these materials. The accuracy of energy differences among structures that are chemically similar is also helped by the cancellations of the systematic errors.

In Chapter 5, the DFT calculations of the slabs are performed using the soft QC5 potentials tabulated in Table A.1. The ionic bonding in the relevant materials gives rise to large separations between atoms, so the cores of the potentials do not overlap. In addition, calculations using the harder potentials (Table A.3) are performed for a few cases. The resulting energy differences are similar to those computed using the softer potentials, giving no change in the ranking of the structures.

In Chapter 6, the random structure searching is also performed using the soft pseudopotentials, since only the energy differences among structures with identical compositions are needed.

The NMR study in Section 5.5 gives additional justifications for using the soft pseudopotentials. The chemical shift is a sensitive local probe, and the values obtained using the soft potentials are almost identical to those computed with the harder ones.

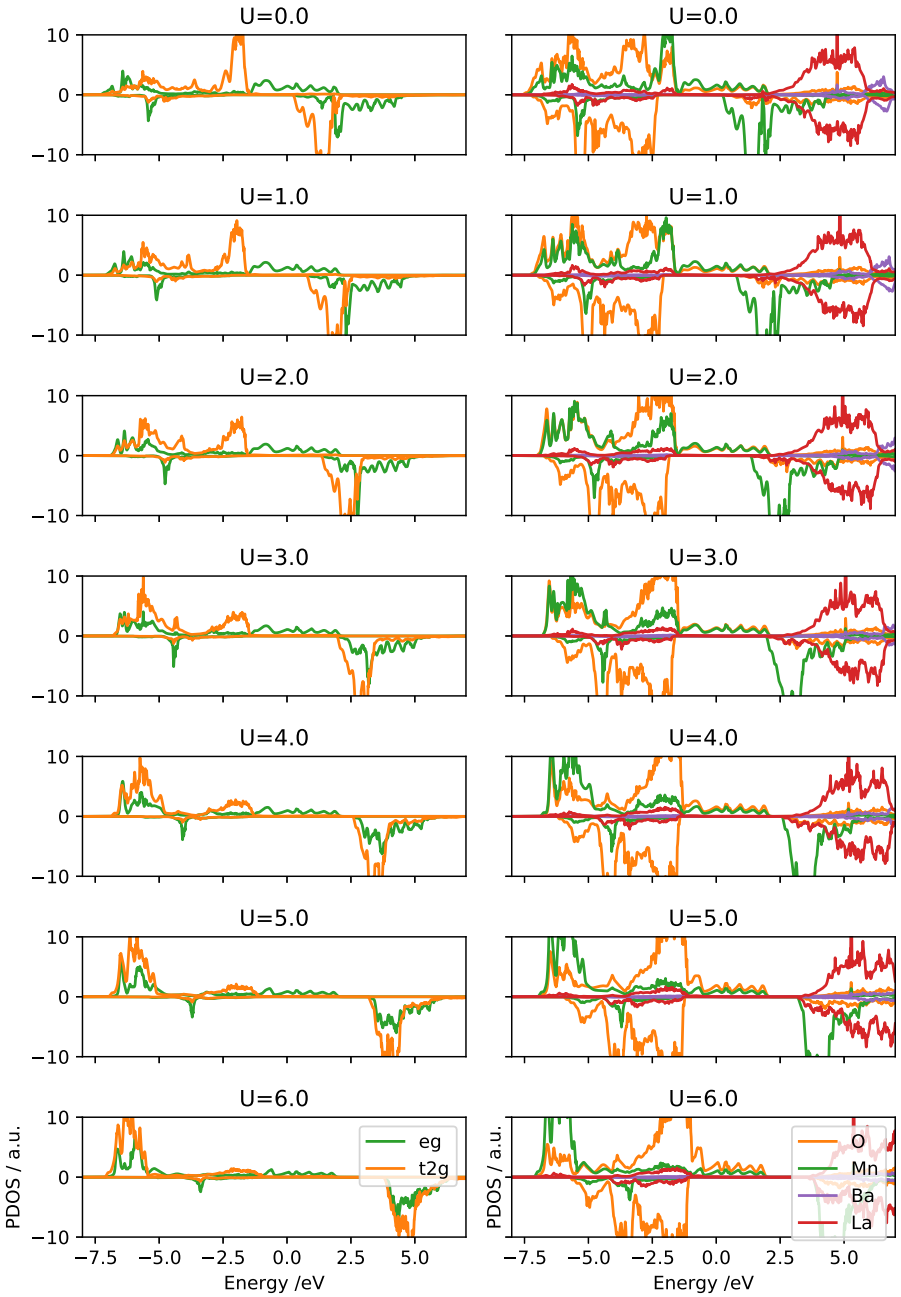

Fig. A.1 Projected density of states for Mn *eg* and Mn t_{2g} electrons (left column) and each specie (right column). The those of the minority spin channel are shown as negative values.

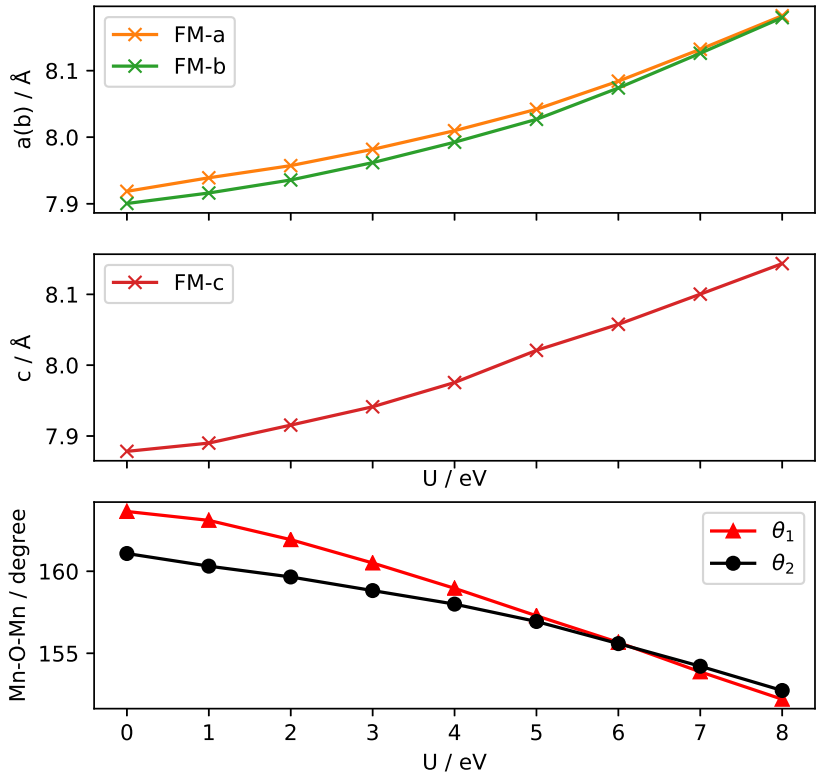

Fig. A.2 Lattice constants and Mn-O-Mn bond angles oriented perpendicular/parallel (θ_1/θ_2) to the c axis (of anti-phase rotation) in relaxed LBMO with a range of U values.

Table A.1 Generation strings of the soft OTFG pseudopotentials. They are included in the QC5 library in CASTEP 18.1.

Element	OTFG string
O	2|1.5|8|9|10|20:21(qc=5)
Ce	2|2.2|7|7|9|50U:60:51:43:52L(qc=5)
Sr	3|2.0|7|7|9|40U:50:41:42(qc=5)
Ti	3|1.9|8|9|10|30U:40:31:32(qc=5)

Table A.2 Generation strings of the soft OTFG pseudopotentials used for structure searching. They are included in the QC5 library in CASTEP 17.2.

Element	OTFG string
O	2|1.5|7|7|9|20:21(qc=5)
Ce	2|2.2|7|7|9|50U:60:51:43:52L(qc=5)
Sr	3|2.0|7|7|9|40U:50:41:42(qc=5)
Ti	3|1.9|8|9|10|30U:40:31:32(qc=5)

Table A.3 Generation strings of the hard OTFG pseudopotentials used. They are included in the C9 library in CASTEP.

Element	OTFG string
O	2|1.1|15|18|20|20:21(qc=7)
Ce	2|2.1|9|10|11|50U:60:51:43:52L(qc=6)
Sr	3|2.0|5|6|7|40U:50:41:42
Ti	3|1.8|9|10|11|30U:40:31:32(qc=5.5)
Mn	3|2.2|2.0|0.7|9|10|11|40:41:32(qc=5.5)
La	2|2.3|5|6|7|50U:60:51:52(qc=4.5)

A.2 Code usage

Descriptions are given below for the computer codes used during the research.

`AiiDA` is an open source framework (see Section 8.2.1) for preserving the provenance of computational studies, and it can also act as a workflow engine. Most DFT calculations presented in this thesis are automated and managed with AiiDA.

`AIRSS` is a software package, available under the GNU General Public License V2.0 (GPLv2), for performing (ab initio) random structure searching*, and the analysis of its results. The `buildcell` program for building random structures, together with the analysis tool `cryan`, are used in the studies described in Chapters 5 and 6.

`atomap` is a python library for analysing atomic resolution scanning transmission electron microscopy images, and it is available under GPLv3. The routines for extracting positions of individual atomic columns using 2D Gaussian fitting are used in the analysis of STEM-HAADF images of $LaCuO_3$/La_2CuO_4 VAN films (Section 8.1).

`ASE` is a python package for setting up, manipulating, running, visualizing and analysing atomistic simulations, and it is freely available under the GNU Lesser General Public License. It is used throughout the projects for setting and manipulating input structures of various calculations.

`CASTEP` is a density functional theory code using plane wave basis set and pseudopotentials. It is used throughout the studies described in this thesis.

`GULP` is a program for performing simulations on materials based on interatomic potentials. It is used for structure searching and defect energy calculations in Chapter 5.

`LAMMPS` is a program for performing massive parallel molecular dynamics simulations based on interatomic potentials. In Chapter 6, it is used to study the anion diffusion at interfaces whose structures are predicted using AIRSS. LAMMPS is a free software released under GPLv2.

`OptaDOS` is a software suite for computing high quality density of states (DOS) using the output of plane wave DFT calculations. It is used to generate the DOS plots using the output of CASTEP. A modified version is written to allow output of *lm* resolved projected density of states (PDOS). OptaDos is available under GPLv2.

*Both the structure prediction method and the code package have the name *Ab initio Random Structure Searching*.

`Quantum Espresso` is a density function theory code using plane wave basis set and pseudopotentials. It is a a free software released under GPLv2. It is used in the preliminary works (not presented in this thesis) of the study described in Chapter 7.